

Carnegie Mellon University

CARNEGIE INSTITUTE OF TECHNOLOGY

THESIS

SUBMITTED IN PARTIAL FULFILLMENT OF THE REQUIREMENTS

FOR THE DEGREE OF Doctor of Philosophy

TITLE

SUPER-PLANCKIAN THERMAL RADIATION FROM NANOPHOTONIC

STRUCTURES: THEORY, SIMULATION AND EXPERIMENT

PRESENTED BY **BAOAN LIU**

ACCEPTED BY THE DEPARTMENT OF
MECHANICAL ENGINEERING

ADVISOR, MAJOR PROFESSOR

DATE

DEPARTMENT HEAD

DATE

APPROVED BY THE COLLEGE COUNCIL

DEAN

DATE

**SUPER-PLANCKIAN THERMAL RADIATION FROM NANOPHOTONIC
STRUCTURES: THEORY, SIMULATION, AND EXPERIMENT**

Submitted in partial fulfillment of the requirements for

the degree of

Doctor of Philosophy

in

Mechanical Engineering

Baoan Liu

B.S., Electrical and Computer Engineering, Shanghai Jiao Tong University, 2011

Carnegie Mellon University
Pittsburgh, PA

May, 2016

©

Baoan Liu

All Rights Reserved

2016

ACKNOWLEDGEMENTS

I have to show my foremost and heartfelt thanks to my PhD advisor, Prof. Sheng Shen (Committee chair). In 2011, Prof. Shen picks me to join his research group as one of his first students in Carnegie Mellon University, which turned out to be one of the most fortunate things in my life. During my PhD study, he was intensively involved in each step of my researches and gave me his insightful guidance. His attitude on pursuing the ultimate limit and the strictness on research helped me grow a lot in my professional career development and become a mature researcher. Other than work-related issues, he also gave me his earnest guidance on my life problems and offering lessons from his experiences.

I would like to thank Prof. Shi-Chune Yao, Prof. Alan J. H. McGaughey, and Prof. Elias Towe for serving on my thesis committee and giving me their insightful and earnest suggestions to my research and my future career path. I would like to express my gratitude to all of my colleagues and my friends for their support and friendship. In particular, the encouragement and insight I received from Siheng Chen, Jianjun He, Jinsheng Gao, Wei Gong, Ankit Jain, Pengfei Li, Simon Lu, Tong Lv, Shubhaditya Majumdar, Wee-Liat Ong, Kevin Parrish, Francisco Ramirez, Keith Regner, Scott Schiffres, Jiawei Shi, Ramesh Shrestha, Zonghui Su, William Wei, Weitao Wu, Ivy Yu is greatly appreciated. I feel honored to have shared this experience with each of them. My warmest thanks belong to my family and especially my beloved wife, Jing. Meeting you is THE most fortunate thing in my life. Without your support, patience, and faith on me, this thesis would not be possible.

Finally, I would like to thank Carnegie Mellon University and the National Science Foundation for supporting my research.

ABSTRACT

SUPER-PLANCKIAN THERMAL RADIATION FROM NANOPHOTONIC STRUCTURES: THEORY, SIMULATION AND EXPERIMENT

by

Baoan Liu

Chair: Sheng Shen

Thermal radiation from macroscopic objects is limited by the well-known Planck's law. However, when the sizes of the objects or the gaps between the objects are in the micro- or nano-scale, Planck's law is no longer valid and the radiative power can exceed the blackbody limit by orders of magnitude. This super-Planckian thermal radiation phenomenon has attracted significant attention in the fields of the thermal management, energy conversion, infrared sensing and imaging, etc. Nevertheless, in comparison with the traditional thermal radiation under the framework of Planck's law, the understanding of super-Planckian thermal radiation is still relatively immature in the aspects of theoretical description, numerical modeling, and experimental characterization.

In this dissertation, we discover new methodologies to design and manipulate the super-Planckian thermal radiation by using the nanophotonic techniques, such as metamaterial, plasmonics, optical cavity effects, etc. First, we present a broadband near-field thermal emitter based on hyperbolic metamaterials, which can significantly enhance near-field radiative heat

transfer with an infrared surface-polariton resonant materials and maintain the monochromatic characteristic of heat transfer. Second, we discover that the thermal graphene plasmons can be efficiently excited and have monochromatic and tunable spectra by graphene nanoribbons, which are resonant near-field thermal emitters. We further demonstrate that "thermal information communication" via graphene surface plasmons can be potentially realized by effectively harnessing thermal energy from various heat sources. To further understand the super-Planckian thermal radiation of the resonant emitters, we develop a general and self-consistent theory from fluctuational electrodynamics and Quasi-Normal Mode theory to describe the thermal radiation from microscale optical resonators made by lossy and dispersive materials. With our theory, we finally propose a general formalism to make the perfect resonant thermal emitters from the densely packed transmission line resonators, and experimentally demonstrate that the thermal emission from the transmission line resonator arrays can be maximized by tuning the waveguiding mode loss or bending the individual structure.

In addition, we implement two numerical simulation methods (the Wiener Chaos Expansion method and the Fluctuating Surface Current method) to directly calculate the super-Planckian thermal radiation of arbitrary geometries. We also propose two highly efficient algorithms to expedite the simulations of periodic and symmetric structures and two-dimensional materials like graphene. These two numerical methods serve as our general computational tools and allow us to investigate the thermal radiation of complex nanophotonic structures in detail.

TABLE OF CONTENTS

ACKNOWLEDGEMENTS	4
ABSTRACT	5
LIST OF TABLES	10
LIST OF FIGURES	11
1 Underlying Principles of Super-Planckian Thermal Radiation	16
1.1 Overview of Super-Planckian Thermal Radiation	16
1.2 Introduction to Classical Electrodynamics	20
1.3 Fluctuational Electrodynamics and Thermal Radiation	25
1.4 Motivation and Scope	27
2 Direct Calculation of Thermal Radiation	31
2.1 Overview	31
2.2 The Wiener Chaos Expansion Method	35
2.2.1 Fundamental Principle	35
2.2.2 Simulation of Periodic Structures	44
2.3 Fluctuating Surface Current Method	53
2.3.1 Introduction to the Boundary Element Method	53
2.3.2 Fluctuating Surface Current Formulation	58
2.3.3 An Efficient Formalism for Simulating Two Dimensional Materials	61

3	Broadband near-field radiative thermal emitter and absorber based on hyperbolic metamaterials	71
3.1	Introduction.....	71
3.2	Enhanced near-field heat transfer between an IR-SPR emitter and a hyperbolic metamaterial.....	74
3.3	Simulation Results	77
3.4	Conclusion	82
3.5	Appendix: Current Modes.....	83
4	Thermal graphene plasmonic interconnects.....	86
4.1	Introduction.....	86
4.2	Thermal excitation of monochromatic and tunable GSPs	87
4.3	Information communication via thermal GSPs.....	94
4.4	Conclusion	98
5	Quasi-Normal Mode Theory for Thermal Radiation from Lossy and Dispersive Optical Resonators.....	100
5.1	Introduction.....	100
5.2	Theory	102
5.3	Numerical Validation.....	110
5.4	Conclusion	113
6	Perfect Narrow-band Thermal Emission by Transmission Line Resonators	115

6.1	Introduction.....	115
6.2	Maximizing Thermal Emission of Transmission Line Resonators.....	116
6.3	Experimental Validation.....	121
6.4	Conclusion	127
7	Conclusions and Outlook.....	129
7.1	Conclusions.....	129
7.2	Outlook and future work.....	131
	REFERENCES.....	133

LIST OF TABLES

Table 1: The current modes used to expand the cuboid unit cell.....	85
---	----

LIST OF FIGURES

Figure 1-1: (a) The schematic of far-field thermal radiative energy transfer. (b) The schematic of near-field thermal radiative energy transfer. (c) The schematic of the thermal emission of a microscale thermal emitter.....	18
Figure 2-1: The schematic of a radiative thermal emitter.....	36
Figure 2-2: Illustration of Wiener Chaos Expansion method for directly calculating thermal radiation heat flux P and field profile $E2$	37
Figure 2-3: Illustration of the concept of current mode expansion in Wiener Chaos Expansion method.....	43
Figure 2-4: The schematic of a periodic and symmetric structure composed by a thin film emitter VE and a grating absorber VA	46
Figure 2-5: Discrete dipole approximation to the continuous current density.....	47
Figure 2-6: Radiative heat transfer between two SiC thin film. The result is calculated by the Wiener Chaos Expansion method.....	49
Figure 2-7: (a) The schematic of periodic nanowire arrays and a thin film. (b) The thermal radiative energy transfer between the arrays and the thin film calculated by the Wiener Chaos Expansion method.....	51
Figure 2-8: (a) The schematic of an object $V1$ in the vacuum space $V0$, where $V1$ encompasses a current source js . (b) and (c) The electromagnetic fields represented by the Huygens' equivalent principle. (b) for the fields inside $V1$, and (c) for the fields inside $V0$	54
Figure 2-9: The schematic of two objects $V1$ and $V2$ in vacuum space $V0$	59
Figure 2-10: (a) Far-field thermal radiation of an infinite long gold nanorod. (b) Near-field thermal radiative energy transfer between two silica microspheres.....	61

Figure 2-11: The schematic of a 2D resistive boundary S and an auxiliary boundary S' 63

Figure 2-12: Extinction cross-section of graphene nanoribbon..... 66

Figure 2-13: The schematic of two resistive boundary $S1$ and $S2$ in vacuum space $V0$ 67

Figure 2-14: Thermal radiative energy transfer between two graphene nano-ribbons (the width of the ribbons equals 50nm, the gap equals 50nm, Fermi level of graphene equals 0.2eV). The thickness of graphene in thin film model equals 0.3nm. 70

Figure 3-1: Plot of radiative heat transfer between two semi-infinite plates maintained at 0K and 300K against the vacuum gap size d . SiC-SiC case (red curve) is compared with SiC-gold case (blue curve). Blackbody radiation limit is also plotted for reference (black dashed line)..... 72

Figure 3-2: Plot of the expression $\text{Im}rTM\exp(-\gamma d)$ to estimate the photon local density of state (LDOS) at $d = 100\text{nm}$ above the surface of semi-infinite (a) SiC, (b) Au, and (c) limiting case of metal wire arrays (MWAs). 77

Figure 3-3: Spectral heat flux into PEC MWA and gold MWA due to current Mode 1. The MWAs have the same geometry: wires radius $r = 50\text{nm}$, wires period $a = 300\text{nm}$. The vacuum gap size d between the MWAs and SiC plate is 100nm..... 78

Figure 3-4: (a) Schematic diagram (3D view and top view) of the SiC plate heat emitter (at 300K) and the metal wire arrays heat absorber (at 0K) separated by a vacuum gap. Metal wires have infinite length, radius $r = 50\text{nm}$ and period $a = 300\text{nm}$. (b) Spectral heat flux into metal wire arrays from sinusoidal current modes in the SiC plate at a 100nm vacuum gap. (c), (d) Electric and magnetic field profiles in metal wire arrays at the SPR frequency ($1.78 \times 10^{14}\text{rad/s}$) of SiC, measured at the plane $2\mu\text{m}$ above the gap. 79

Figure 3-5: (a) Comparison between heat fluxes from $1\mu\text{m}$ thick SiC plate (at 300K) to MWAs (at 0K) and semi-infinite gold plate (at 0K), as a function of the vacuum gap size. Also the

performance of ideal MWAs is plotted for reference. (b) Spectral heat flux between the SiC plate and the MWAs with different (a, r) at a 100nm gap. Here a, r denote the period and the radius of metal wires, respectively. 81

Figure 4-1: (a) Schematic of a graphene nanoribbon thermal emitter and a graphene sheet. (b) Electric field intensity E^2 (color plot) and Poynting vector (green quiver plot) due to the thermal emission from the nanoribbon emitter. Blue lines indicate the locations of graphene ribbon and sheet. (c) Spectral field intensity E_x, ω^2 (in the unit of $V^2 \cdot m^{-2} \cdot rad^{-1} \cdot s$ and plot in log scale) along the x direction and at 15nm above the graphene sheet. The white dashed lines indicate the location of the graphene nanoribbon emitter. The black dashed line indicates the peak frequency ($\omega = 2.3 \times 10^{14} rad/s$) of the thermally excited GSPs. (d) Spectral energy fluxes of the thermally excited GSPs by graphene nanoirbbon emitters with different W and EF , at the same gap $d = 50nm$. (e) The total power Φ (normalized to the area of nanoribbon) of the thermally excited GSPs as a function of d 88

Figure 4-2: (a) and (b) Contribution from each photon mode kz, ω to the thermal excitation of GSPs on the graphene sheet, for (a) $d = 50nm$ and (b) $d = 15nm$, respectively. The graphene nanoribbon emitter has $EF = 0.2eV$ and $W = 50nm$. The white curves represent the dispersion relation of intrinsic GSPs on a single graphene sheet. (c) Thermal radiation field profile due to the photon modes from the two regions: $kz < k_{GSP}$ and $kz > k_{GSP}$. (d) The spectral energy flux carried by the surface waves with $kz < k_{GSP}$ for both $d = 50nm$ and $d = 15nm$ cases. . 92

Figure 4-3: (a) Schematic of a basic demonstration in which graphene nanoribbon A is a transmitter, and nanoribbons B, C are receivers. The graphene sheet with a finite width of $4\mu m$ serves as a GSP waveguide. The gap between the nanoribbons and the sheet is 50nm. (b) Spectral energy fluxes for $A \rightarrow B$ (blue curve) and $A \rightarrow C$ (red curve). The results are normalized

to the area of the nanoribbon transmitter. (c) Local energy flux profiles on receiver B (blue curve), receiver C (red curve), and graphene waveguide (green curve). The red and blue regions indicate the locations of the graphene ribbons..... 95

Figure 4-4: (a) Schematic of two graphene nanoribbon transmitters and two nanoribbon receivers. The graphene sheet waveguide has the finite width of $6.4\mu\text{m}$. (b) Spectral energy transfer for different transmitter and receiver pairs. The total energy fluxes for $A \rightarrow C$ and $B \rightarrow D$ are $1.3 \times 10^4 \text{W/m}^2$ and $6.6 \times 10^3 \text{W/m}^2$, respectively. The "cross-talk" energy fluxes for $A \rightarrow D$ and $B \rightarrow C$ are $4.4 \times 10^2 \text{W/m}^2$ and $7.6 \times 10^2 \text{W/m}^2$, respectively. The results are normalized to the area of the corresponding nanoribbon transmitter. 97

Figure 5-1: The schematic of an optical resonator thermal emitter and a near-field absorber placed in the vacuum background..... 102

Figure 5-2: (a) and (b) Electric field profile of the fundamental resonant mode of the gold nanorod with $D = 40\text{nm}$ and $L = 2.5\mu\text{m}$. Color profile and the arrows indicate the field intensity and polarization, respectively. (c) Fractional mode losses and the thermal emission peak value for the cases with different D . (d) Spectral energy flux of thermal emission evaluated based on theory (dash curves) and direct calculation (solid curves)..... 112

Figure 5-3: (a) and (b) Electric field profile of the fundamental resonant mode of two aligned gold nanorods with $D = 60\text{nm}$, $L = 2.5\mu\text{m}$ and a 50nm gap. Color profile and the arrows indicate the field intensity and polarization, respectively. (c) Fractional mode losses and the thermal emission peak value for the cases with different D . (d) Spectral energy flux of thermal emission evaluated based on theory (dash curves) and direct calculation (solid curves)..... 113

Figure 6-1: (a) The schematic of the transmission line resonator. (b) The electric field profile of the fundamental resonant mode. Arrows indicate the electric field polarization directions. (c) The

effective propagating index of the transmission line waveguiding mode at the wavelength of $7\mu\text{m}$, inset: the electric field profile of the waveguiding mode. (d) The fractional mode losses ηE and η^∞ , and the thermal emission peak ψ of the cases with different A 117

Figure 6-2: (a) and (b) The schematic of the bended transmission line resonators in C-shape (a) and (b) V-shape. (c) and (d) The fractional mode losses ηE and η^∞ , and the thermal emission peak ψ of the cases with different d and θ . (e) and (f) the electric field profile of the fundamental resonant modes for both the cases. Arrows indicate the electric field polarization directions. .. 119

Figure 6-3: (a) and (b) The schematic of the transmission line resonator arrays. (c) The SEM image of an individual transmission line resonator in the arrays. (d) The y-polarized emissivity spectrums of arrays with different H and (e) their corresponding peak values. (f) The y-polarized emissivity spectrums of the resonator arrays with different period and $H = 35\text{nm}$ 121

Figure 6-4: (a) The SEM images of the C-shape transmission line resonators with different gap distance d . (b) The y-polarized emissivity spectrums of the C-shape resonator arrays with different d , and (c) the corresponding peak values. (d) The y-polarized and x-polarized emissivity spectrums of the C-shape arrays with $d = 400\text{nm}$ 125

Figure 6-5: (a) The SEM images of the V-shape transmission line resonators with different bending angle θ . (b) The y-polarized emissivity spectrums of the V-shape resonator arrays with different θ , and (c) the corresponding peak values. 127

1 Underlying Principles of Super-Planckian Thermal Radiation

1.1 Overview of Super-Planckian Thermal Radiation

Thermal radiation is the electromagnetic waves emitted by an object as a result of its temperature [1]. For an object at the temperature $T > 0K$, random electric charge oscillations are thermally induced inside the materials. According to the electromagnetic theory, these oscillating charges emit electromagnetic waves, which are regarded as thermal radiation. In history, thermal radiation from macroscopic objects has been well studied. In the year of 1900, German physicist Max Planck proposed the upper limit of the thermal radiation from arbitrary macroscopic objects [2], which is well-known Planck's law of blackbody radiation. His famous law dictates that, for any emitting surface at the temperature of T in thermal equilibrium, the thermal radiation power per unit surface area per unit frequency cannot exceed the blackbody limit [1]

$$B_T(\nu) = \pi \frac{2\nu^2}{c_0^2} \frac{h\nu}{\exp\left(\frac{h\nu}{k_B T}\right) - 1}, \quad (1.1)$$

where ν is the emitting frequency, k_B is the Boltzmann constant, h is the Planck constant, c_0 is the speed of light in vacuum. π comes from the solid angle integration over the hemisphere, which accounts for the emission in all the directions. Since the blackbody limit defines the maximum power emission from a single object, it can therefore be used to describe the maximum radiative energy transfer between two objects.

However, Planck himself recognized that the blackbody limit in Eq.(1.1) fails in the micro- or nano-scale, when the characteristic lengths of the geometries are comparable or smaller than the dominant wavelength of thermal radiation $\lambda_{th} = hc_0/k_B T$ [3]. The experimental measurements have shown that the Planck's blackbody limit can be exceeded in the cases of (i)

the thermal radiative energy transfer between two closely separated objects, and (ii) the thermal emission from a nanoscale emitter. The super-Planckian radiative energy transfer has been observed in the following experimental works. In the late 1960s, anomalous radiative energy transfer between flat metallic surface was reported [4,5]. In 2005, the radiative energy transfer between a gold-coated scanning tunneling microscope and a plate of gold or GaN was measured [6], and the heat transfer was demonstrated to increase as the decrease of the nanoscale gap. Around the year of 2008, the radiative energy transfer between a silica micro-sphere attached on a cantilever and a silica plate has been measured by the MIT group [7,8] and CNRS group [9], where the heat transfer coefficients at the nanoscale gaps are directly observed as three orders of magnitude larger than that of the blackbody radiation limit [7]. Recently, the super-Planckian radiative energy transfer has been measured for the exotic structures and materials with more sophisticated experimental setups, including silica sphere to doped Si and VO_2 [10,11], silica sphere to nanowire arrays [12], two parallel plates [13], and parallel thin films [14,15]. On the other hand, the super-Planckian thermal emission from a single nanoscale emitter has also been observed. In 2007, the thermal emission from a platinum nanowire with sub-micron transverse size was measured to be larger than the blackbody limit calculated based on its geometrical cross-section [16]. In 2013, the thermal emission rate of an optical fiber with subwavelength diameter was observed to be larger than the prediction from Planck's law [17]. There also exists indirect characterization of the super-Planckian thermal emission from a SiC whisker [18].

The super-Planckian phenomena are attributed to the "wave nature" of thermal radiation, whereas the blackbody limit treats the thermal emission as particles traveling along straight lines. In the derivation of Planck's law, a blackbody can be modeled as a small hole on the surface of a

large vacuum chamber made by perfect metal at the temperature of T [19]. Inside the chamber, "photon gas" is created and annihilated by obeying the Bose-Einstein statistics. Therefore, the blackbody radiation is essentially the propagating photons leaked from the hole, which can be viewed as particles traveling along the straight lines. As a result, the blackbody limit in Eq. (1.1) is invalid when (i) the photons cannot be simply treated as propagating particles, where they are not traveling along the straight *lines*; (ii) the surface area of the blackbody is subwavelength, where the photon cannot go through because of the diffraction limit.

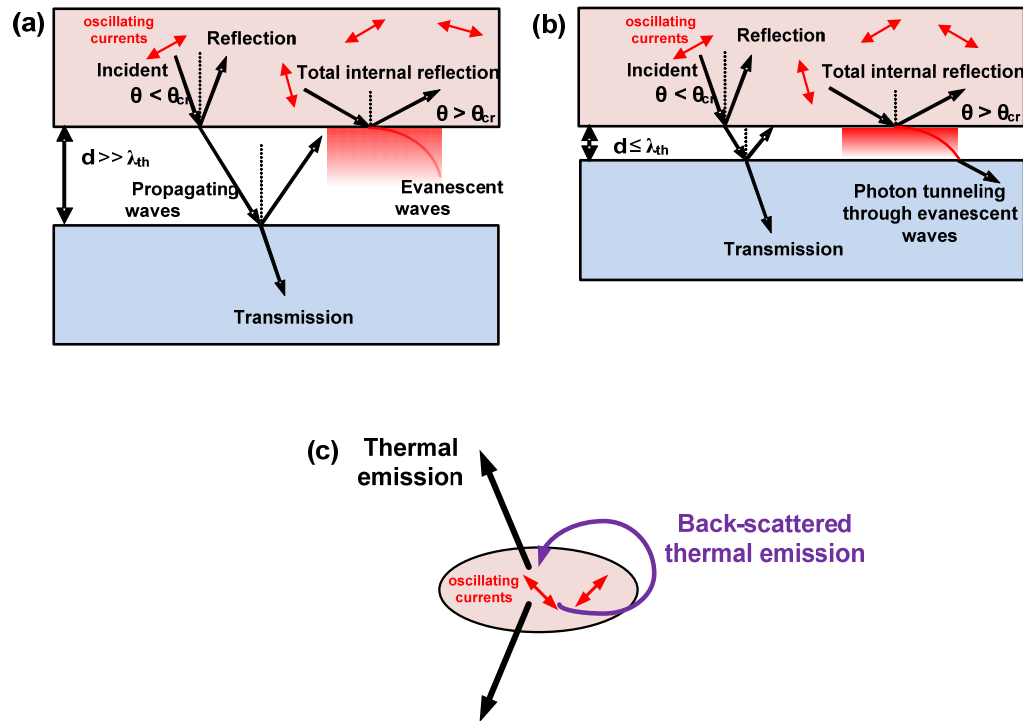


Figure 1-1: (a) The schematic of far-field thermal radiative energy transfer. (b) The schematic of near-field thermal radiative energy transfer. (c) The schematic of the thermal emission of a microscale thermal emitter.

For the cases of two closely separated objects, the super-Planckian phenomenon is caused by the extra contribution from the evanescent waves (or photon tunneling) to the radiative energy transfer, as depicted in Figure 1-1(a) and (b). Here, evanescent waves are the electromagnetic waves decaying exponentially away from the emitter, which can be excited by the total internal reflection. Inside the thermal emitter, the electromagnetic waves are emitted from the thermally induced random oscillating currents. Some of the waves escape from the emitter and become the propagating radiation, and some of them are trapped inside the emitter due to the total internal reflection. When the two objects are separated by a large gap, as shown in Figure 1-1(a), only the propagating waves contribute to energy transfer, and the radiative energy transfer is limited by the blackbody limit. However, when the objects are separated by a microscale gap, as shown in Figure 1-1(b), in which the evanescent waves impinge upon the absorber before the total attenuation, both the propagating waves and the evanescent waves contribute to the energy transfer, leading to a case exceeding the blackbody limit. The thermal radiation enabled by evanescent waves is usually known as near-field thermal radiation [20–23].

For a single microscale emitter, its thermal emission can also exceed the blackbody limit evaluated based on its geometrical area, especially in the case that the random oscillating currents strongly interact with their own back-scattered radiation waves, as illustrated in Figure 1-1(c). In this scenario, the power emitted by a current source can be significantly increased because the back-scattered waves strongly enhance the electric field intensity at the current source. This retardation interaction has been well understood as the Purcell effect [24].

To describe the thermal radiative energy transfer between two closely separated objects and the thermal emission of microscale emitters, Planck's formalism should be abandoned. Instead, thermal radiation requires to be rigorously formulated by the fluctuational

electrodynamics, which is a theory derived from the first principles [25–27]. The key of the fluctuational electrodynamics is the fluctuation-dissipation theorem [28–30], which connects the statistical properties of the thermally induced random currents with the temperature. The thermal radiation is then expressed as the electromagnetic waves emitted from the random currents according to the Maxwell equations. Note that the fluctuational electrodynamics is rigorously formulated by the quantum field theory [27,31]. Nevertheless, the classical formulation of the fluctuational electrodynamics proposed by S. M. Rytov are widely used [23,25], where the results totally agrees with that of the quantum mechanical formulation if the quantum discretization effect is negligible. Based on this theory, the super-Planckian phenomena have been successfully predicted for various structures including parallel plates [26,32], metamaterials [33–35], graphene [36,37], and nanowires [38,39], etc..

In this Chapter, the fluctuational electrodynamics theory is introduced for describing the thermal emission and radiative energy transfer. Here, we follow the classical formulations proposed by S. M. Rytov [25]. To be self-consistent, we first briefly reviewed the classical electromagnetics in Section 1.2. Then, the fluctuational electrodynamics is introduced and the expression for thermal radiation is derived in Section 1.3. Finally, the motivation and the scope of this dissertation are discussed in Section 1.4.

1.2 Introduction to Classical Electrodynamics

Thermal radiation, visible light, and radio waves are all electromagnetic waves, which are essentially the oscillating electric field and the magnetic field propagating at the speed of the light. The properties of the electromagnetic waves are described by electrodynamics. To

understand the thermal radiation from the prospective of waves, the fundamental principles of electrodynamics are briefly reviewed in this section based on Ref. [24,40].

In electrodynamics, there are four key quantities: (1) electric charges ρ ; (2) electric current j , which is the motion of the electric charge, i.e. $j = \frac{\partial \rho}{\partial t}$; (3) electric field E , which determines the electric force experienced by a charged particle q , i.e. $F = qE$; (4) magnetic field H , which determines the magnetic force experienced by a moving charged particle q , i.e. $F = qv \times \mu H$, where v is the velocity of the charged particle and μ is the permeability of the material. $\mu_0 = 4\pi \times 10^{-7} N \cdot A^{-2}$ is the constant indicating the permeability of vacuum.

The Maxwell equations can be used to describe the correlation between these four key quantities, as shown in Eq. (1.2)-(1.5)

$$\nabla \cdot D = \rho \quad (1.2)$$

$$\nabla \cdot B = 0 \quad (1.3)$$

$$\nabla \times E = -\frac{\partial B}{\partial t} \quad (1.4)$$

$$\nabla \times H = j + \frac{\partial D}{\partial t}, \quad (1.5)$$

where $D = \epsilon E$ is the electric displacement field, and $B = \mu H$ is the magnetic B-field. ϵ is the permittivity determined by the material properties, and in vacuum $\epsilon = \epsilon_0 = 8.85 \times 10^{-12} F/m$. μ is the permeability and in vacuum $\mu = \mu_0 = 4\pi \times 10^{-7} N \cdot A^{-2}$. Note that E, D, H, B, j, ρ in Eq. (1.2)-(1.5) are the functions of position and time. The propagating speed of the electromagnetic waves c inside the material equals

$$c = \sqrt{\frac{1}{\epsilon\mu}}. \quad (1.6)$$

The E and H fields also satisfy the boundary conditions at the interface between two different materials 1 and 2, as

$$\hat{\mathbf{n}} \times (E_1 - E_2) = 0 \quad (1.7)$$

$$\hat{\mathbf{n}} \times (H_1 - H_2) = K \quad (1.8)$$

$$\hat{\mathbf{n}} \cdot (D_1 - D_2) = \sigma \quad (1.9)$$

$$\hat{\mathbf{n}} \cdot (B_1 - B_2) = 0, \quad (1.10)$$

where $\hat{\mathbf{n}}$ indicates the normal direction of the interface, K and σ are the external surface current source and external surface charge density on the boundary, respectively.

The Maxwell equations demonstrate that the electromagnetic waves can be excited by the time oscillating current source, because

$$\begin{aligned} \nabla \times (\nabla \times E) &= \nabla \times \left(-\frac{\partial B}{\partial t} \right) \\ &= -\mu_0 \frac{\partial \nabla \times H}{\partial t} \\ &= -\mu_0 \frac{\partial}{\partial t} \left[j + \epsilon_0 \epsilon \frac{\partial E}{\partial t} \right] \end{aligned} \quad (1.11)$$

which leads to

$$\nabla \times (\nabla \times E) + \frac{1}{c^2} \frac{\partial^2 E}{\partial t^2} = -\mu_0 \frac{\partial j}{\partial t} \quad (1.12)$$

Eq. (1.12) has the form of “wave equation”. Consider the one-dimensional case without losing the generality. $\nabla \times \nabla \times E = \nabla(\nabla \cdot E) - \nabla^2 E = -\nabla^2 E$ inside a homogenous medium, which can be further reduced to $-\frac{\partial^2}{\partial r^2}$. The general solution of Eq. (1.12) then equals $E = f(r - ct) + g(r + ct)$, where f and g are non-zero functions if $\frac{\partial j}{\partial t} \neq 0$. Here, f and g can be understood as the forward and the backward propagating wave, respectively.

The exact field profile of the electromagnetic wave $[E(r, t), H(r, t)]$ can therefore be determined by solving Eq. (1.12) together with the boundary conditions in Eq. (1.7)-(1.10). The temporal dependency of the field profile $[E(r, t), H(r, t)]$ can be further eliminated by assuming the current source $j(r, t)$ and the fields have the Fourier transform representation,

$$\begin{aligned} j(r, t) &= \int_{-\infty}^{\infty} d\omega j(r, \omega) \exp(-i\omega t) \\ E(r, t) &= \int_{-\infty}^{\infty} d\omega E(r, \omega) \exp(-i\omega t) \\ H(r, t) &= \int_{-\infty}^{\infty} d\omega H(r, \omega) \exp(-i\omega t) \end{aligned} \quad (1.13)$$

where $j(r, \omega)$, $E(r, \omega)$, and $H(r, \omega)$ are known as the phasor of the electric current, E-field, and H-field, respectively. Substituting Eq. (1.13) into Eq. (1.12), the wave equation becomes

$$(\nabla \times \nabla \times -k^2)E(r, \omega) = i\omega\mu_0 j(r, \omega) \quad (1.14)$$

where $k = \frac{\omega}{c}$ is defined as the wavevector. For the linear operator $\nabla \times \nabla \times -k^2$, $E(r, \omega)$ can be represented in terms of the Dyadic Green's function as [24]

$$E(r, \omega) = i\omega\mu_0 \int dr'^3 G(r, r', \omega) \cdot j(r', \omega) \quad (1.15)$$

where the Dyadic Green's function $G(r, r', \omega)$ is essentially a 3-by-3 tensor which is defined as

$$\nabla \times \nabla \times G(r, r', \omega) - k^2 G(r, r', \omega) = \mathbf{I}\delta(r - r'). \quad (1.16)$$

In Eq. (1.16), \mathbf{I} is the 3-by-3 unit matrix and δ is the Dirac delta function. Note that finding the analytical solution for Eq. (1.14) and (1.16) can be notoriously difficult in the inhomogeneous media. However, they can always be solved by the numerical methods such as the finite-element method (FEM), finite-difference time-domain method (FDTD), or the boundary element method (BEM). The H field can also be obtained by $H(r, \omega) = \frac{1}{i\omega\mu_0} \nabla \times E(r, \omega)$.

The energy conservation law of electromagnetic waves can be derived from the Maxwell equations as [24]

$$\begin{aligned} & \int_{\partial V} dr^2 \cdot [E(r, t) \times H(r, t)] \cdot \hat{\mathbf{n}} \\ &= -\frac{\partial}{\partial t} \left\{ \frac{1}{2} \int_V dr^3 [D(r, t) \cdot E(r, t) + B(r, t) \cdot H(r, t)] \right\} \\ & \quad - \int_V dr^3 j(r, t) \cdot E(r, t). \end{aligned} \quad (1.17)$$

In Eq. (1.17), V is an arbitrary volume with the boundary of ∂V . The left-hand side indicates the total energy flux out of ∂V , where $E(r, t) \times H(r, t) = S(r, t)$ is defined as the Poynting vector, indicating the energy flux density of the electromagnetic waves. On the right-hand side, the first integral indicates the electromagnetic energy stored in V , and the second term indicates the energy gain inside V due to the external current source $j(r, t)$. In addition, for the time-harmonic

E and H fields, the time average of Poynting vector equals $S(r, \omega) = \frac{1}{2} \text{Re}[E(r, \omega) \times H(r, \omega)^*]$ [24].

1.3 Fluctuational Electrodynamics and Thermal Radiation

Classical electrodynamics alone is insufficient to formulate the thermal radiation, because the value of thermally induced oscillating currents $j(r, t)$ in Eq. (1.5) remains undetermined. To describe the statistical properties of $j(r, t)$, the fluctuation-dissipation theorem is required [25,41]. Although $j(r, t)$ is a stochastic process, it can still be spectrally decomposed by using the Fourier transform based on the Wiener-Khinchin theorem [23]. Therefore, it has

$$\langle j(r, t)j(r', t')^* \rangle = \int d\omega d\omega' \langle j(r, \omega)j(r', \omega')^* \rangle \exp(-i\omega t + i\omega' t'), \quad (1.18)$$

where bracket $\langle \cdot \rangle$ denotes the statistical ensemble average. Clearly, the mean value of the thermal fluctuating currents equals zero, i.e. $\langle j(r, \omega) \rangle = 0$. However, its intensity is not zero, i.e. $\langle |j(r, \omega)|^2 \rangle \neq 0$, which is the origin of the thermal radiation.

To describe the intensity of the thermally induced fluctuating currents $j(r, \omega)$ inside a thermal emitter at the temperature of T , the fluctuation-dissipation theorem is formulated as [23,25,41]

$$\langle j(r, \omega) \cdot j(r', \omega')^* \rangle = \frac{4}{\pi} \omega \text{Im}[\epsilon] \Theta(\omega, T) \delta(\omega - \omega') \delta(r - r') \mathbf{I}, \quad (1.19)$$

where * indicates the complex-conjugate; $\text{Im}[\epsilon]$ is the imaginary part of the permittivity of the emitter; $\Theta(\omega, T) = \hbar\omega / \left[\exp\left(\frac{\hbar\omega}{k_B T}\right) - 1 \right]$ is the Planck's distribution; $\delta(\omega - \omega')$ and $\delta(r - r')$

indicate the temporal and spatial incoherence of $j(r, \omega)$. Since we express $j(r, \omega)$ as a 3-by-1 column vector, the 3-by-3 unit matrix \mathbf{I} on the right-hand side indicates the incoherency of the fluctuation currents at different polarizations. Note that fluctuation-dissipation theorem itself is general and can be applied to any system at thermal equilibrium. The detailed derivation can be found in Ref. [24,25,27].

As a result, thermal radiation can be formulated by the fluctuational electrodynamics, i.e. the Maxwell equations in Eq. (1.2)-(1.5) and the fluctuation-dissipation theorem in Eq. (1.19) [23,25]. Specifically, the field intensity $\langle |E(r, \omega)|^2 \rangle$ of thermal emission can be derived as

$$\begin{aligned}
\langle |E(r, \omega)|^2 \rangle &= \langle E(r, \omega)^* \cdot E(r, \omega) \rangle \\
&= \left[-i\omega\mu_0 \int_{V_E} dr'^3 j^*(r', \omega) G(r, r', \omega)^* \right] \cdot \left[-i\omega\mu_0 \int_{V_E} dr''^3 G(r, r'', \omega) j(r'', \omega) \right] \\
&= \omega^2 \mu_0^2 \int_{V_E} dr'^3 \int_{V_E} dr''^3 \text{Tr}[G(r, r', \omega)^* \cdot G(r, r'', \omega) \cdot \langle j(r'', \omega) j^*(r', \omega) \rangle] \\
&= \frac{4}{\pi} \omega^3 \mu_0^2 \Theta(\omega, T) \epsilon_0 \text{Im}[\epsilon] \int_{V_E} dr'^3 \int_{V_E} dr''^3 \text{Tr}[G(r, r', \omega)^* \cdot G(r, r'', \omega)],
\end{aligned} \tag{1.20}$$

where V_E indicates the volume of the thermal emitter; $\text{Tr}[\cdot]$ is the trace of the matrix, and we use the property $\text{Tr}[ABC] = \text{Tr}[BCA]$.

The radiative energy flux $\langle \frac{1}{2} \text{Re}[E(r, \omega) \times H(r, \omega)^*] \rangle$ can also be derived in the similar manner. For example, the z-component of the radiative energy flux equals

$$\left. \left\langle \frac{1}{2} \text{Re}[E \times H^*] \right\rangle \right|_z = \frac{1}{2} \text{Re}[\langle E_x^* H_y \rangle + \langle E_x H_y^* \rangle - \langle E_y H_x^* \rangle - \langle E_y^* H_x \rangle] \tag{1.21}$$

where

$$\begin{aligned} \langle E_x^* H_y \rangle = & -i \frac{4}{\pi} \omega^2 \mu_0 \Theta(\omega, T) \epsilon_0 \text{Im}[\epsilon] \int_{V_E} dr'^3 \int_{V_E} dr''^3 \text{Tr}[[G(r, r', \omega)^*]_x \\ & \cdot [G^H(r, r'', \omega)]_y]. \end{aligned} \quad (1.22)$$

In Eq. (1.22), $G^H(r, r', \omega)$ indicates the magnetic Dyadic Green's function, which is defined as

$$H(r, \omega) = \int dr'^3 G^H(r, r', \omega) \cdot j(r', \omega), \quad (1.23)$$

and it can be further expressed as

$$G^H(r, r', \omega) = \mu_0 \nabla_r \times G(r, r', \omega). \quad (1.24)$$

Note that both thermal radiation field intensity in Eq. (1.20) and energy flux in Eq. (1.22) are deterministic expressions.

The fluctuational electrodynamics formulations in Eq. (1.20) and Eq. (1.22) provide the first-principle evaluation for thermal radiation. Note that there exists a proof of Eq. (1.20) and Eq. (1.22) based on the quantum field theory [27,31]. The fluctuational electrodynamics formulation poses no assumption on the size of the thermal radiative system. It is applicable on both the cases of far-field and near-field thermal radiation, whereas the Planck's formulation can only be used to evaluate the far-field thermal radiation of the macroscopic objects.

1.4 Motivation and Scope

The motivation of this dissertation is to develop new methodologies to design and manipulate the super-Planckian thermal radiation by using nanophotonic techniques, such as metamaterials, plasmonics, optical cavity effects, etc. To achieve this goal, we first develop and implement

highly efficient numerical tools to directly calculate the thermal radiation from arbitrary geometries based on the fluctuational electrodynamics. With these numerical tools, we investigate the thermal radiation of complex nanophotonic structures, and invent the new thermal radiation devices and discover the new theoretical principles. Finally, we also experimentally verify our theoretical discoveries by using the nano-fabrication techniques. Chapters of this dissertation are arranged in the following manner:

Chapter 2 reviews and introduces two powerful numerical tools, i.e. the Wiener Chaos Expansion method and Fluctuating Surface Current method, for directly calculating the thermal radiation from arbitrary geometries. We implement these two numerical tools with high computational efficiency, and also significantly improve their performances for calculating periodic and symmetric structures (with Wiener Chaos Expansion method) and two-dimensional materials such as graphene (with Fluctuating Surface Current method).

Chapter 3 presents a broadband near-field thermal emitter and absorber based on hyperbolic metamaterials, which can significantly enhance near-field radiative heat transfer with infrared surface-polariton-resonant materials and maintain the monochromatic characteristic of heat transfer. Instead of using effective medium approximation, we perform a direct numerical simulation to accurately investigate the heat transfer mechanisms of metamaterials based on the Wiener-chaos expansion method.

Chapter 4 shows that thermal graphene plasmons can be efficiently excited and have monochromatic and tunable spectra, which paves a way to harness thermal energy for graphene plasmonic devices. We further demonstrate that "thermal information communication" via graphene surface plasmons can be potentially realized by effectively harnessing thermal energy

from various heat sources, e.g., the waste heat dissipated from nanoelectronic devices. These findings open up a new avenue of thermal plasmonics based on graphene for various applications, ranging from infrared emission control, to information processing and communication, and to energy harvesting.

Chapter 5 develops a general and self-consistent theory from fluctuational electrodynamics and Quasi-Normal Mode (QNM) theory to describe the thermal radiation from microscale optical resonators made by lossy and dispersive materials like metals. It shows that to maximize the narrow band thermal radiation from an optical resonator, not only the losses of the resonant mode to the emitter and the absorber (or far-field background) require to be matched, but the resonant mode needs to be electrically quasi-static, i.e. the electric field of the resonant mode oscillates in phase. By efficiently evaluating the lossy resonant modes of an optical resonator using finite element methods, our theory thus paves the way for designing arbitrary optical resonator thermal emitters with perfect or maximized emission.

Chapter 6 propose a general formalism to make the perfect resonant thermal emitters from the densely packed transmission line resonators, i.e. a cropped transmission line with finite length. Transmission lines are essentially the waveguides composed by one or multiple metallic wires, which have been invented more than a century ago and widely used today in radio-frequency communications. We demonstrate that the thermal emission from the transmission line resonator can always be maximized by tuning the waveguiding mode loss or bending the structure. It therefore serves as a general principle to make the perfect thermal emitter by densely packing the resonators on a surface, which is confirmed by our experimental investigation. Our formalism thus depict a new way to engineer the highly efficient narrow-band thermal emitters.

Chapter 7 summarizes the major contributions of the dissertation. The suggestions for further work are also discussed in this chapter.

2 Direct Calculation of Thermal Radiation

2.1 Overview

To evaluate the thermal radiation and radiative heat transfer at the micro/nanoscale, the fluctuational electrodynamics is required. Although Eq. (1.20) and Eq. (1.22) serve as general formulations to calculate radiative field intensity and heat flux, directly computing these two formulas turns out to be extremely difficult in the cases where the geometries are complex. First, deriving the analytical results of Eq. (1.20) and Eq. (1.22) is difficult because the Dyadic Green's function $G(r, r', \omega)$ usually does not have analytical solution for complex geometries. On the other hand, numerically integrating Eq. (1.20) and Eq. (1.22) can be computationally expensive, because $G(r, r', \omega)$ at a huge number of location pairs (r, r') is required to be evaluated, and each computation demands at least $O(N)$ calculation steps by using the finite-element based methods, where N is the number of the infinitesimal meshes used for decomposing the geometries.

The previous research works on the direct calculation of thermal radiation are briefly reviewed as follows. For simple geometries where the analytical expression of the Dyadic Green's function exists, thermal radiation can therefore be directly calculated by evaluating Eq. (1.20) and Eq. (1.22) analytically. This approach has successfully solved the radiative heat flux and thermal radiation spectrum for two parallel plates [26], parallel thin-films [42], two spheres [43], sphere to plate [44], infinite-long cylinders [38], etc. For complex geometries, this analytical approach is not feasible. Therefore, highly efficient numerical methods are proposed to simulate the thermal radiation of arbitrary geometries by decomposing the geometries into small

elements. The representative examples of the numerical methods for directly calculating thermal radiation are listed as follows:

- (i) The scattering matrix method based on the rigorous coupled-wave analysis (RCWA) has been proposed to simulate radiative heat flux for periodic structures [45–47], where the geometries are decomposed into multi-layers by the RCWA method.
- (ii) The Wiener Chaos Expansion (WCE) method has been proposed to simulate both radiative heat flux and field profile for arbitrary geometries [33,37,48], which has been implemented in finite-difference frequency-domain (FDFD) method [48], finite-difference time-domain (FDTD) method [33], and boundary element method (BEM) [37]. In addition, the WCE method has been optimized for periodic structures [33]. In the FDFD and FDTD implementations, the geometries are decomposed into volumetric elements. In the BEM implementation, the geometries are decomposed into surface elements.
- (iii) The Fluctuating Surface Current (FSC) method based on the boundary element method (BEM) has been proposed to simulate the radiative heat flux for arbitrary three dimensional geometries [39,49] and two-dimensional symmetric geometries [37], where the boundaries of the geometries are decomposed into surface elements.
- (iv) The Monte-Carlo method based on sampling the thermally induced random currents has been proposed to simulate both radiative heat flux and field profile for arbitrary geometries [50], where this algorithm is implemented in finite-difference time domain (FDTD) method. The geometries are decomposed into volumetric elements.
- (v) The Thermal Discrete Dipole Approximation (T-DDA) method has been proposed to simulate heat flux for arbitrary geometries [51], where the geometries are decomposed into volumetric elements.

- (vi) The Fluctuating Volume Current (FVC) method has been proposed to simulate radiative heat flux for arbitrary geometries [52], where the geometries are decomposed into volumetric elements.

In this Chapter, we investigate two direct simulation methods for thermal radiation: the Wiener Chaos Expansion method and the Fluctuating Surface Current method, where we implement these two methods as general tools with high computational efficiency, and propose the new formalisms to improve their performances for handling special geometries and materials. The Wiener Chaos Expansion method is introduced in Section 2.2. The underlying principle is first reviewed, and a new formalism for calculating the thermal radiation from periodic and symmetric structures is then presented. The Fluctuating Surface Current method is introduced in Section 2.3. We first briefly review its underlying principles. After that, we investigate a new formalism for calculating the thermal radiation of two-dimensional materials (e.g. graphene).

2.2 The Wiener Chaos Expansion Method

2.2.1 Fundamental Principle

According to the fluctuational electrodynamics, thermal radiation originates from thermally induced random currents. Consider a thermal emitter V_E at the temperature of T , as shown in Figure 2-1. The radiative heat flux $\langle P(r, \omega) \rangle$ can be expressed in terms of the Dyadic Green's function and the random currents $j(r', \omega)$ as

$$\begin{aligned} \langle P(r, \omega) \rangle &= \langle E_x^* H_y \rangle \\ &= -i\omega\mu_0 \int_{V_E} dr'^3 \int_{V_E} dr''^3 \text{Tr}[[G(r, r', \omega)^*]_x \cdot [G^H(r, r'', \omega)]_y \\ &\quad \cdot \langle j(r'', \omega) j^*(r', \omega) \rangle]. \end{aligned} \quad (2.1)$$

Similarly, the thermal radiation field intensity $\langle |E(r, \omega)|^2 \rangle$ equals

$$\begin{aligned} \langle |E(r, \omega)|^2 \rangle &= \omega^2 \mu_0^2 \int_{V_E} dr'^3 \int_{V_E} dr''^3 \text{Tr}[G(r, r', \omega)^* \cdot G(r, r'', \omega) \\ &\quad \cdot \langle j(r'', \omega) j^*(r', \omega) \rangle]. \end{aligned} \quad (2.2)$$

In Eqs. (2.1) and (2.2), $\langle \cdot \rangle$ indicates the ensemble average. $\langle j(r'', \omega) j^*(r', \omega) \rangle$ equals a deterministic expression defined by the fluctuation-dissipation theorem

$$\langle j(r'', \omega) \cdot j^*(r', \omega) \rangle = \frac{4}{\pi} \omega \epsilon_0 \text{Im}[\epsilon(r')] \Theta(\omega, T) \delta(r'' - r') \mathbf{I}. \quad (2.3)$$

As we discussed previously, directly integrating Eqs. (2.1) and (2.2) is extremely computationally inefficient, which is incapable to calculate thermal radiation in general cases.

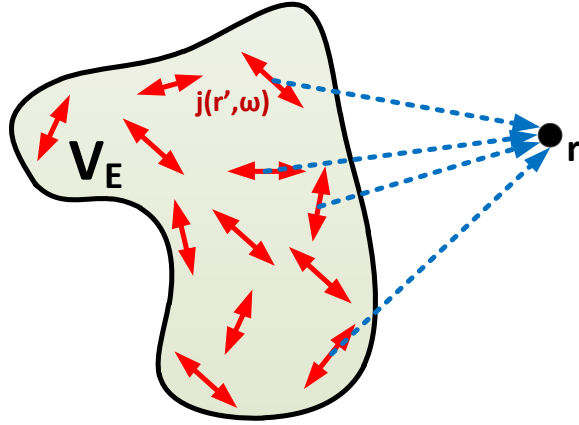


Figure 2-1: The schematic of a radiative thermal emitter.

To avoid the inefficient numerical integration, the Wiener Chaos Expansion method is proposed to calculate thermal radiation of arbitrary geometries by expanding the thermally induced random current $j(r', \omega)$ onto deterministic orthonormal current modes [33,48]. As a result, thermal radiative heat flux (and field profiles) equals the sum of the energy flux (and field profiles) emitted by each current mode, as illustrated in Figure 2-2. By choosing the current modes in the multipole expansion form, the summation can be fast converged in practice. Consequently, only a few number of current modes require to be numerically simulated, and the thermal radiation can therefore be calculated with high computational efficiency.

$$\begin{aligned}
\langle |E|^2 \rangle &= |E_1|^2 + |E_2|^2 + |E_3|^2 + |E_4|^2 + \dots \\
\langle P \rangle &= P_1 + P_2 + P_3 + P_4 + \dots \\
\text{Diagram} &= \text{Diagram}_1 + \text{Diagram}_2 + \text{Diagram}_3 + \text{Diagram}_4 + \dots
\end{aligned}$$

Figure 2-2: Illustration of Wiener Chaos Expansion method for directly calculating thermal radiation heat flux $\langle P \rangle$ and field profile $\langle |E|^2 \rangle$.

The formulation of the Wiener Chaos Expansion method is investigated as follows. According to the fluctuational electrodynamics in Eqs. (2.1) to (2.3), the heat flux $\langle P \rangle$ and field profile $\langle |E|^2 \rangle$ are determined by the first and the second moment of the random currents, i.e. $\langle j(r, \omega) \rangle$ and $\langle j(r, \omega) j^*(r', \omega) \rangle$, with the value of

$$\langle j(r, \omega) \rangle = 0; \quad (2.4)$$

$$\langle j(r, \omega) j^*(r', \omega) \rangle = V_T(r, \omega)^2 \delta(r - r') \mathbf{I},$$

where $\langle j(r, \omega) \rangle = 0$ is attributed to the unbiased nature of the thermal fluctuation; $V_T(r, \omega) =$

$\sqrt{\frac{4}{\pi} \omega \epsilon_0 \text{Im}[\epsilon(r)] \Theta(\omega, T)}$ is a deterministic quantity according to Eq. (2.3). Under the constraint

of Eq. (2.4), the random current $j(r, \omega)$ can be mathematically constructed as

$$j(r, \omega) = V_T(r, \omega) \begin{bmatrix} dW_x(r) \\ dW_y(r) \\ dW_z(r) \end{bmatrix}, \quad r \in V_E \quad (2.5)$$

where dW_x , dW_y , and dW_z are the white noise stochastic processes (i.e. the derivative of Brownian motion), which have the properties of

$$\begin{aligned} \langle dW_l(r) \rangle &= 0 \\ \langle dW_l(r) \cdot dW_k(r') \rangle &= \delta(r - r') \quad \text{for } r, r' \in V_E; l, k \in \{x, y, z\} \end{aligned} \quad (2.6)$$

Note that $dW_l(r)$ is a random process, i.e. it is a random variable for each r . In addition, dW_x , dW_y , dW_z are independent to each other, i.e. $\langle dW_l(r)dW_k(r') \rangle = \langle dW_l(r) \rangle \langle dW_k(r') \rangle = 0$ for $l \neq k; l, k \in \{x, y, z\}$, indicating the random polarization of the random current $j(r, \omega)$.

The properties of $dW(r)$ has been extensively studied in stochastic theories. It can be expanded onto a deterministic orthonormal basis by the Wiener Chaos Expansion (also named as Karhunen-Loève expansion) as [53]

$$dW(r) = \sum_{n=1}^{\infty} c_n \cdot f_n(r), \quad \text{for } r \in V_E \quad (2.7)$$

where c_n are the uncorrelated random variables satisfying

$$\begin{aligned} \langle c_i \rangle &= 0 \\ \langle c_i \cdot c_j \rangle &= \delta_{ij} = \begin{cases} 1 & i = j \\ 0 & i \neq j \end{cases} \end{aligned} \quad (2.8)$$

$\{f_n(r)\}$ is a set of orthonormal basis functions defined in $r \in V_E$, i.e. the volume of the thermal emitter. The orthonormality of $\{f_n(r)\}$ is defined as

$$\int_{r \in V_E} d^3r \cdot f_i(r) \cdot f_j(r) = \delta_{ij} = \begin{cases} 1 & i = j \\ 0 & i \neq j \end{cases} \quad (2.9)$$

The completeness requires that an arbitrary function $H(r)$ with $r \in V_E$ can always be expanded onto $\{f_n(r)\}$, i.e.

$$H(r) = a_1 f_1(r) + a_2 f_2(r) + a_3 f_3(r) + \dots \quad (2.10)$$

for some $\{a_n\}$. Note that $\{f_n(r)\}$ can be chosen in arbitrarily forms as long as Eqs. (2.9) and (2.10) are satisfied. For example, $\{f_n(r)\}$ can have the form of Fourier series if the shape of the thermal emitter is a rectangular prism. $\{f_n(r)\}$ can also be the delta functions, i.e. $f_i(r) = \delta(r - r_i)$, $\forall r_i \in V_E$. By substituting Eq. (2.7) into Eq. (2.5), the thermally induced random current $j(r, \omega)$ can be expressed in terms of the orthonormal basis functions $\{f_n(r)\}$ as

$$j(r, \omega) = \begin{bmatrix} \sum_n c_{xn} \cdot [V_T(r, \omega) f_n(r)] \\ \sum_n c_{yn} \cdot [V_T(r, \omega) f_n(r)] \\ \sum_n c_{zn} \cdot [V_T(r, \omega) f_n(r)] \end{bmatrix}, \quad r \in V_E. \quad (2.11)$$

where c_{xn} , c_{yn} and c_{zn} are the random variables satisfying

$$\begin{aligned} \langle c_{ki} \rangle &= 0 \\ \langle c_{ki} \cdot c_{mj} \rangle &= \begin{cases} 1 & i = j \text{ and } k = m \\ 0 & \text{otherwise} \end{cases} \end{aligned} \quad (2.12)$$

Therefore, the second moment of random current $\langle j(r, \omega) j^*(r', \omega) \rangle$ equals

$$\langle j(r, \omega) j^*(r', \omega) \rangle \quad (2.13)$$

$$= \begin{bmatrix} \sum_i \sum_j \langle c_{xi} c_{xj} \rangle \cdot V_T^2 f_i f_j & \sum_i \sum_j \langle c_{xi} c_{yj} \rangle \cdot V_T^2 f_i f_j & \sum_i \sum_j \langle c_{xi} c_{zj} \rangle \cdot V_T^2 f_i f_j \\ \sum_i \sum_j \langle c_{yi} c_{xj} \rangle \cdot V_T^2 f_i f_j & \sum_i \sum_j \langle c_{yi} c_{yj} \rangle \cdot V_T^2 f_i f_j & \sum_i \sum_j \langle c_{yi} c_{zj} \rangle \cdot V_T^2 f_i f_j \\ \sum_i \sum_j \langle c_{zi} c_{xj} \rangle \cdot V_T^2 f_i f_j & \sum_i \sum_j \langle c_{zi} c_{yj} \rangle \cdot V_T^2 f_i f_j & \sum_i \sum_j \langle c_{zi} c_{zj} \rangle \cdot V_T^2 f_i f_j \end{bmatrix}$$

$$= \begin{bmatrix} \sum_i V_T^2 f_i(r) f_i(r') & 0 & 0 \\ 0 & \sum_i V_T^2 f_i(r) f_i(r') & 0 \\ 0 & 0 & \sum_i V_T^2 f_i(r) f_i(r') \end{bmatrix}$$

Substituting Eq.(2.13) into Eq. (2.1), the radiative heat flux equals

$$\langle P(r, \omega) \rangle = \int_{V_E} dr'^3 \int_{V_E} dr''^3 \text{Tr}[GG_P(r, r', r'', \omega) \cdot \langle j(r'', \omega) j^*(r', \omega) \rangle] \quad (2.14)$$

$$= \int_{V_E} dr'^3 \int_{V_E} dr''^3 \text{Tr} \left[GG_P \cdot \left(\left(\sum_i V_T^2 f_i(r') f_i(r'') \right) \cdot \begin{bmatrix} 1 & 0 & 0 \\ 0 & 1 & 0 \\ 0 & 0 & 1 \end{bmatrix} \right) \right],$$

where we simplify the Dyadic Green's function term $-i\omega\mu_0 \cdot [G(r, r', \omega)^*]_x \cdot [G^H(r, r'', \omega)]_y$ as $GG_P(r, r', r'', \omega)$, or GG_P . We also denote the operator $L_p[\cdot]$ as

$$L_p[X(r', r'', \omega)] = \int_{V_E} dr'^3 \int_{V_E} dr''^3 \text{Tr}[GG_P \cdot X(r', r'', \omega)]. \quad (2.15)$$

As a result, Eq. (2.14) can be represented as

$$\langle P(r, \omega) \rangle = L_p \left[\left(\sum_i V_T^2 f_i(r') f_i(r'') \right) \cdot \begin{bmatrix} 1 & 0 & 0 \\ 0 & 1 & 0 \\ 0 & 0 & 1 \end{bmatrix} \right]. \quad (2.16)$$

Note that $L_p[\cdot]$ is a linear operator, i.e. $L_p[cA + dB] = cL_p[A] + dL_p[B]$, since the trace has the property $\text{Tr}[A \cdot (xB + yC)] = \text{Tr}[A \cdot xB + A \cdot yC] = x\text{Tr}[A \cdot B] + y\text{Tr}[A \cdot C]$. $L_p[h(r', \omega) \cdot h^*(r'', \omega)]$ physically indicates the energy flux due to a given current density distribution $h(r, \omega)$. Consequently, the radiative heat flux $\langle P(r, \omega) \rangle$ equals

$$\begin{aligned} \langle P(r, \omega) \rangle = \sum_i \left\{ L_p \left[\begin{bmatrix} V_T f_i(r') \\ 0 \\ 0 \end{bmatrix} \cdot [V_T f_i(r''), 0, 0] \right] \right. \\ + L_p \left[\begin{bmatrix} 0 \\ V_T f_i(r') \\ 0 \end{bmatrix} \cdot [0, V_T f_i(r''), 0] \right] \\ \left. + L_p \left[\begin{bmatrix} 0 \\ 0 \\ V_T f_i(r') \end{bmatrix} \cdot [0, 0, V_T f_i(r'')] \right] \right\}. \quad (2.17) \end{aligned}$$

Eq. (2.17) is the main result of the Wiener Chaos Expansion method. It describes that the thermal radiative heat flux $\langle P(r, \omega) \rangle$ can be expanded as the sum of the energy flux P_n from each *current mode*, where the current mode n is defined as a set of the same current density distribution $f_n(r)$ with three independent polarization directions

$$\begin{cases} j_{n,x}(r, \omega) = V_T(r, \omega) f_n(r) \hat{\mathbf{x}} \\ j_{n,y}(r, \omega) = V_T(r, \omega) f_n(r) \hat{\mathbf{y}} \\ j_{n,z}(r, \omega) = V_T(r, \omega) f_n(r) \hat{\mathbf{z}} \end{cases}. \quad (2.18)$$

The radiative heat flux $\langle P(r, \omega) \rangle$ in Eq. (2.17) can therefore be represented by current modes as

$$\begin{aligned}
\langle P(r, \omega) \rangle &= \sum_n P_n \\
&= \sum_n \{L_p[j_{n,x} \cdot j_{n,x}^*] + L_p[j_{n,y} \cdot j_{n,y}^*] + L_p[j_{n,z} \cdot j_{n,z}^*]\}
\end{aligned} \tag{2.19}$$

Similarly, the thermal radiation field intensity $\langle |E(r, \omega)^2| \rangle$ can also be expanded in terms of current modes based on the aforementioned derivation as

$$\begin{aligned}
\langle |E(r, \omega)^2| \rangle &= \sum_n |E_n^2| \\
&= \sum_n \{L_E[j_{n,x} \cdot j_{n,x}^*] + L_E[j_{n,y} \cdot j_{n,y}^*] + L_E[j_{n,z} \cdot j_{n,z}^*]\},
\end{aligned} \tag{2.20}$$

where the operator $L_E[\cdot]$ can be defined accordingly based on Eq. (2.2) as

$$L_E[X] = \omega^2 \mu_0^2 \int_{V_E} dr'^3 \int_{V_E} dr''^3 \text{Tr}[G(r, r', \omega)^* \cdot G(r, r'', \omega) \cdot X]. \tag{2.21}$$

The concept of current modes expansion depicted in Eqs. (2.19) and (2.20) is further illustrated in Figure 2-3. The energy flux and the field intensity from each current mode can easily be calculated by the well-known finite-element numerical methods (e.g. finite element method, finite-difference time-domain method, boundary element method), by setting up the electric current source accordingly.

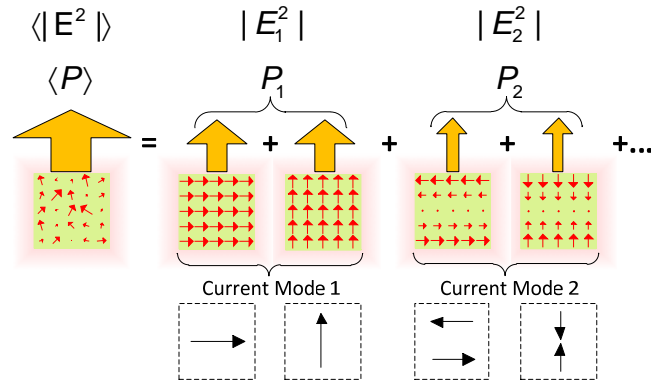


Figure 2-3: Illustration of the concept of current mode expansion in Wiener Chaos Expansion method.

The primary challenge of the Wiener Chaos Expansion method is to find the proper current modes of the thermal emitters in order to achieve fast convergence. For instance, when the current modes are chosen in sinusoidal forms, their expansion can physically be viewed as a classical multipole expansion (Figure 2-3), which leads to a fast convergence for energy flux calculation. Hence, we can truncate the expansion and only keep the lower order current modes without losing accuracy. For an emitter with the rectangular prism shape defined in the Cartesian coordinate as $x \in [0, a] \cup y \in [0, b] \cup z \in [0, z]$, the current mode can be chosen in the form of Fourier series as

$$J_{l,m,n}(r, \omega) = V_T \cdot [H_l(x)P_m(y)Q_n(z)]\{\hat{\mathbf{x}}, \hat{\mathbf{y}}, \hat{\mathbf{z}}\} \quad (2.22)$$

$$H_l(x) = \begin{cases} \frac{1}{\sqrt{a}} & l = 0 \\ \sqrt{\frac{2}{a}} \cos\left[\frac{l\pi x}{a}\right] & l = 1, 2, 3 \dots \end{cases}$$

$$P_m(y) = \begin{cases} \frac{1}{\sqrt{b}} & m = 0 \\ \sqrt{\frac{2}{b}} \cos\left[\frac{m\pi y}{b}\right] & m = 1, 2, 3 \dots \end{cases}$$

$$Q_n(z) = \begin{cases} \frac{1}{\sqrt{c}} & n = 0 \\ \sqrt{\frac{2}{c}} \cos\left[\frac{n\pi z}{c}\right] & n = 1, 2, 3 \dots \end{cases}$$

For complicated geometries, special algorithms can be used to generate the current modes in spherical harmonic forms [54].

2.2.2 Simulation of Periodic Structures

The Wiener Chaos Expansion method in Eqs. (2.19) and (2.20) not only applies to the structures with finite size, but it can also handle the infinitely large structures. In this scenario, choosing proper current modes are especially important to achieve a high computational efficiency. Practically, the expansion on the current modes with larger spatial size generally lead to a slower convergence in comparison with that on the smaller current modes [55,56]. As a result, for the structures with a large or infinite size, naively choosing sinusoidal current modes expanded over the whole structure can make the Wiener Chaos Expansion method extremely inefficient.

For the periodic and symmetric structures with infinite size, we propose a formalism to choose current modes which can lead to a high computational efficiency. Consider a periodic structure composed of a thin film emitter V_E and a grating absorber V_A , as shown in Figure 2-4. Rather than finding the current modes directly for the whole volume of the emitter V_E , we expand the current modes only for an unit cell of the emitter, where the unit cell is the smallest repeatable unit dividing the emitter based on the periodicity and symmetricity of the whole structure. In Figure 2-4, by translating and mirroring the unit cell V_C , the emitter V_E can be replicated. Note that the orthonormal basis functions $\{f_n(r)\}$ in this scenario only require to be defined inside one unit cell, i.e. $r \in V_C$, because the basis functions in all the unit cells are essentially the same, i.e. $\left\{f_n\left(r + \frac{p}{2}m\right)\right\}$ with the translation of the coordinates. As a result, the set of the basis functions from all unit cells satisfies the orthonormality and completeness in Eqs. (2.9) and (2.10) for the whole volume of the emitter V_E .

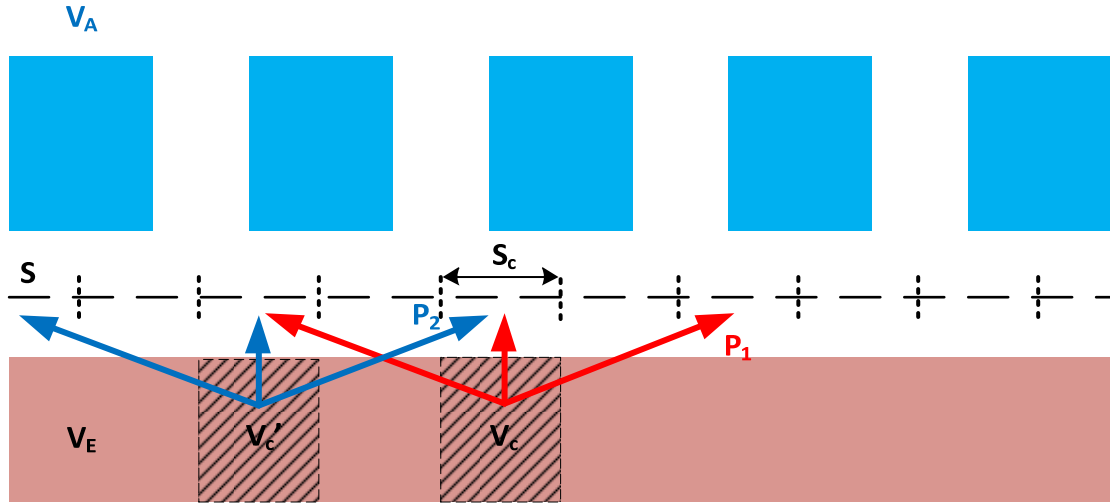


Figure 2-4: The schematic of a periodic and symmetric structure composed by a thin film emitter V_E and a grating absorber V_A .

Therefore, the radiative heat flux between the emitter V_E and the absorber V_A can be obtained by calculating the energy fluxes due to a single unit cell V_c . For the current modes in V_c , the energy fluxes are evaluated at all the points on the surface S , as illustrated in the dashed line in Figure 2-4. As a result, the contributions from all other unit cells are obtained, because the energy flux P_2 from V_c' equals to the energy flux P_1 from V_c . Therefore, by summing up the energy fluxes at all the segments on surface S (as illustrated in Figure 2-4), the actual radiative heat flux at the segment S_c is obtained. Since the size of the unit cell V_c is much smaller than the size of the emitter V_E , the current modes expansion on V_c leads to a faster convergence in comparison with directly expanding the current modes on V_E , therefore makes the Wiener Chaos Expansion method computationally efficient for the periodic and symmetric structures.

The Wiener-Chaos Expansion method can be implemented by any finite-element based computational electromagnetic methods, e.g. FDTD, FEM, BEM, etc., for simulating the

electromagnetic responses from each deterministic current mode. In comparison with the frequency domain methods such as FEM and BEM, the FDTD method can be more efficient because it calculates the whole spectrum in one run, whereas the frequency domain methods only calculate one frequency point in each run. In addition, the FDTD method is available in commercial software, and we use the Lumerical FDTD Solutions® [57] to perform all the simulations in this Section. We also implement a BEM version of the Wiener Chaos Expansion, and the underlying principle is essential the same as what we described here [37].

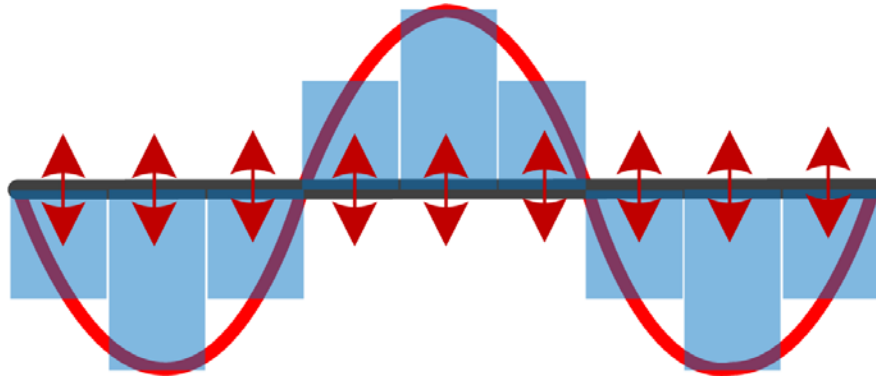


Figure 2-5: Discrete dipole approximation to the continuous current density.

The major technical challenge in the implementation is to set up the continuous current modes by using the discrete point dipole sources. Figure 2-5 illustrates the strategy we used to resolve this challenge. Consider a continuous current distribution $j(x) = f(x)\hat{\mathbf{z}}$ along a straight line $x \in [0, L]$, which is illustrated as the red curve in Figure 2-5. We first approximate it as a step function $F(x)\hat{\mathbf{z}}$ illustrated as the blue histogram. Assume the width of each step is ΔL , the step function is expressed as

$$F(x) = \sum_n f(x_n) \left[u\left(x - \left(x_n - \frac{\Delta L}{2}\right)\right) - u\left(x - \left(x_n + \frac{\Delta L}{2}\right)\right) \right], \quad (2.23)$$

where $\{x_n\}$ indicates the center of each step, i.e. $x_n = n \cdot \Delta L - \frac{\Delta L}{2}$, $u(x)$ is the step function, where $u(x) = 1$ for $x \geq 0$ and $u(x) = 0$ for $x < 0$. Eq. (2.23) can be further expressed as

$$F(x) \approx \sum_n f(x_n) (\delta(x - x_n) \Delta L), \quad (2.24)$$

given the fact that $\delta(x - x_n) = \frac{\partial u(x - x_n)}{\partial x} \approx \left[u\left(x - \left(x_n - \frac{\Delta L}{2}\right)\right) - u\left(x - \left(x_n + \frac{\Delta L}{2}\right)\right) \right] / \Delta L$. Eq.

(2.24) indicates that the current density $F(x)\hat{\mathbf{z}}$ can be mimicked by the point dipole sources located at $\{x_n\}$ with the dipole moment $p_n = \frac{f(x_n)\Delta L}{i\omega} \hat{\mathbf{z}}$.

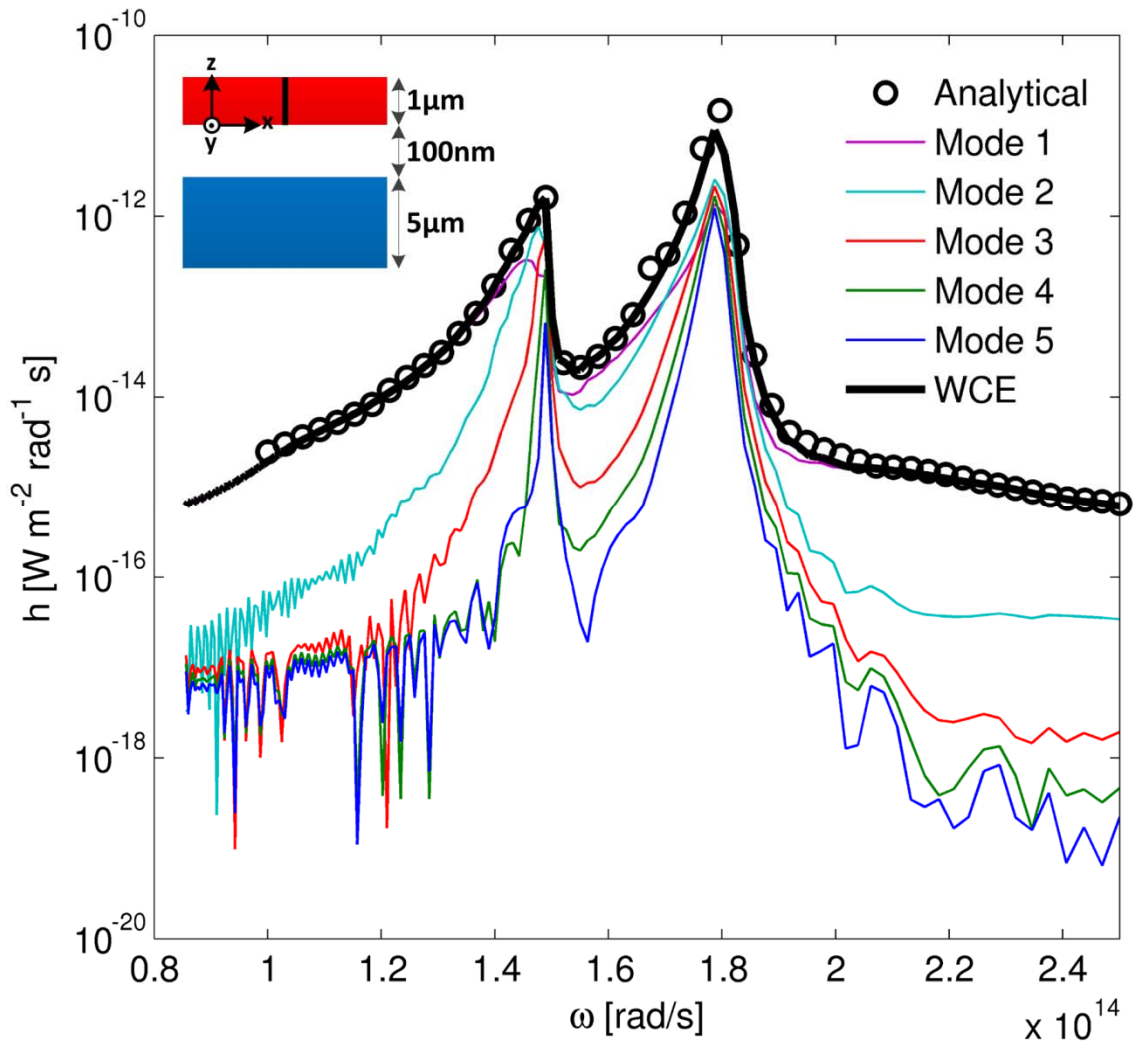


Figure 2-6: Radiative heat transfer between two SiC thin film. The result is calculated by the Wiener Chaos Expansion method.

To prove the concept, we investigate two examples of the thermal radiative energy transfer between two closely separated periodic structures. The first example is two SiC thin films, as shown in Figure 2-6. These two thin films have the thickness of $L_1 = 1 \mu\text{m}$ and $L_2 = 5 \mu\text{m}$, respective, and the gap in between has the distance of 100nm . Since the structure is

uniform in xy direction, the unit cell can be chosen a straight line, i.e. $x \in [x_c, x_c + \Delta x] \cup y = [y_c, y_c + \Delta y] \cup z \in [0, L_1]$, for any x_c, y_c . Therefore, we choose the current modes on this infinitesimal thin rectangular prism based on Eq. (2.22). To calculate the thermal radiative heat flux, we expand the first five current modes [1..5] corresponding to $j_{0,0,\{0..4\}}$, and ten dipole sources are used to approximate the continuous mode functions. For each current mode, the energy flux on a whole xy plane in the gap is recorded. The heat flux between the two thin films can be obtained as the sum of the energy flux due to each mode, and then divides the lateral area of the unit cell, i.e. $\Delta x \Delta y$. Figure 2-6 plots the simulated heat transfer coefficient h at the temperature of $300K$ with the contributions from each current mode. The result from the Wiener Chaos Expansion method agrees well the analytical result in Ref. [58], which convincingly validates our formalism for handling the periodic structures. In addition, a fast convergence of the current mode expansion is also observed, attributing to the multiple expansion form of $j_{0,0,n}$.

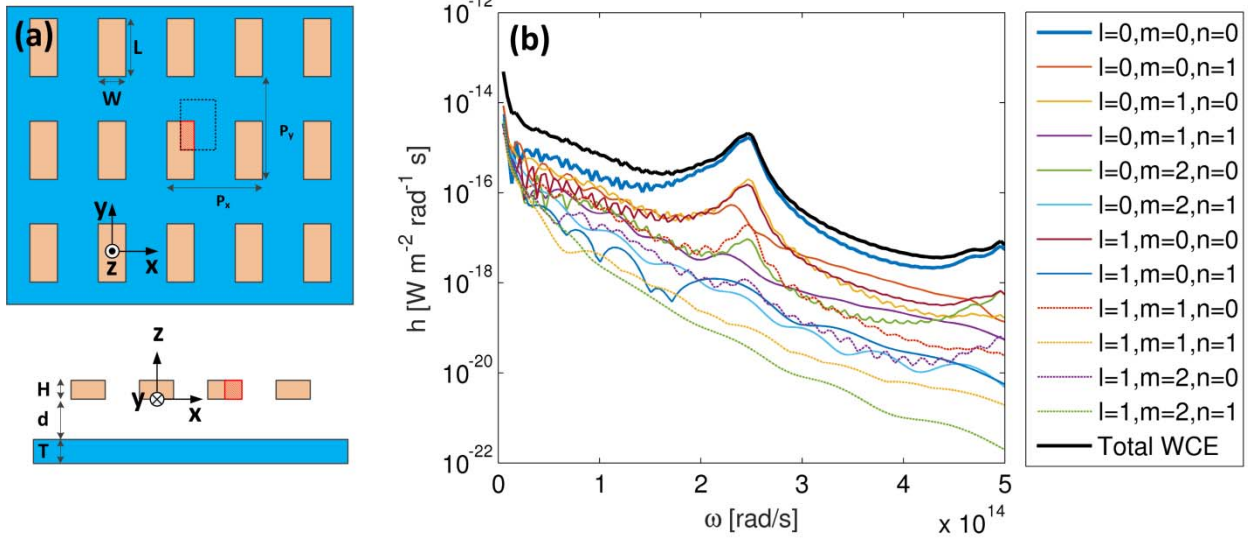


Figure 2-7: (a) The schematic of periodic nanowire arrays and a thin film. (b) The thermal radiative energy transfer between the arrays and the thin film calculated by the Wiener Chaos Expansion method.

The second example is the radiative heat transfer from periodic nanowire arrays to a thin film, as shown in Figure 2-7(a). The nanowires have the size of $L = 3\mu\text{m}$, $W = H = 0.2\mu\text{m}$ and the periods of $P_x = 800\text{nm}$, $P_y = 4\mu\text{m}$. The thin film has the thickness of $T = 400\text{nm}$. The gap distance between the arrays and the thin film is $d = 500\text{nm}$. The materials of both the nanowires and the thin film are N-type doped Si with the doping concentration of $5 \times 10^{21}[\text{cm}^{-3}]$, and the optical property is modeled based on the formulation in Ref. [10]. Based on the periodicity and symmetry of this structure, the unit cell can be chosen as the region indicated as the dashed line in Figure 2-7(a). Therefore, the current modes only require to be expanded inside a quarter portion of a nanowire, as highlighted in the red region in Figure 2-7(a). Similarly, the energy fluxes are calculated on the whole xy -plane in the gap, and the total heat flux is obtained as the

sum of the energy fluxes from all the modes divides the area enclosed by the dashed line in Figure 2-7(a). Figure 2-7(b) plots the directly simulated heat transfer coefficient h between the nanowire arrays and the thin film at the temperature of $300K$ with the expansion of 12 current modes $j_{l,m,n}$ defined in Eq. (2.22). A fast convergence is also observed.

2.3 Fluctuating Surface Current Method

Under the framework of the boundary element method (BEM), the Fluctuating Surface Current (FSC) method directly calculates the thermal radiation energy flux of arbitrary geometries [39,49,59], which potentially has a higher efficiency in comparison with the Wiener Chaos Expansion method. The time complexity of this method is $O(N^3)$, where N is the number of boundary elements used to discretize the geometries. It circumvents the difficulty in finding the proper current modes for bizarre geometries in the Wiener Chaos Expansion method, and calculating the thermal radiation by the FSC method turns out to be as efficient as calculating electromagnetic responses from deterministic sources in the BEM. In this section, we first briefly review the underlying principles of the BEM based on Refs. [59,60]. Then, we introduce the formulation of the FSC method based on Refs. [39,49]. After that, we present an efficient formalism to calculate the thermal radiation of two-dimensional materials like graphene.

2.3.1 Introduction to the Boundary Element Method

The BEM is essentially a highly efficient computational tool for simulating electromagnetic responses [59,60]. In comparison with the popular FEM and FDTD methods, the BEM only requires the surface meshes on the boundaries of the geometries, which can lead to smaller matrix equation. The foundation of the BEM is the Huygens' equivalent principle [61,62], which states that the scattered electromagnetic field from an object can be expressed as the radiation fields due to the equivalent electric and magnetic surface currents on the object. With the Huygens' equivalent principle, the surface integration equation is then derived for solving the equivalent surface currents. After that, the surface integration equation can be converted into a matrix equation by using the Galerkin method, where the matrix equation can be solved by the standard methods, for example, LU-decomposition. Once the equivalent surface currents are

solved, the electromagnetic responses can then be obtained. Here, we briefly review these key concepts of the BEM as follows.

2.3.1.1 Huygens' Equivalent Principle

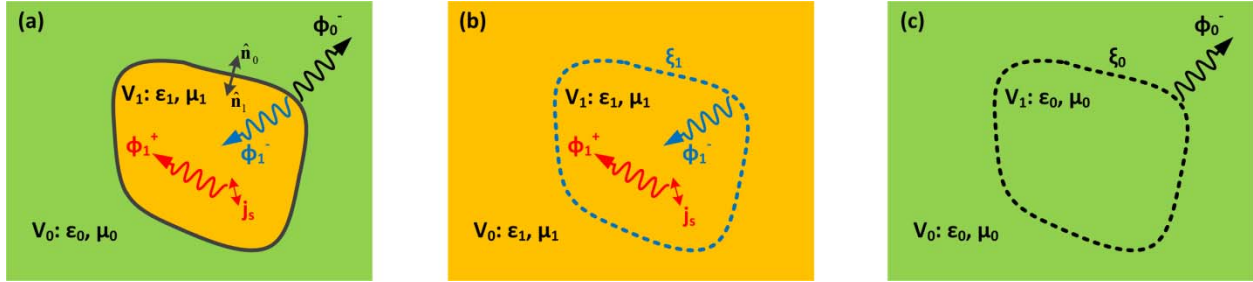


Figure 2-8: (a) Schematic of an object V_1 in the vacuum space V_0 , where V_1 encompasses a current source j_s . (b) and (c) Electromagnetic fields represented by the Huygens' equivalent principle. (b) for the fields inside V_1 , and (c) for the fields inside V_0 .

Consider an object V_1 in the vacuum space V_0 encompassing a current source $j_s(r)$ inside, as illustrated in

Figure 2-8(a). The Huygens' equivalent principle states that the total electromagnetic fields

$\phi_j(r) = \begin{pmatrix} E_j(r) \\ H_j(r) \end{pmatrix}$ inside each region (i.e. V_1 and V_0) can be decomposed into the incident fields

$\phi_j^+(r)$ (due to the source inside V_j) and the scattered fields $\phi_j^-(r)$ (due to the scattering from the

boundaries and the sources in other regions, where both the incident and scattered fields $\phi_j^+(r)$

and $\phi_j^-(r)$ can be represented in terms of the convolution of the Dyadic Green's function of the

homogenous space Γ_j . Specifically, the total fields $\phi_1(r)$ inside V_1 equals [61,62]

$$\begin{aligned}\theta(r)\phi_1(r) &= \phi_1^+(r) + \phi_1^-(r) \\ &= \int_{V_1} dr'^3 \Gamma_1(r, r') \cdot \begin{pmatrix} j_s(r') \\ 0 \end{pmatrix} + \int_{\partial V_1} dr'^2 \Gamma_1(r, r') \cdot \begin{pmatrix} \widehat{\mathbf{n}}_1 \times H_1(r') \\ -\widehat{\mathbf{n}}_1 \times E_1(r') \end{pmatrix},\end{aligned}\quad (2.25)$$

and the total fields $\phi_0(r)$ in the vacuum space equals

$$\begin{aligned}\theta(r)\phi_0(r) &= \phi_0^-(r) \\ &= \int_{\partial V_1} dr'^2 \Gamma_0(r, r') \cdot \begin{pmatrix} \widehat{\mathbf{n}}_0 \times H_0(r') \\ \widehat{\mathbf{n}}_0 \times E_0(r') \end{pmatrix}.\end{aligned}\quad (2.26)$$

In Eqs. (2.25) and (2.26), E_j and H_j are 3-by-1 column vectors, and therefore ϕ is 6-by-1 column vectors. $\Gamma_j(r, r')$ is the 6-by-6 tensor representing the electric and magnetic impulse response due to the electric and magnetic current sources, which equals

$$\begin{aligned}\Gamma_j(r, r') &= \begin{bmatrix} \Gamma_j^{EE} & \Gamma_j^{EH} \\ \Gamma_j^{HE} & \Gamma_j^{HH} \end{bmatrix} \\ &= \begin{bmatrix} i\omega\mu_j G_j(r, r') & -\nabla_r \times G_j(r, r') \\ \nabla_r \times G_j(r, r') & i\omega\epsilon_j G_j(r, r') \end{bmatrix}\end{aligned}\quad (2.27)$$

where $G_j(r, r')$ is the 3-by-3 Dyadic Green's tensor for the homogenous space with the permittivity of ϵ_j and the permeability of μ_j , satisfying

$$(\nabla_r \times \nabla_r - k_j^2)G_j(r, r') = \mathbf{I}\delta(r - r'),\quad (2.28)$$

and $k_j = \omega\sqrt{\epsilon_j\mu_j}$ is the wavevector. Note that $G_j(r, r')$ can be explicitly expressed as

$$G_j(r, r') = \left[I + \frac{1}{k_j^2} \nabla_r \nabla_r \right] \frac{\exp(ik_j|r - r'|)}{4\pi|r - r'|}.\quad (2.29)$$

The factor $\theta(r)$ in Eqs. (2.25) and (2.26) equals $\theta(r) = 1$ for $r \in V_1$ and $\theta(r) = 0.5$ for $r \in \partial V_1$. Note that $[E_1(r), H_1(r)]$ are continuous from $r \in V$ to $r \in \partial V$, even though the value of $\theta(r)$ has a jump. As a result, the equivalent surface currents can be defined as

$$\xi_j(r) = \begin{pmatrix} J_j(r) \\ K_j(r) \end{pmatrix} = \begin{pmatrix} \hat{\mathbf{n}}_j \times H_j(r) \\ -\hat{\mathbf{n}}_j \times E_j(r) \end{pmatrix}, \quad (2.30)$$

where $\hat{\mathbf{n}}_j$ indicates the normal direction of the boundary of the region j , and $\hat{\mathbf{n}}_1 = -\hat{\mathbf{n}}_0$. Eqs. (2.25) and (2.26) therefore become

$$\phi_1(r) = \frac{\phi_1^+(r) + \Gamma_1 \star \xi_1}{\theta(r)} \quad (2.31)$$

$$\phi_0(r) = \frac{-\Gamma_0 \star \xi_0}{\theta(r)},$$

where \star indicates the convolution. Because Γ_j is composed by the Green's functions of homogenous space, Eq. (2.31) has the clear physical meaning. As illustrated in

Figure 2-8(b) and (c), the total fields in each region j equal the incident fields plus the radiation from the equivalent current density ξ_j in the homogenous space.

2.3.1.2 Surface Integral Equation

According to the Huygens' equivalent principle in Eq. (2.31), the electromagnetic field ϕ can be evaluated once the equivalent surface currents ξ are determined. To solve ξ , the surface integral equation is required. For bulk materials, e.g. V_1 , the boundary conditions of the Maxwell equations state that the parallel component of E and H field are continuous at $r \in \partial V_1$, i.e.

$$\widehat{\mathbf{n}}_1 \times [H_1(r) - H_0(r)] = 0 \quad (2.32)$$

$$\widehat{\mathbf{n}}_1 \times [E_1(r) - E_0(r)] = 0.$$

Eq. (2.32) indicates two identities: $\xi_1 = -\xi_0$ and $\widehat{\mathbf{n}}_1 \times (\phi_1(r) - \phi_0(r)) = 0$. Substituting Eq. (2.31) into these two identities, the surface integral equation can be derived as

$$\widehat{\mathbf{n}}_1 \times [(\Gamma_1 - \Gamma_0) \star \xi_1] = \widehat{\mathbf{n}}_1 \times [-\phi_1^+(r)], \quad (2.33)$$

where ξ_1 can be solved accordingly. Eq. (2.33) is known as the PMCHW surface integral equation [39,61].

2.3.1.3 Galerkin discretization and BEM equation

To solve the equivalent surface currents ξ_1 , the surface integral equation in (2.33) requires to be discretized into matrix equation by using the Galerkin method [39,59]. Suppose $\{\beta_n^j(r)\}$ is a set of N basis functions for the 6-component tangential vector fields on the boundary ∂V_j , so that any surface currents or the tangential components of the EM fields $f(r)$ on the boundary can be expressed as $f(r) = \sum_n x_n^j \beta_n^j(r)$ with the coefficients $\{x_n^j\}$. Note that $\{\beta_n^j(r)\}$ is not necessarily orthogonal. As a result, the surface current ξ_1 can be discretized as

$$\xi_1 = \sum_n \langle \xi_1 | \beta_n^1 \rangle \beta_n^1(r), \quad (2.34)$$

where $\langle \cdot | \cdot \rangle$ indicates the inner product i.e. $\langle A | B \rangle = \int_{\partial V} dr^2 A(r)^* \cdot B(r)$, and $*$ denotes the conjugate transpose. Substituting Eq. (2.34) into Eq. (2.33), and taking the inner product of both side of Eq. (2.34) with β_m^1 , the BEM equation can be obtained as

$$Mx = s \quad (2.35)$$

where M is the N-by-N BEM matrix

$$M_{mn} = \langle \beta_m^1 | \Gamma_1 \star \beta_n^1 \rangle - \langle \beta_m^1 | \Gamma_0 \star \beta_n^1 \rangle, \quad (2.36)$$

x is the N-by-1 column vector indicating the equivalent surface currents and $x_n = \langle \xi_1 | \beta_n^1 \rangle$. s is the N-by-1 column vector representing the stimulating sources where $s_n = \langle \beta_n^1 | -\phi_1^+ \rangle$. Note that the $\hat{\mathbf{n}} \times$ is dropped because β is tangential to the boundary. In the BEM, the basis function $\{\beta_n\}$ is usually chosen as the piecewise-polynomial element functions. Specially, we adopt the RWG basis functions for the general three-dimensional structures, and two-dimensional roof-top (TDRT) basis functions for the structures invariant in one direction (i.e. 2D-invariant structures) [59]. As a result, x can be determined by directly solving the BEM equation in Eq. (2.35), where the general matrix solver such as the LU-decomposition or Gaussian elimination methods can be adopted [63]. To perform the BEM simulation, we write our home-made code based on the open-source boundary element method library *scuff-EM* developed by M.T. Reid [59,64].

2.3.2 Fluctuating Surface Current Formulation

With the framework of the BEM, the formulation of the FSC method is briefly introduced as follows, and the derivation details are available in Ref. [39,49]. Consider two objects V_1 and V_2 in the vacuum space V_0 , as illustrated in

Figure 2-9. The surface integral equation of this two-body system can be expressed as

$$\begin{aligned} \hat{\mathbf{n}}_1 \times [(\Gamma_0 + \Gamma_1) \star \xi_1 + \Gamma_0 \star \xi_2] &= \hat{\mathbf{n}}_1 \times [\phi_1^+ - \phi_0^+] \\ \hat{\mathbf{n}}_2 \times [(\Gamma_0 + \Gamma_2) \star \xi_2 + \Gamma_0 \star \xi_1] &= \hat{\mathbf{n}}_2 \times [\phi_2^+ - \phi_0^+]. \end{aligned} \quad (2.37)$$

Then, the BEM equation can be obtained with the Galerkin discretization on a set of the $P + Q$ basis functions $\{\beta_p^1, \beta_q^2\}$ for ∂V_1 and ∂V_2 , as

$$\begin{bmatrix} \langle \beta^1 | (\Gamma_0 + \Gamma_1) \star \beta^1 \rangle & \langle \beta^1 | (\Gamma_0) \star \beta^2 \rangle \\ \langle \beta^2 | (\Gamma_0) \star \beta^1 \rangle & \langle \beta^2 | (\Gamma_0 + \Gamma_2) \star \beta^2 \rangle \end{bmatrix} \begin{bmatrix} \langle \xi_1 | \beta^1 \rangle \\ \langle \xi_2 | \beta^2 \rangle \end{bmatrix} = \begin{bmatrix} \langle \beta^1 | \phi_1^+ - \phi_0^+ \rangle \\ \langle \beta^2 | \phi_2^+ - \phi_0^+ \rangle \end{bmatrix}, \quad (2.38)$$

which corresponds to $Mx = s$. M has the size of $(P + Q)$ by $(P + Q)$. The BEM matrix M can be further expanded as $M = M_0 + M_1 + M_2$, where

$$\begin{aligned} M_0 &= \begin{bmatrix} \langle \beta^1 | \Gamma_0 \star \beta^1 \rangle & \langle \beta^1 | \Gamma_0 \star \beta^2 \rangle \\ \langle \beta^2 | \Gamma_0 \star \beta^1 \rangle & \langle \beta^2 | \Gamma_0 \star \beta^2 \rangle \end{bmatrix} \\ M_1 &= \begin{bmatrix} \langle \beta^1 | \Gamma_1 \star \beta^1 \rangle & 0 \\ 0 & 0 \end{bmatrix} \\ M_2 &= \begin{bmatrix} 0 & 0 \\ 0 & \langle \beta^2 | \Gamma_2 \star \beta^2 \rangle \end{bmatrix}. \end{aligned} \quad (2.39)$$

M_0 represents the multibody interactions via the waves in the vacuum space V_0 . M_1 and M_2 represent the self interactions via the waves inside the object V_1 and V_2 , respectively.

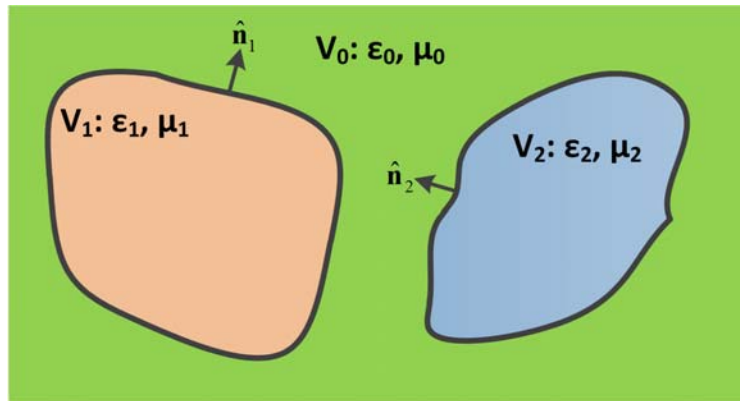


Figure 2-9: The schematic of two objects V_1 and V_2 in vacuum space V_0 .

For the case that V_1 at the temperature of T_1 and V_2 at the temperature of T_2 , the FSC method describes that the thermal radiative energy transfer from V_1 to V_2 equals

$$H = \int_0^{\infty} d\omega [\Theta(\omega, T_1) - \Theta(\omega, T_2)] \Phi_{1 \rightarrow 2}(\omega) \quad (2.40)$$

where $\Theta(\omega, T) = \frac{\hbar\omega}{\exp(\hbar\omega/k_B T) - 1}$, and the spectral energy flux $\Phi_{1 \rightarrow 2}(\omega)$ can be calculated from the BEM matrix M and the self-interaction matrices M_1 and M_2 as

$$\Phi_{1 \rightarrow 2}(\omega) = \frac{2}{\pi} \text{Tr}[\text{sym}[M_1]M^{-1*} \text{sym}[M_2]M^{-1*}]. \quad (2.41)$$

In Eq. (2.41), $\text{Tr}[\cdot]$ denotes the trace of the matrix; $\text{sym}[A] = \frac{1}{2}(A + A^*)$; and M^{-1} indicates the inverse matrix of M . In addition, the thermal emission from V_1 to far-field can also be calculated as

$$\Phi_{1 \rightarrow 0}(\omega) = \frac{2}{\pi} \text{Tr}[\text{sym}[M_1]M^{-1*} \text{sym}[M_0]M^{-1*}]. \quad (2.42)$$

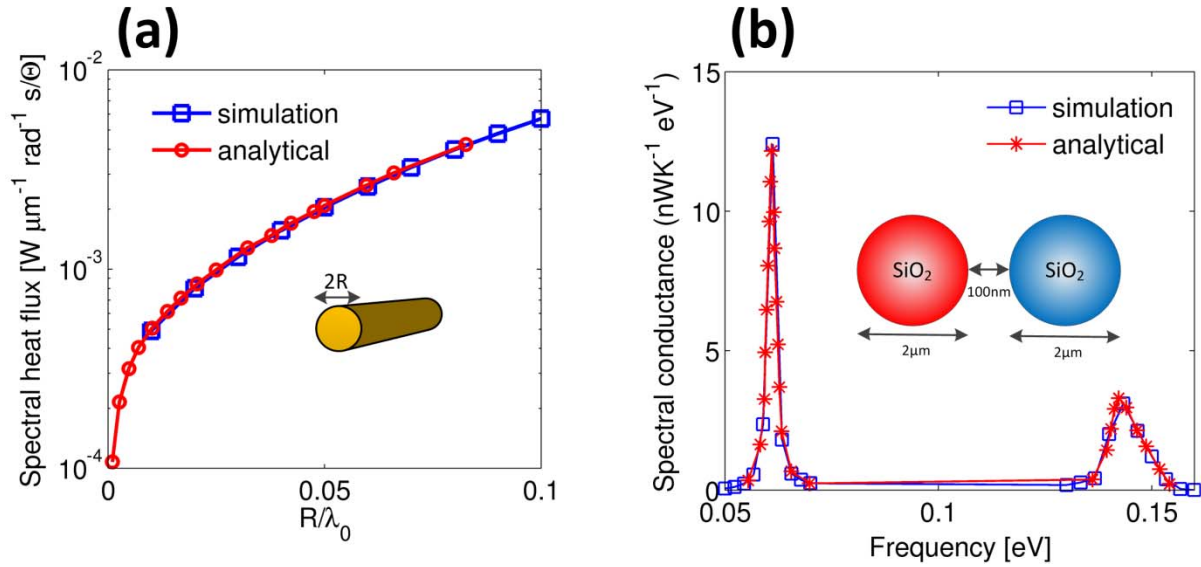


Figure 2-10: (a) Far-field thermal radiation of an infinite long gold nanorod. (b) Near-field thermal radiative energy transfer between two silica microspheres.

We implement the FSC method in Eqs. (2.41) and (2.42) in our home-made BEM code for both three-dimensional structure and the 2D-invariant structure. Figure 2-10 demonstrates two test examples. Our simulation results are directly compared with the analytical solutions in Refs. [38] and [43], respectively. Their excellent agreements convincingly validate our simulation.

2.3.3 An Efficient Formalism for Simulating Two Dimensional Materials

Two dimensional materials are the crystalline materials consisting of a single layer of atoms [65]. Graphene is a single layer of carbon atoms which recently attracts great attention in the fields of photonics and thermal radiation because of its extraordinary optical properties [36,66–68]. Since graphene has a sub-nanometer thickness, it requires to be modeled

as a 2D resistive boundary with an in-plane conductivity $\sigma_g(\omega)$ in the electromagnetics theory [69]. The in-plane conductivity σ_g relates to the volumetric conductivity σ_v as $\delta(z)\sigma_g = \sigma_v$ for a graphene sheet located at $z = 0$. It thus satisfies $j_{x,y} = \sigma_g\delta(z)E_{x,y}$.

To numerically model the 2D resistive boundary in the simulations, there exists intrinsic difficulties for the FEM and FDTD methods, where the 2D resistive boundary requires to be approximated as an extremely thin dielectric film [66,70]. In this case, $\delta(z)$ is approximated as $\delta(z) \approx \frac{u(z-\frac{t}{2})-u(z+\frac{t}{2})}{t}$. Therefore, the volumetric conductivity becomes $\sigma_v = \frac{\sigma_g}{t}$, and the permittivity of the thin film equals $\epsilon = \epsilon_0 + i\sigma_g/(\omega t)$. However, this approximation can severely deteriorate the simulation efficiency because extremely fine meshes are required in this ultra thin film to maintain the accuracy. Very recently, new algorithms are proposed to model the graphene with only a layer of meshes in the FEM and FDTD methods [57,71,72]. Nevertheless, the BEM is the ideal candidate to model the 2D resistive boundary, since it only requires boundary meshes.

However, it is not straightforward to model open 2D resistive boundaries in the BEM, for examples, graphene disks or ribbons. Although the thin-film approximation can still be applied in this scenario [66,73], the BEM simulation can become very inefficient in assembling the self-interaction matrix of the thin-film, due to its very large effective permittivity ϵ . Here, we propose an efficient formalism to model the suspended 2D resistive boundaries in the BEM without using the thin-film approximation, and then we derive the FSC formulation to directly calculate their thermal radiation.

2.3.3.1 Surface Integral Equation for a 2D Resistive Boundary

To model the 2D resistive boundary, a new surface integral equation is required. Consider an open 2D resistive boundary S suspended in vacuum space with the in-plane conductivity of σ_s , as shown in Figure 2-11. The boundary conditions of the Maxwell equation state that

$$\widehat{\mathbf{n}}_0 \times (E_0 - E_1) = 0 \quad (2.43)$$

$$\widehat{\mathbf{n}}_0 \times (H_0 - H_1) = \sigma_s E_0 + J_{ext},$$

at the resistive boundary S , where $[E_0, H_0]$ is the field on the top surface, and $[E_1, H_1]$ is the field on the bottom surface. $\sigma_s E_0$ indicates the induced surface currents on the resistive boundary due to the electric field. J_{ext} denotes the surface current sources in S .

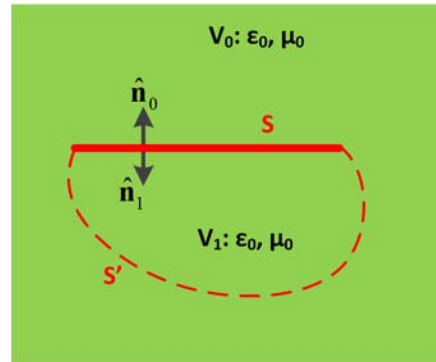


Figure 2-11: The schematic of a 2D resistive boundary S and an auxiliary boundary S' .

To apply the Huygens' equivalent principle, we add an auxiliary boundary S' to connect the ends of S through the vacuum, and then the vacuum space is divided into two regions V_0 and

V_1 . For the region V_0 , the equivalent surface can be defined as $\xi_0 = \begin{pmatrix} J_0 \\ K_0 \end{pmatrix} = \begin{pmatrix} \widehat{\mathbf{n}}_0 \times H_0 \\ -\widehat{\mathbf{n}}_0 \times E_0 \end{pmatrix} \Big|_S$ on S ,

and $\xi'_0 = \begin{pmatrix} J'_0 \\ K'_0 \end{pmatrix} = \begin{pmatrix} \widehat{\mathbf{n}}_0 \times H_0 \\ -\widehat{\mathbf{n}}_0 \times E_0 \end{pmatrix} \Big|_{S'}$ on S' . For the region V_1 , they are defined similarly as $\xi_1 =$

$\begin{pmatrix} J_1 \\ K_1 \end{pmatrix} = \begin{pmatrix} \widehat{\mathbf{n}}_1 \times H_1 \\ -\widehat{\mathbf{n}}_1 \times E_1 \end{pmatrix} \Big|_S$ on S , and $\xi'_1 = \begin{pmatrix} J'_1 \\ K'_1 \end{pmatrix} = \begin{pmatrix} \widehat{\mathbf{n}}_1 \times H_1 \\ -\widehat{\mathbf{n}}_1 \times E_1 \end{pmatrix} \Big|_{S'}$ on S' . Because the boundary

conditions on S' satisfy Eq. (2.32), it has $\xi'_0 = -\xi'_1$. As a result, the fields in V_0 and V_1 can be expressed in terms of the conventional notations as

$$\begin{aligned} \phi_0(r) &= \begin{pmatrix} E_0(r) \\ H_0(r) \end{pmatrix} = \frac{\phi_0^+(r) + \Gamma_0 \star \xi_0 + \Gamma_0 \star \xi'_0}{\theta(r)} \\ \phi_1(r) &= \begin{pmatrix} E_1(r) \\ H_1(r) \end{pmatrix} = \frac{\Gamma_0 \star \xi_1 + \Gamma_0 \star \xi'_1}{\theta(r)} \\ &= \frac{\Gamma_0 \star \xi_1 - \Gamma_0 \star \xi'_0}{\theta(r)}, \end{aligned} \quad (2.44)$$

where $\phi_0^+(r) = \begin{pmatrix} E_0^+(r) \\ H_0^+(r) \end{pmatrix}$ indicates the incident field due to the sources in V_0 . According to the

electric field relation in Eq. (2.43), it has $\widehat{\mathbf{n}}_0 \times 2E_0 = \widehat{\mathbf{n}}_0 \times (E_0 + E_1)$ on S , and $K_0 = -K_1$.

Substituting these two equations into Eq. (2.44), it can be further derived as

$$\begin{aligned} \widehat{\mathbf{n}}_0 \times 2E_0|_S &= \widehat{\mathbf{n}}_0 \times (E_0 + E_1)|_S \\ &= \widehat{\mathbf{n}}_0 \times \frac{1}{\theta} \left\{ E_0^+ + \begin{bmatrix} \Gamma_0^{EE} & \Gamma_0^{EH} \end{bmatrix} \star \left(\begin{bmatrix} J_0 \\ K_0 \end{bmatrix} + \begin{bmatrix} J_1 \\ -K_0 \end{bmatrix} \right) \right\} \Big|_S \\ \Rightarrow \widehat{\mathbf{n}}_0 \times E_0|_S &= \widehat{\mathbf{n}}_0 \times \{ E_0^+ + \Gamma_0^{EE} \star (J_0 + J_1) \} \Big|_S \end{aligned} \quad (2.45)$$

In addition, the magnetic field relation in Eq. (2.43) states that

$$\widehat{\mathbf{n}}_0 \times (H_0 - H_1) = J_0 + J_1 = \sigma_s E_0|_S + J_{ext} \quad (2.46)$$

where $\begin{pmatrix} -1 \\ \sigma_s \end{pmatrix} \mathbf{I}_0^3$ denotes the matrix coefficient for simplifying the notation. In comparison with the self-interaction matrix of the thin-film, i.e. $\langle \beta_m | \Gamma_1 \star \beta_n \rangle$, the self-interaction matrix of the resistive boundary in Eq. (2.49) can be calculated very efficiently without suffering from numerically integrating the Dyadic Green's function Γ_1 with a very large permittivity ϵ .

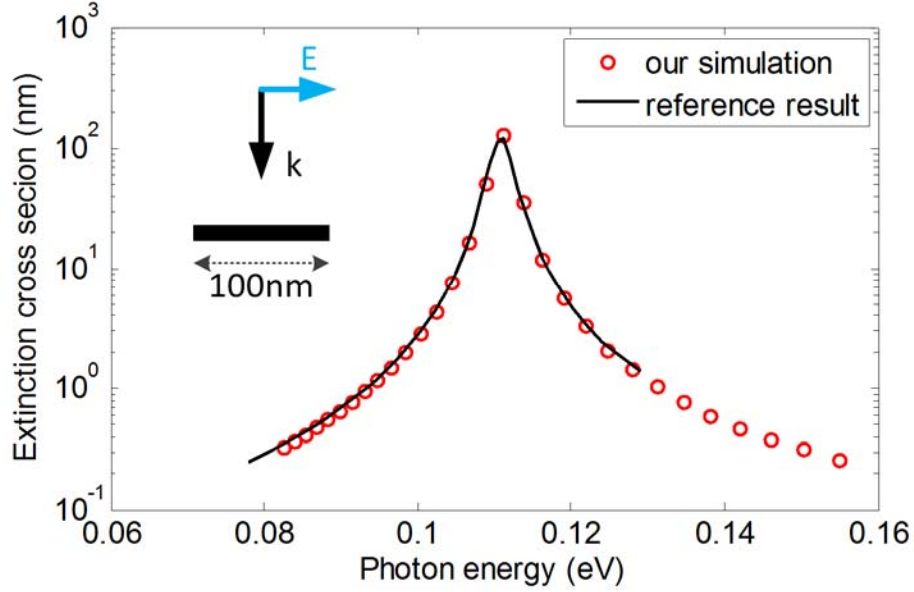


Figure 2-12: Extinction cross-section of graphene nanoribbon.

We validate our BEM code with the implementation of the 2D resistive boundary formulation in Eq. (2.48) by simulating the extinction cross-section of an infinite long graphene nano-ribbon, as shown in Figure 2-12. The graphene nano-ribbon has the width of 100nm and the Fermi level equals 0.2eV. Our simulation result agrees well with the result in Ref. [66].

2.3.3.2 Fluctuating Surface Current Formulation for 2D Resistive Boundary

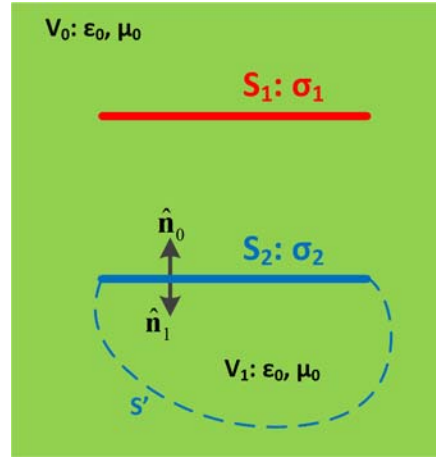


Figure 2-13: The schematic of two resistive boundary S_1 and S_2 in vacuum space V_0 .

The thermal radiative energy transfer between an emitter and an absorber made by 2D resistive boundaries can be directly calculated by the same FSC formulation in Eq. (2.41) and (2.42) with the substitution of the self-interaction matrix in Eq. (2.49). Consider the resistive boundaries S_1 as the emitter and S_2 as the absorber suspended in vacuum space V_0 , as shown in Figure 2-13. Assume the equivalent surface currents $\xi_1 = \begin{pmatrix} J_1 \\ 0 \end{pmatrix}$ on S_1 and $\xi_2 = \begin{pmatrix} J_2 \\ 0 \end{pmatrix}$. According to Eq. (2.48), the BEM equation $Mx = s$ of this system can be expressed as

$$[M_0 + M_1 + M_2] \begin{bmatrix} \langle \xi_1 | \beta_1 \rangle \\ \langle \xi_2 | \beta_2 \rangle \end{bmatrix} = \begin{bmatrix} \left\langle \beta_1 \left| \begin{pmatrix} -J_{ext} \\ \sigma_1 \\ 0 \end{pmatrix} \right. \right\rangle \\ 0 \end{bmatrix}, \quad (2.50)$$

where β_1 and β_2 are the basis for S_1 and S_2 , respectively. J_{ext} indicates the thermally induced random currents inside S_1 . The multibody-interaction matrix M_0 and the self-interaction matrix M_1 and M_2 equal

$$\begin{aligned}
M_0 &= \begin{bmatrix} \langle \beta_1 | \begin{bmatrix} \Gamma_0^{EE} & 0 \\ 0 & 0 \end{bmatrix} \star \beta_1 \rangle & \langle \beta_1 | \begin{bmatrix} \Gamma_0^{EE} & 0 \\ 0 & 0 \end{bmatrix} \star \beta_2 \rangle \\ \langle \beta_2 | \begin{bmatrix} \Gamma_0^{EE} & 0 \\ 0 & 0 \end{bmatrix} \star \beta_1 \rangle & \langle \beta_2 | \begin{bmatrix} \Gamma_0^{EE} & 0 \\ 0 & 0 \end{bmatrix} \star \beta_2 \rangle \end{bmatrix} \\
M_1 &= \begin{bmatrix} \langle \beta_1 | \begin{pmatrix} -1 \\ \sigma_1 \\ 0 \end{pmatrix} \mathbf{I}_0^3 \beta_1 \rangle & 0 \\ 0 & 0 \end{bmatrix} \\
M_2 &= \begin{bmatrix} 0 & 0 \\ 0 & \langle \beta_1 | \begin{pmatrix} -1 \\ \sigma_2 \end{pmatrix} \mathbf{I}_0^3 \beta_1 \rangle \end{bmatrix}.
\end{aligned} \tag{2.51}$$

The radiative energy transfer from S_1 to S_2 equals the energy absorbed by S_2 , i.e.

$$\Phi = - \int_{S_2} dr^2 \frac{1}{2} \widehat{\mathbf{n}}_0 \cdot \text{Re}[E_0 \times H_0^*] - \int_{S_2} dr^2 \frac{1}{2} \widehat{\mathbf{n}}_1 \cdot \text{Re}[E_1 \times H_1^*]. \tag{2.52}$$

The first term on the right hand side of Eq. (2.52) equals

$$- \int_{S_2} dr^2 \frac{1}{2} \widehat{\mathbf{n}}_0 \cdot \text{Re}[E_0 \times H_0^*] = \frac{1}{2} \int_{S_2} dr^2 \text{Re}[E_0 \cdot J_+^*]. \tag{2.53}$$

Similarly, the second term equals $\frac{1}{2} \int_{S_2} dr^2 \text{Re}[E_0 \cdot J_-^*]$, where $J_+ = \widehat{\mathbf{n}}_0 \times H_0$, and $J_- = \widehat{\mathbf{n}}_1 \times H_1$.

According to Eq. (2.43), $J_2 = J_+ + J_-$, and $J_2 = \sigma_2 E_0$. Therefore, the energy transfer Φ from S_1 to S_2 equals

$$\begin{aligned}
\Phi &= \frac{1}{2} \int_{S_2} dr^2 \text{Re}[E_0 \cdot J_2^*] \tag{2.54} \\
&= -\frac{1}{2} \left\langle \xi_2 \left| \text{Re} \left[\frac{-1}{\sigma_g} \right] \xi_2 \right. \right\rangle \\
&= -\frac{1}{2} x^* \text{sym}[M_2] x \\
&= -\frac{1}{2} \text{Tr}[ss^* M^{-1*} \text{sym}[M_2] M^{-1}].
\end{aligned}$$

The term ss^* in Eq. (2.54) indicates the thermally induced random current sources, and $ss^* =$

$$\begin{bmatrix} \left\langle \beta_1 \left| \begin{pmatrix} -J_{ext} \\ \sigma_1 \\ 0 \end{pmatrix} \right\rangle \left\langle \begin{pmatrix} -J_{ext} \\ \sigma_1 \\ 0 \end{pmatrix} \right| \beta_1 \right\rangle & 0 \\ 0 & 0 \end{bmatrix}.$$

According to the fluctuation-dissipation theory,

$$\langle J_{ext}(r) J_{ext}^*(r') \rangle = \frac{4}{\pi} \text{Re}[\sigma_1] \Theta(\omega, T) \delta(r - r') \mathbf{I},$$

where $\langle \cdot \rangle$ denotes the ensemble average.

Therefore,

$$\begin{aligned}
\langle ss^* \rangle_{11, mn} &= \left\langle \left\langle \beta_1^m \left| \begin{pmatrix} -J_{ext} \\ \sigma_1 \\ 0 \end{pmatrix} \right\rangle \left\langle \begin{pmatrix} -J_{ext} \\ \sigma_1 \\ 0 \end{pmatrix} \right| \beta_1^n \right\rangle \right\rangle \tag{2.55} \\
&= \frac{1}{|\sigma_1|^2} \int_{S_1} dr^2 \int_{S_1} dr'^2 [\beta_1^m(r)]^* \langle J_{ext}(r) J_{ext}^*(r') \rangle \mathbf{I}_0^3[\beta_1^n(r')] \\
&= -\frac{4}{\pi} \Theta \int_{S_1} dr^2 [\beta_1^m(r)]^* \text{Re} \left[\frac{-1}{\sigma_1} \right] \mathbf{I}_0^3[\beta_1^n(r)] \\
&= -\frac{4}{\pi} \Theta \text{sym}[M_1].
\end{aligned}$$

Substitute Eq. (2.55) into Eq. (2.54), the FSC formulation for calculating the radiative energy transfer between two resistive boundaries can thus be derived as

$$\phi(\omega) = \frac{2}{\pi} \text{Tr}[\text{sym}[M_1]M^{-1*} \text{sym}[M_2]M^{-1}], \quad (2.56)$$

which agrees with the form of Eqs. (2.41) and (2.42). Note that the similar formulations can also be derived if the emitter or absorber is bulk dielectric or far-field space, where only the self-interaction matrices M_1 and M_2 require to be substitute accordingly.

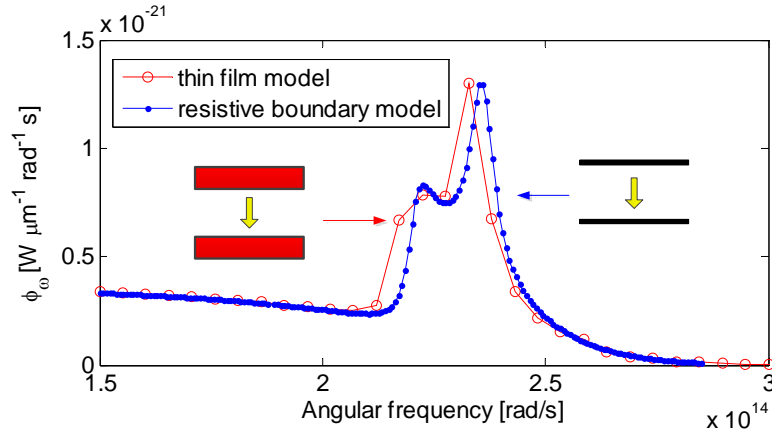


Figure 2-14: Thermal radiative energy transfer between two graphene nano-ribbons (the width of the ribbons equals 50nm, the gap equals 50nm, Fermi level of graphene equals 0.2eV). The thickness of graphene in thin film model equals 0.3nm.

In Figure 2-14, we validate our formulation in Eq. (2.56) by directly calculating the thermal radiative energy transfer between two graphene nano-ribbons modeled as resistive boundaries. The result is then compared with the simulation result based on the thin-film approximation model. Good agreements between these two results are observed, and the resistive boundary model demonstrates significant enhancement of the computational speed.

3 Broadband near-field radiative thermal emitter and absorber based on hyperbolic metamaterials

3.1 Introduction

In the near-field, when the gap distance between objects is smaller than the dominant thermal wavelength predicted by Wien's displacement law, radiative heat transfer can be greatly enhanced by photon tunneling through evanescent electromagnetic waves [23,74,75]. In particular, it has been demonstrated that near-field radiative heat transfer can exceed the prediction from Planck's law by several orders of magnitude [7,9,76], when the interacting materials support infrared surface-polariton resonances (IR-SPRs), including surface phonon polaritons in polar dielectric materials [76] (e.g., cBN, SiC or SiO₂) and surface plasmon polaritons in doped semiconductors [77]. In contrast to far-field radiation in which the spectral distribution of emissive power is usually broadband, near-field thermal emission from an IR-SPR material is almost monochromatic [32]. The IR-SPR based near-field radiation is practically important due to the significant heat transfer enhancement and quasi-monochromatic emission, and has been suggested to be used to increase the efficiency of thermophotovoltaic devices [20,78] and create vacuum thermal rectifiers [79,80].

However, the IR-SPR based near-field heat transfer is strongly material-dependent. The enhancement of heat transfer between two identical IR-SPR materials arises from the coupling of surface polariton waves [32]. If the emitter and absorber are made from different materials which support SPRs at different frequencies, the mismatch between SPR frequencies will result in much less heat transfer. For instance, SiC supports surface phonon polaritons in the infrared range, but gold supports surface plasmon polaritons in the visible range. As shown in Figure 3-1,

near-field radiative heat transfer between semi-infinite SiC and gold plates is found to be three orders of magnitude less than that between two SiC plates.

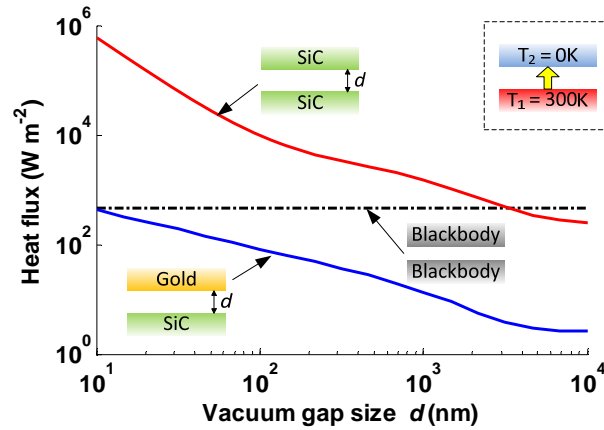


Figure 3-1: Plot of radiative heat transfer between two semi-infinite plates maintained at 0K and 300K against the vacuum gap size d . SiC-SiC case (red curve) is compared with SiC-gold case (blue curve). Blackbody radiation limit is also plotted for reference (black dashed line).

To overcome the material limitation of the IR-SPR based near-field radiation, "metamaterials" have been proposed to enhance near-field radiative heat transfer by designing SPRs at desired frequencies [81]. Metamaterials, which are typically structured at a scale smaller than $1/10^{\text{th}}$ of wavelength, are artificial composite materials whose electromagnetic properties are engineered by sub-wavelength structures such as split-ring resonators and dilute metal wires [82,83]. If the gold plate in Fig. 1 is replaced by the arrays of sub-wavelength gold wires or split ring resonators, the effective resonant frequency of surface plasmon polaritons in the metamaterial can be shifted to match the resonant frequency of surface phonon polaritons in SiC. However, in order to maintain designed effective properties and manipulate thermal radiation in the near-field, a metamaterial needs to meet two criteria: (i) the feature size of the metamaterial

(e.g., period of sub-wavelength structures) must be much smaller than the gap size between the emitter and the absorber, which can be in the range of tens of nanometers [84], and (ii) the metamaterial must have an effective resonant frequency in the infrared range (e.g., wavelength around $10\mu m$) in order to match the resonant frequency of an IR-SPR emitter. For both criteria to be fulfilled simultaneously, the diameters of dilute metal wires and the thicknesses of split ring resonators are predicted to be in the sub-nanometer scale. Although these resonant metamaterials show potential for manipulating near-field radiation, they are very difficult to be experimentally realized with current fabrication technologies.

In this work, we present a broadband non-resonant heat emitter/absorber based on hyperbolic metamaterials [85–87], which can significantly enhance near-field radiative heat transfer between metals and IR-SPR thermal emitters, and maintain the monochromatic characteristic of the IR-SPR based near-field radiation. In order to elucidate the heat transfer mechanisms of complex three-dimensional metamaterials, we directly calculate near-field radiation based on the Wiener-chaos expansion method, rather than using effective medium theory (EMT). Previous studies on metamaterial based near-field radiation generally adopted EMT to approximate electromagnetic properties [81,88]. However, EMT approximation has two drawbacks: (i) It may not be applicable in the near-field because, instead of effective or averaged properties, inhomogeneous behaviors of individual sub-wavelength structures dominate the responses of metamaterials to the exponentially decaying evanescent waves. (ii) EMT is essentially an approximation which cannot provide detailed information on the electromagnetic fields in metamaterials. A direct numerical simulation is thus crucial for accurately predicting the near-field responses of complicated geometries like metamaterials.

3.2 Enhanced near-field heat transfer between an IR-SPR emitter and a hyperbolic metamaterial

Hyperbolic metamaterials are non-resonant and can potentially manipulate near-field radiation [34,85]. The effective permittivity of this type of metamaterials has a negative vertical component ($\epsilon_z < 0$) and positive horizontal components ($\epsilon_{x,y} > 0$), with the materials assumed to be uniaxial (i.e., $\epsilon_x = \epsilon_y = \epsilon_{x,y}$) for simplicity. Since ϵ_z and $\epsilon_{x,y}$ are opposite in sign, the dispersion relation for TM (transverse-magnetic, $H_z=0$) waves is a hyperbolic function

$$\frac{k_z^2}{\epsilon_{x,y}} - \frac{K^2}{|\epsilon_z|} = k_0^2, \quad (3.1)$$

where K is the lateral wave vector $K = \sqrt{k_x^2 + k_y^2}$, and k_0 is the wave vector in vacuum. As shown in Eq. (3.1), one intriguing property of hyperbolic metamaterials is that they allow propagating TM waves with no upper bound for K . The IR-SPR based near-field heat transfer is dominated by the contribution from the TM waves that have a purely imaginary k_z and a large surface wave vector K ($K > k_0$) [23]. These waves are evanescent in vacuum but can be converted into propagating waves by hyperbolic metamaterials for arbitrarily large K .

Hyperbolic metamaterials can be realized by a number of structures such as alternating metal-dielectric layers [85] and metal wire arrays (MWAs) [86,87]. In the infrared regime, metals behave like perfect electric conductors (PEC) with permittivity $\epsilon = -\infty + i\infty$. A metamaterial made of MWAs can have the hyperbolic dispersion given by Eq. (3.2) in a broad frequency band for $\omega < \omega_p$ without relying on the intrinsic resonant properties of metals. Here, ω_p is the equivalent plasma frequency of MWAs, which can be expressed by the wire period a

and the radius r as $\omega_p \approx \sqrt{2\pi c_0^2 / [a^2 \ln(a/r)]}$ [89]. The vertical components of the effective permittivity $\epsilon_{x,y}$ can be approximated as the vacuum permittivity ϵ_0 due to the negligible polarizability in x- or y- direction. However, the estimation of the parallel component ϵ_z is not straightforward. The local EMT model for “diluted metal wires” proposed by Pendry *et al.* [89] cannot interpret the dispersion of the propagating waves inside the MWAs [86,87]. Belov *et al.* [86] proposed a non-local EMT model for MWAs which requires evaluating the microscopic structure details

$$\epsilon_z(\omega, k_z) = \epsilon_0 \left(1 - \frac{\omega_p^2}{\omega^2 - c_0^2 k_z^2} \right) \quad (3.2)$$

which is always negative for $\omega < \omega_p$. If the period of MWAs is chosen to be hundreds of nanometers, ω_p of MWAs is typically in the visible range, and MWAs can maintain the hyperbolic dispersion in the infrared range.

The performance of MWAs can be evaluated by the photon local density of states (LDOS) above the surface of semi-infinite MWAs. According to Ref. [90], the photon tunneling rate through evanescent waves increases with the increase of the LDOS immediately above the surface of the thermal emitter/absorber. Therefore, by enhancing the LDOS, near-field radiative heat transfer can be increased. The LDOS, $\rho_i(d, K, \omega)$, at the distance d above the surface of a medium for parallel wave vector K and frequency ω is related by

$$\rho_i(d, K, \omega) \propto \text{Im}[r_{TM}^i] \exp(-\gamma d), \quad (3.3)$$

where r_{TM}^i is the Fresnel factor of the medium $i \in \{\text{emitter, absorber}\}$ for TM waves, and $\gamma = \sqrt{k_0^2 - K^2}$. Here, we ignore the contribution from the transverse-electric (TE) wave since the near-field heat transfer with an IR-SPR emitter is dominated by TM waves. Furthermore, the profile of the spectral heat flux $\Phi(\omega)$ between a thermal emitter and absorber separated by a vacuum gap d can be estimated by the product of the LDOS above the surface of each individual medium

$$\int_{k_0}^{\infty} dK^2 \cdot \rho_{emitter}(d, K, \omega) \cdot \rho_{absorber}(d, K, \omega) \quad (3.4)$$

Due to the hyperbolic dispersion, the LDOS above MWAs can be dramatically increased compared to that of bulk metals. However, the exact value of the LDOS of MWAs is difficult to be calculated based on the non-local EMT model (Eq. (3.2)), because the calculation of the Fresnel factors of non-local media requires to scrutinize the structure details [91]. Hence, we consider a limiting case with local dispersion relation to predict the general trend of the LDOS above MWAs. If the period of MWAs is infinitely small, the equivalent plasma frequency approaches infinity, $\omega_p \rightarrow \infty$, then the effective permittivity of this limiting case of MWAs is $\varepsilon_x = \varepsilon_y = \varepsilon_0, \varepsilon_z = -\infty$ according to Eq. (3.2). The limiting case is a reasonable approximation to the actual MWAs in the near-field because it can lead to the same dispersion relation of the propagating waves inside MWAs as that of the actual cases when $\omega < \omega_p$ [86,87]. The LDOS can thus be easily evaluated by calculating the Fresnel factor for an anisotropic medium with local EMT model [84]. In Figure 3-2, we estimate the LDOS at 100nm above the surface of the semi-infinite SiC, gold and the limiting case of MWAs by calculating $\text{Im}[r_{TM}^i] \exp(-\gamma d)$. The

LDOS of MWAs is largely enhanced in a broad frequency band compared to that of gold. The LDOS of SiC has a sharp peak at the SPR frequency. The LDOS of MWAs as shown in Figure 3-2 is almost evenly distributed in the infrared regime. Hence, MWAs can strongly interact with an IR-SPR emitter (e.g., SiC) and simultaneously maintain the monochromatic near-field heat transfer with the IR-SPR emitter, according to Eq. (3.4).

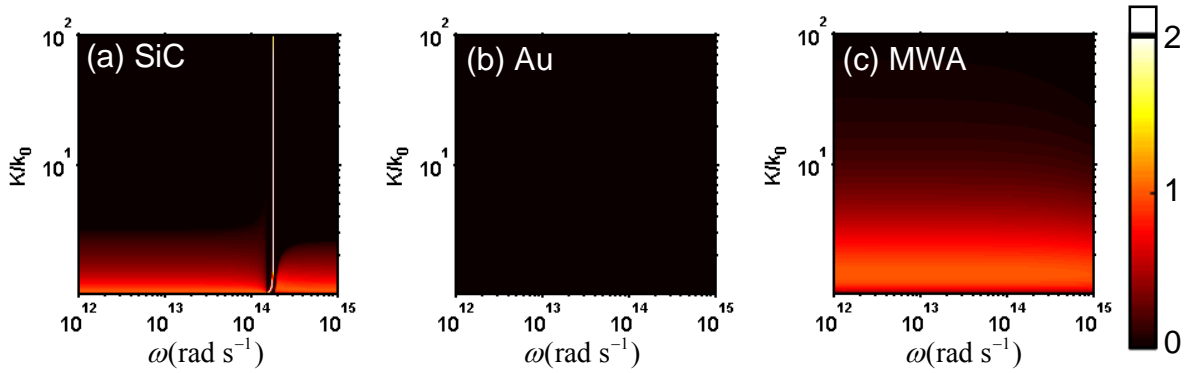


Figure 3-2: Plot of the expression $\text{Im}[r_{TM}] \exp(-\gamma d)$ to estimate the photon local density of state (LDOS) at $d = 100\text{nm}$ above the surface of semi-infinite (a) SiC, (b) Au, and (c) limiting case of metal wire arrays (MWAs).

3.3 Simulation Results

Here, we investigate the near-field radiative heat transfer between an IR-SPR emitter and MWAs placed in vacuum, as shown in Figure 3-4(a). The IR-SPR emitter is assumed to be a $1\mu\text{m}$ thick plate. Metal wires are aligned in the z-direction with radius $r=50\text{nm}$ and period $a=300\text{nm}$. The IR-SPR emitter is kept at 300K , and the MWAs are at 0K . The heat flux between them is evaluated by calculating the amount of energy transmitted into the MWAs. As the MWAs are at a finite temperature, the net heat flux can be solved by the reciprocity of radiative

heat transfer [50]. In our simulation, the current modes in the IR-SPR emitter are chosen in sinusoidal forms (see Appendix) because of the resulting high convergence speed of numerical simulation. The MWAs at 0K do not emit thermal radiation, and we only consider their electromagnetic response in the infrared range. The metal wires in our simulation are assumed to be PEC wires, which is verified by comparing the energy fluxes into PEC and gold wire arrays for current *Mode 1*. We find that the results from PEC and gold wires are almost the same, as shown in Figure 3-3.

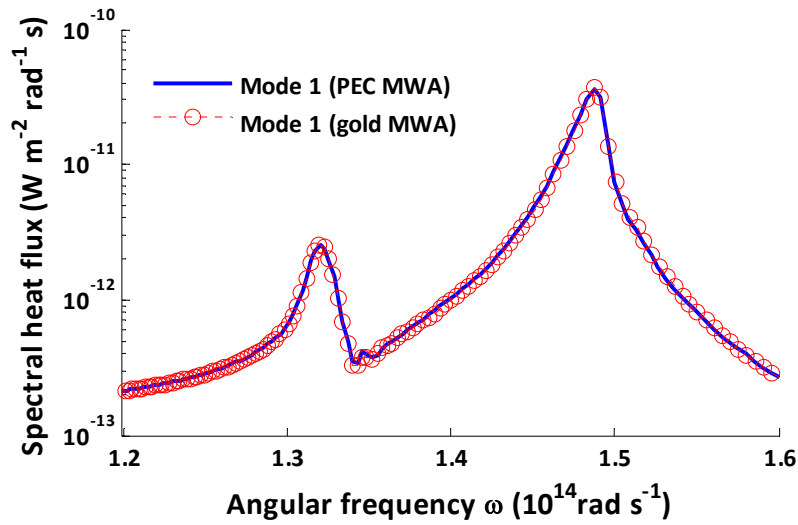


Figure 3-3: Spectral heat flux into PEC MWA and gold MWA due to current Mode 1. The MWAs have the same geometry: wires radius $r = 50\text{nm}$, wires period $a = 300\text{nm}$. The vacuum gap size d between the MWAs and SiC plate is 100nm .

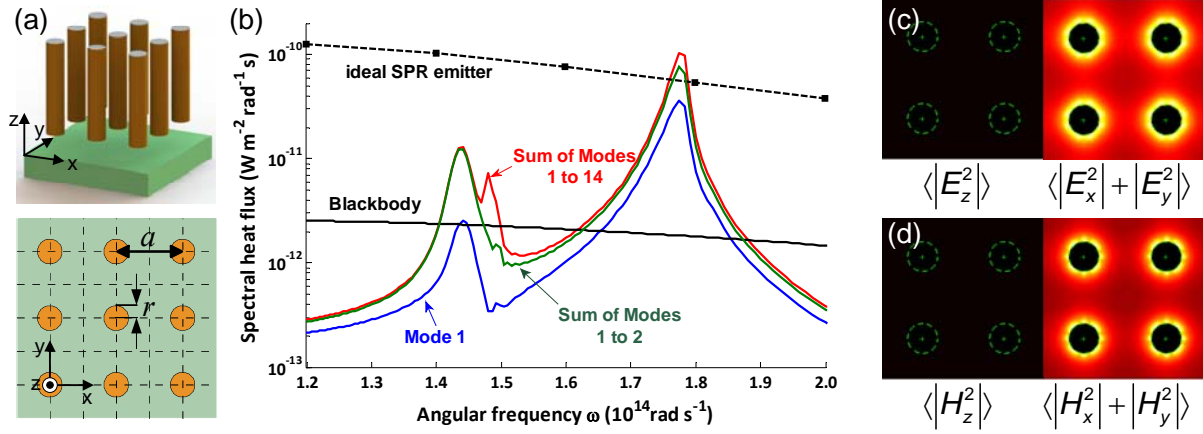


Figure 3-4: (a) Schematic diagram (3D view and top view) of the SiC plate heat emitter (at 300K) and the metal wire arrays heat absorber (at 0K) separated by a vacuum gap. Metal wires have infinite length, radius $r = 50\text{nm}$ and period $a = 300\text{nm}$. (b) Spectral heat flux into metal wire arrays from sinusoidal current modes in the SiC plate at a 100nm vacuum gap. (c), (d) Electric and magnetic field profiles in metal wire arrays at the SPR frequency ($1.78 \times 10^{14}\text{rad/s}$) of SiC, measured at the plane $2\mu\text{m}$ above the gap.

The spectral heat flux between a SiC emitter and the MWAs with a 100nm gap is plotted in Figure 3-4(b). The first current mode (dipole-like mode) contributes $\approx 40\%$ of the total heat flux, and the first two modes contribute $\approx 80\%$. The monochromatic feature of heat transfer is denoted by the peaks corresponding to the symmetric and antisymmetric SPR modes of the $1\mu\text{m}$ thick SiC plate, where near-field heat transfer clearly exceeds the Planck law. The broadband response from the MWAs can be found by introducing an “ideal SPR emitter” that has a frequency-independent permittivity equal to $-1+bi$. The real part, -1, indicates that the material supports SPR at any frequency, and the imaginary part b is an arbitrary number associated with the magnitude of thermal induced currents. In Figure 3-4(b), b is assumed to be 0.1. The spectral

heat flux between the “ideal SPR emitter” and the MWAs is plotted in Figure 3-4(b). Heat transfer enhancement is observed for all the frequencies of interest in the infrared regime.

The mechanism with which MWAs absorb heat is directly elucidated in our simulations. The field profiles inside the MWAs at the SPR frequency of SiC are shown in Figure 3-4(c) and (d). The highly spatial dispersion of MWAs leads to the TEM (transverse electromagnetic, $E_z = H_z = 0$) propagating modes [86]. At the frequencies below the equivalent plasma frequency ω_p , the hyperbolic dispersion relation becomes flat as $k_z^2 = k_0^2$. Thus, the MWAs support the TM waves with arbitrary K propagating only along the z direction (i.e., TEM waves) [87]. For real MWAs (e.g., gold wire arrays), they couple the TM waves (both propagating and evanescent components) from the IR-SPR emitter into the TEM waves propagating along the wires, which will eventually be absorbed by metals due to the ohmic loss. In the frequency range of thermal radiation, the MWAs can be viewed as a system of coupled low-loss transmission lines [86]. The decay length L_d of the gold wires in Figure 3-4 is estimated to be on the order of $100\mu\text{m}$ by the approach described in Ref. [19] that $L_d \approx \text{Im}[k_z]^{-1}$ for the TEM waves with $K = 0$. With this low-loss feature, MWAs can also be used as “near-field thermal waveguides” which can couple the evanescent radiative energy at the nanoscale and transfer it to a macroscopic scale.

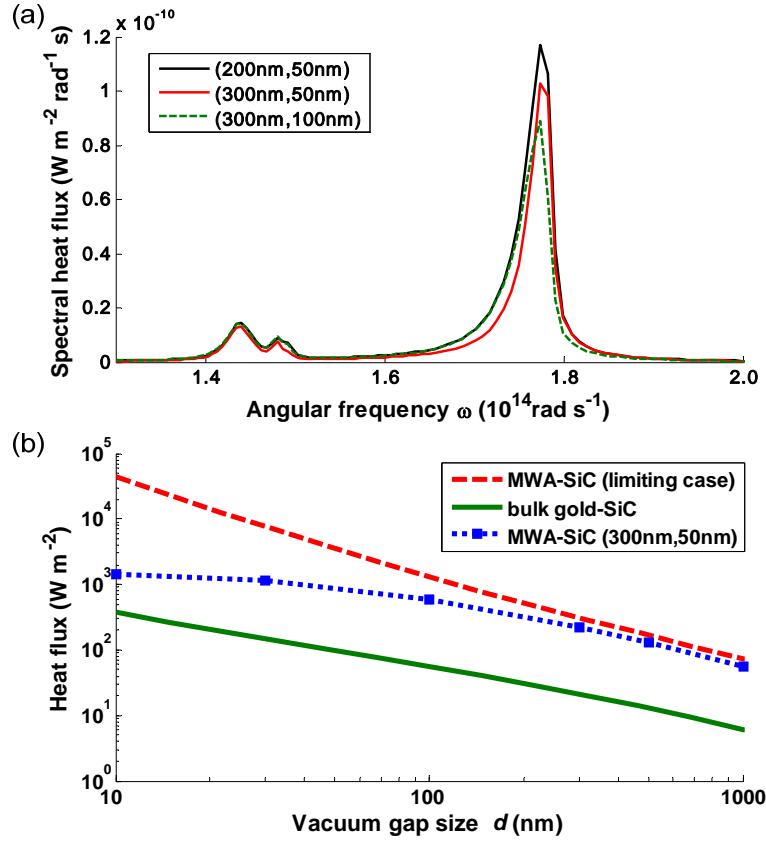


Figure 3-5: (a) Comparison between heat fluxes from $1\mu\text{m}$ thick SiC plate (at 300K) to MWAs (at 0K) and semi-infinite gold plate (at 0K), as a function of the vacuum gap size. Also the performance of ideal MWAs is plotted for reference. (b) Spectral heat flux between the SiC plate and the MWAs with different (a, r) at a 100nm gap. Here a, r denote the period and the radius of metal wires, respectively.

In Figure 3-5(a), we plot the total heat flux between the SiC IR-SPR emitter and the MWAs against gap sizes. Compared with the SiC-gold case, MWAs can enhance the near-field heat transfer with SiC by one order of magnitude without having to match the SPR in SiC. These results show that MWAs significantly modify the radiative thermal properties of bulk metals in

the near-field. For a fixed gap, the performance of MWAs is determined by wire density and size. As shown in Figure 3-4(c) and (d), the transmitted energy in the MWAs is concentrated on the surface of each wire. MWAs with smaller radii and periods are expected to absorb more energy. This trend is demonstrated by calculating the spectral heat fluxes to MWAs with different wire radii and periods (Figure 3-5(b)). The performance of MWAs can be maximized when the period of the wires is infinitely small, which is the limiting case presented in Section 3.2. The radiative heat transfer between this limiting case of MWAs and a SiC emitter can be calculated analytically by modeling the MWAs as an anisotropic medium with local dispersion relation based on EMT [84,92], as shown in Figure 3-5(a). At large gaps, the limiting case EMT approximation gives an accurate prediction. However, for small gaps, it overestimates the heat transfer in actual cases. Therefore, a direct numerical simulation is required to accurately predict the performance.

3.4 Conclusion

We described a hyperbolic metamaterial based heat emitter/absorber made of metal wire arrays (MWAs), which can greatly enhance near-field heat transfer with IR-SPR materials. Rather than match the resonant frequencies of IR-SPR materials, MWAs are non-resonant and have enormous enhancement of the LDOS in a broad frequency range. We directly simulated the near-field radiative heat transfer between MWAs and an IR-SPR emitter based on the Wiener-chaos expansion method. The direct numerical simulation is demonstrated to be critical for accurately predicting the near-field radiation of complex geometries like metamaterials. Manipulation of near-field radiation using metamaterials has been considered in theory for a long time but is difficult to be experimentally realized. The results presented in this paper provide a

feasible way to achieve the metamaterials which can work in the near-field and enhance radiative heat transfer beyond material limitation.

3.5 Appendix: Current Modes

In the simulation of the heat transfer between the IR-SPR emitter and MWAs, as shown in Fig. 5(a), the orthonormal basis $\{f_i\}$ is defined in the volume of the $1\ \mu\text{m}$ -thick SiC plate. Since the structure is periodic in x,y direction, the infinite plate can be divided into cuboid cells with a height of $h = 1\ \mu\text{m}$ and a length and a depth of $a/2$. Thus, the orthonormal basis $\{f_i\}$ for this infinite plate can be chosen as the union of the orthonormal basis for all the cuboid cells.

Consider the cuboid cell centered at $(x_c, y_c) = \left(\frac{a}{4}[2c_x + 1], \frac{a}{4}[2c_y + 1] \right)$, where c_x and c_y are integers. The orthonormal basis for this cell is chosen as the Fourier-series basis $\{f_{l,m,n,\mathbf{k},c_x,c_y}\}$,

where

$$f_{l,m,n,c_x,c_y}(x, y, z) = H_l(x - x_c)P_m(y - y_c)Q_n(z + h)\mathbf{k} \quad (3.5)$$

$$H_l(x) = \begin{cases} \frac{1}{\sqrt{a}} & l = 0 \\ \sqrt{\frac{2}{a}} \cos\left[\frac{l\pi x}{a}\right] & l = 1, 2, 3 \dots \end{cases}$$

$$P_m(y) = \begin{cases} \frac{1}{\sqrt{b}} & m = 0 \\ \sqrt{\frac{2}{b}} \cos\left[\frac{m\pi y}{b}\right] & m = 1, 2, 3 \dots \end{cases}$$

$$Q_n(z) = \begin{cases} \frac{1}{\sqrt{c}} & n = 0 \\ \sqrt{\frac{2}{c}} \cos\left[\frac{n\pi z}{c}\right] & n = 1, 2, 3 \dots \end{cases}$$

Here, $x - x_c, y - y_c \in [-a/4, a/4]$, $z \in [-h, 0]$, $\mathbf{k} \in \{\mathbf{e}_x, \mathbf{e}_y, \mathbf{e}_z\}$ is the unit vector of 3D space. Then the current modes in the SiC plate become $\{j_{l,m,n,\mathbf{k},c_x,c_y}(r, \omega) = V(\omega, T)f_{l,m,n,\mathbf{k},c_x,c_y}(r)\}$.

Due to the periodicity and symmetry of the structure, the current modes in different cuboid cells have the same contribution to thermal radiation. Therefore, we only need to evaluate the current modes in one cell, which can be chosen as $c_x = c_y = 0$. Since the current modes in sinusoidal forms can be viewed as a multipole expansion, they can be divided into different groups with ranking numbers, which are similar to the orders in the multipole expansion. The top 14 groups of current modes are listed in Table I. For example, *Mode 1* denotes the group of current modes $\{j_{l,m,n,\mathbf{k},c_x,c_y}\}$ with $l = m = n = 0$. It can be viewed as the term of dipole approximation, which is similar to the concept mentioned in Ref. [55].

Mode No.	l	m	n
1	0	0	0
2	0	0	1
3	0	0	2
4	0	0	3
5	0	0	4
6	0	0	5
7	0	1	0
8	1	0	0
9	0	1	1
10	1	0	1
11	0	1	2
12	1	0	2
13	1	1	0
14	1	1	1

Table 1: The current modes used to expand the cuboid unit cell.

4 Thermal graphene plasmonic interconnects

4.1 Introduction

The manipulation of optical fields and energy flow of light plays a pivotal role in communication and information technologies. Among various means of controlling light, surface plasmons (SPs), known as the coupled excitations of photons and free electrons, enable confinement and control of electromagnetic energy at the sub-wavelength scale, and thus bridge optics and nanotechnology. Noble metals such as gold and silver are widely used plasmonic materials in the visible and near-infrared range. However, metal SPs in the infrared and terahertz range (e.g., dual-conductor transmission line modes [93]) usually have a large wavelength comparable to that of free-space photons, and thus cannot truly squeeze the light down to deep sub-wavelength scale, especially in propagating direction. Recent studies have shown that graphene, a two-dimensional single layer of carbon atoms, can support propagating SPs with unprecedented properties at infrared and terahertz frequencies due to the strong interactions between graphene and low frequency photons [66,94]. More importantly, graphene surface plasmons (GSPs) can be confined to an extremely small dimension, on the order of 10^2 times smaller than the diffraction limit, and can be tuned over a wide range by gating or doping [66]. Hence, graphene has emerged as a promising plasmonic material for tunable infrared or terahertz light sources [95], sub-wavelength optical circuits [96], robust and cost-effective photodetectors for terahertz radiation [97–102], and nanoelectronic devices with strong light-matter interactions [103], to name a few.

In spite of the unique properties of GSPs, launching GSPs remains challenging because of the large wavevector mismatch between GSPs and free-space light waves [67]. Moreover, active light sources currently used for exciting GSPs such as infrared lasers cannot be easily

miniaturized and integrated into optoelectronic circuits [94,104]. Since GSPs exist in the infrared and terahertz regime, they can be thermally excited by the infrared evanescent waves emitted from an object [36]. However, compared with active light sources like lasers, thermal emission usually has a broad spectrum with low output power limited by the blackbody radiation [1]. In this paper, by directly solving stochastic Maxwell's equations, we show that thermal GSPs can be efficiently excited and have monochromatic and tunable spectra. Furthermore, we demonstrate, for the first time, that thermal energy can be employed to transmit information via GSPs, enabling information communication with negligible cross-talks. These results provide us new understanding of graphene in the areas of thermal science and nano optics, implying that we can harness thermal energy to build various graphene plasmonic devices.

4.2 Thermal excitation of monochromatic and tunable GSPs

The key for efficiently launching monochromatic GSPs is to utilize the resonance of nanoscale thermal emitters. Previously, graphene nanoribbons and nanodisks have been discovered as high-Q plasmonic cavities, whose resonance frequencies can be tuned by designing their Fermi level and geometry [66]. Here, we employ graphene nanoribbon thermal emitters (surface plasmon cavities in 2D) to excite GSPs on a coupled graphene sheet. To directly simulate the thermal radiation energy transfer and field intensity of graphene, we solve stochastic Maxwell's equations by both the Fluctuating-Surface-Current (FSC) formulation and the Wiener-Chaos-Expansion (WCE) formulation under the framework of the 2D boundary element method (BEM) [33,39]. As shown in the schematic of Figure 4-1(a), a graphene nanoribbon thermal source with width W and Fermi level E_F is placed in proximity to a

graphene sheet at a nanoscale gap d . Similar suspended graphene nanoribbon structures have been experimentally realized in Refs. [105–107]. Electromagnetic energy output from a thermal source is usually understood as the radiation from thermally induced random dipoles in the source [25]. When the nanoribbon emitter is close to graphene, the evanescent photons with large wavevector produced by the random dipoles enable the excitation of surface waves on the graphene sheet. In addition, thermal emission from a heat source in the near-field (at a nanoscale gap) is not limited by the blackbody radiation [23].

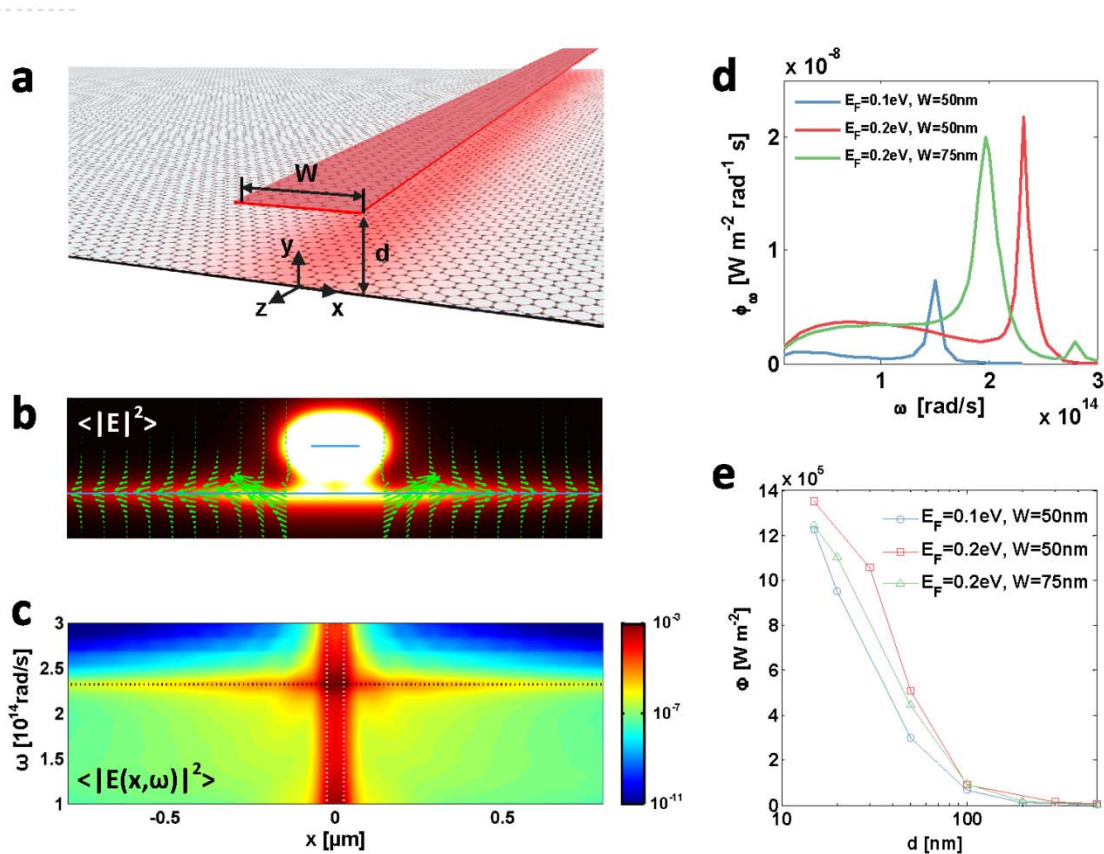


Figure 4-1: (a) Schematic of a graphene nanoribbon thermal emitter and a graphene sheet. (b) Electric field intensity $\langle |E|^2 \rangle$ (color plot) and Poynting vector (green quiver plot) due to the thermal emission from the nanoribbon emitter. Blue lines indicate the locations of graphene

ribbon and sheet. (c) Spectral field intensity $\langle |E(x, \omega)|^2 \rangle$ (in the unit of $V^2 \cdot m^{-2} \cdot rad^{-1} \cdot s$ and plot in log scale) along the x direction and at 15nm above the graphene sheet. The white dashed lines indicate the location of the graphene nanoribbon emitter. The black dashed line indicates the peak frequency ($\omega = 2.3 \times 10^{14} rad/s$) of the thermally excited GSPs. (d) Spectral energy fluxes of the thermally excited GSPs by graphene nanoirbbon emitters with different W and E_F , at the same gap $d = 50nm$. (e) The total power Φ (normalized to the area of nanoribbon) of the thermally excited GSPs as a function of d .

For the case of $d = 50nm$, $W = 50nm$, and $E_F = 0.2eV$, the thermal radiation field intensity and energy flow profiles (cross-section view) due to the graphene nanoribbon emitter are illustrated in Figure 4-1(b). Here, the nanoribbon thermal emitter and the graphene sheet are maintained at 500 K and 0 K, respectively, in order to demonstrate the effect of the nanoribbon thermal source. The mobility of graphene is set to be $10,000cm^2/(V \cdot s)$ that can be achieved by exfoliated graphene samples. The field intensity profile in Figure 4-1(b) shows that the thermal radiation of the nanoribbon emitter excites the confined surface waves on the graphene sheet, which can spread a long distance from the emitter. The Poynting vector profile (green arrows in Figure 4-1(b)) further confirms that the surface waves indeed carry energy and propagate away from the nanoribbon emitter. Due to near-field effect, the output energy flux from the nanoribbon emitter to the sheet is $7 \times 10^5 W/m^2$ (total power normalized to the ribbon area), which is two orders of magnitude larger than the blackbody limit. Moreover, the graphene nanoribbon thermal emitter is essentially an extremely efficient source for exciting graphene surface waves because of the significant enhancement of the photon local density of states (PLDOS) in the near-field [90]. In this case, almost 100% of the energy output from the nanoribbon is converted to

surface waves through evanescent photons, and only 0.01% of the energy output leaks to the far-field surroundings due to propagating photons.

To investigate the spectrum of the thermally excited surface waves, the spectral field intensity along the graphene sheet is plotted in Figure 4-1(c). It can be clearly seen that only the field intensity at $\omega = 2.3 \times 10^{14}$ rad/s spreads a long distance in the x direction on the graphene sheet (highlighted by the black dashed line in Figure 4-1(c)), which indicates the monochromatic excitation of the propagating GSPs. By designing the cavity modes (e.g., tuning the Fermi level and ribbon size), the peak frequency of the thermally excited GSPs by the graphene nanoribbon can also be controlled, as shown in Figure 4-1(d). For example, the Q factor is estimated to be ~ 20 for the graphene ribbon cavity with $E_F = 0.2$ eV and $W = 50$ nm (the red curve in Figure 4-1(d)). Despite the monochromatism, the thermally excited GSPs are incoherent because the source dipoles inside the emitter are random. Furthermore, the power of the thermally excited GSPs significantly depends on the ribbon-sheet separation due to the near-field effect. As shown in Figure 4-1(e) for graphene ribbons with different sizes and Fermi levels, the total power dramatically increases with reduced gap size.

To understand the mechanism of the thermal excitation of monochromatic GSPs, we perform the mode expansion of the thermally emitted photons in the (k_z, ω) space. There are two fundamental reasons to perform the mode expansion in the (k_z, ω) space: (1) since the complex graphene structures proposed in this paper are 2D invariant (in the z direction), only z-component of wavevector k_z and frequency ω of each photon are conserved; (2) The 2D BEM (together with the FSC formulation and the WCE method) allows us to calculate the exact contribution from each photo mode (k_z, ω) to the energy flux and the field intensity.

The total surface waves excited on the graphene sheet in Figure 4-1(b) include the contributions from “long-range” propagating surface waves and “quickly decaying” surface waves. For the excited GSPs on the graphene sheet in Figure 4-1(a) (except the projection area of the nanoribbon), its surface wavevector, $k_s = \sqrt{k_x^2 + k_z^2}$, should be equal to

$$k_{GSP} = \frac{\omega}{c_0} \sqrt{1 - \frac{4\epsilon_0}{\mu_0 \sigma_g^2(\omega, T)}},$$

the surface wave vector of intrinsic GSPs on a single graphene sheet.

Its k_x needs to be a real number in order to "propagate" or carry energy in the x direction. Therefore, we divide the mode space (k_z, ω) into two regions by the dispersion curve $k_{GSP}(\omega)$ of the intrinsic GSPs on a graphene sheet, as shown by the white curves in Figure 4-2(a). The first region corresponds to the modes with $k_z < k_{GSP}$, which are capable to excite the propagating surface waves with real k_x . The second region represents the modes with $k_z > k_{GSP}$, which can only excite the quickly decaying surface waves due to the imaginary k_x . To further clarify the physical meaning of the two mode regions in Figure 4-2(a), we plot the thermal radiation field profiles $\langle |E|^2 \rangle$ due to the modes from these two regions, as shown in Figure 4-2(c). It can be clearly seen that only the first mode region ($k_z < k_{GSP}$) contributes to the excitation of the propagating GSPs, while the second mode region ($k_z > k_{GSP}$) only leads to the quickly decaying surface waves, which are highly localized near the nanoribbon and do not carry substantial energy in the x direction.

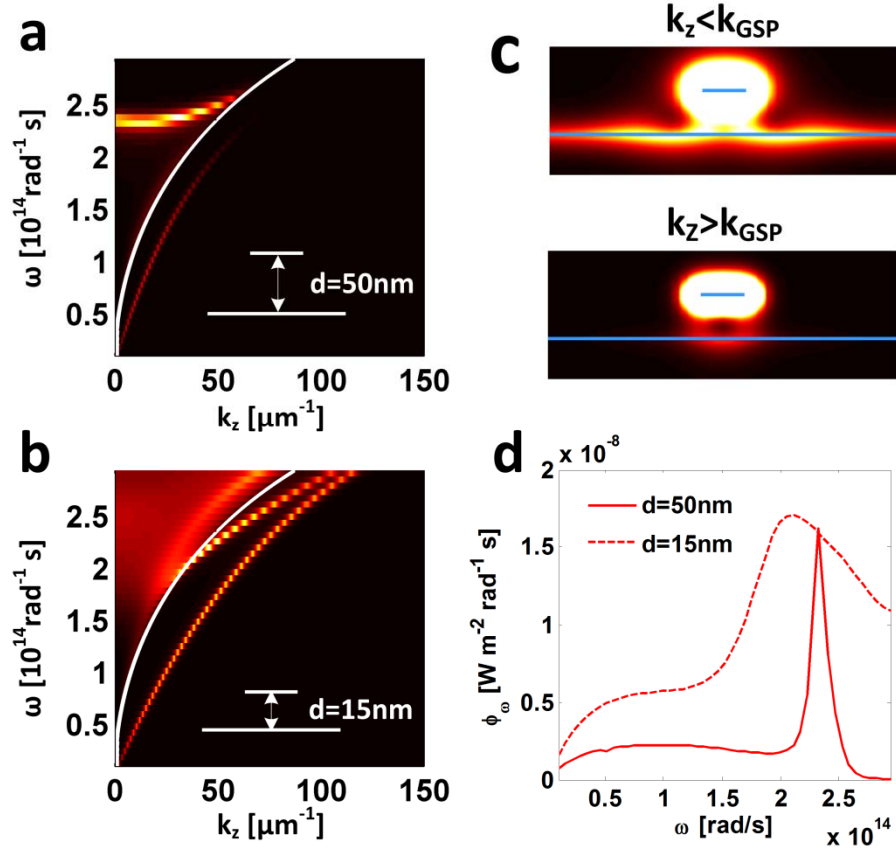


Figure 4-2: (a) and (b) Contribution from each photon mode (k_z, ω) to the thermal excitation of GSPs on the graphene sheet, for (a) $d = 50\text{nm}$ and (b) $d = 15\text{nm}$, respectively. The graphene nanoribbon emitter has $E_F = 0.2\text{eV}$ and $W = 50\text{nm}$. The white curves represent the dispersion relation of intrinsic GSPs on a single graphene sheet. (c) Thermal radiation field profile due to the photon modes from the two regions: $k_z < k_{GSP}$ and $k_z > k_{GSP}$. (d) The spectral energy flux carried by the surface waves with $k_z < k_{GSP}$ for both $d = 50\text{nm}$ and $d = 15\text{nm}$ cases.

As a result, the upper limit of the output power exciting propagating GSPs can be calculated by integrating the photon energy flux due to the first mode region ($k_z < k_{GSP}$). The corresponding upper bound of the excitation efficiency of propagating GSPs is estimated to be

70% for the case with $d = 50\text{nm}$, where the excitation efficiency is defined as the ratio between the energy flux carried by propagating GSPs and the total energy output from the nanoribbon emitter. Here, we also want to emphasize that the exact excitation efficiency of propagating GSPs depends on both the graphene material property and the structure geometry in real cases.

The separation between the graphene nanoribbon emitter and the graphene sheet can also strongly influence the excitation of GSPs. In order to excite GSPs, a small gap is required because only the evanescent photons can match the large wavevector of GSPs. However, if the gap is too small, the monochromatism of excited GSPs vanishes due to the strong coupling between the nanoribbon and the sheet. In Figure 4-2(d), we plot the spectral energy flux carried by the surface waves with $k_z < k_{GSP}$ for both $d = 50\text{nm}$ and $d = 15\text{nm}$. The frequency band of GSPs for $d = 15\text{nm}$ becomes much broader, compared with the $d = 50\text{nm}$ case. The mechanism can also be revealed by the results of mode expansion. For the $d = 50\text{nm}$ case, the monochromatism of the thermally excited GSPs is attributed to the narrow bright area in the first mode region ($k_z < k_{GSP}$) in Figure 4-2(a), which corresponds to the first-order cavity mode (or edge mode) of an individual graphene nanoribbon due to the optical confinement in the x direction. This consistence of the resonance modes in a graphene ribbon-sheet system with an individual graphene ribbon indicates the weak coupling between the ribbon and the sheet. For the $d = 15\text{nm}$ case, the resonance modes of the graphene nanoribbon are quite different from those of the 50nm gap due to the strong coupling between the ribbon and the sheet. As shown in Figure 4-2(b), there exist no single “resonance modes” in the first mode region ($k_z < k_{GSP}$) which contribute to the excitation of propagating surface waves.

4.3 Information communication via thermal GSPs

Based on the properties of the GSPs that are thermally excited by a graphene nanoribbon emitter, we design and demonstrate "thermal GSP interconnects". Superior to conventional optical circuits, GSP interconnects can achieve the thinnest possible platform and field confinement on the order of 10 to 100nm, 100 times smaller than the infrared wavelength. In comparison with conventional SP interconnects, GSP interconnects work at the infrared range, and they can be easily tuned by modifying the Fermi level of graphene. To prove the concept, we study the systems which are composed of graphene nanoribbon transmitters and receivers. All the nanoribbons are separated from the graphene waveguide with a proper gap size so that they are all weakly coupled to the waveguide. A graphene nanoribbon transmitter transmits signals by being heated to a high temperature (e.g., by the Joule heating from an electrically biased graphene nanoribbon) and then exciting the GSPs thermally. Likewise, the graphene nanoribbon transmitter can be electrically modulated at high frequency, considering the extremely small thermal mass of the graphene nanoribbon. A graphene nanoribbon receiver receives or detects signals by absorbing the energy carried by GSPs. To date, graphene based infrared light detectors have been demonstrated [97–102], all of which are required to absorb the light directly by graphene. Furthermore, due to the resonance property of graphene nanoribbons, the proposed thermal GSP interconnect allows us to selectively transmit information at the desired spatial and spectral positions.

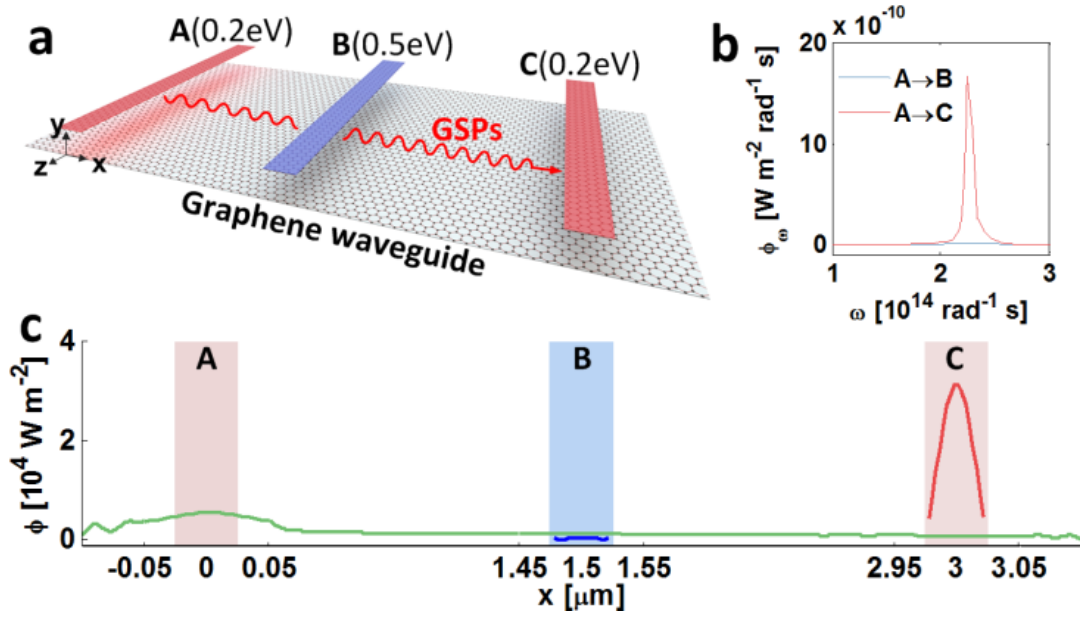


Figure 4-3: (a) Schematic of a basic demonstration in which graphene nanoribbon A is a transmitter, and nanoribbons B, C are receivers. The graphene sheet with a finite width of 4 μm serves as a GSP waveguide. The gap between the nanoribbons and the sheet is 50 nm. (b) Spectral energy fluxes for $A \rightarrow B$ (blue curve) and $A \rightarrow C$ (red curve). The results are normalized to the area of the nanoribbon transmitter. (c) Local energy flux profiles on receiver B (blue curve), receiver C (red curve), and graphene waveguide (green curve). The red and blue regions indicate the locations of the graphene ribbons.

The first system illustrated in Figure 4-3(a) is composed of one transmitter **A** and two receivers **B** and **C**, all of which are 50 nm wide nanoribbons and are separated from the graphene sheet waveguide with a 50 nm gap. To demonstrate the idea of long-range communications, the distances between **A** to **B** and **B** to **C** are set to be 1.5 μm, which are long enough to prevent the direct near-field coupling between adjacent nanoribbons. The Fermi level and mobility of the graphene sheet waveguide are set to be $E_F = 0.6\text{eV}$ and $\mu = 10,000\text{cm}^2/(\text{V}\cdot\text{s})$, respectively. In

this case, the propagation distance of GSPs reaches $10\mu\text{m}$. Transmitter **A** is at 500 K, and the rest of the system, including the graphene waveguide, receivers **B** and **C**, is maintained at 300 K. Although the heated graphene waveguide can also excite GSPs thermally, they have no impact on receivers because there is no net energy flow from the waveguide to receivers. The information cannot be transferred without net energy flow in a reciprocal thermal system [108]. Transmitter **A** and receiver **C** have the same resonance frequency because both the Fermi levels are equal to 0.2eV, whereas receiver **B** is designed to have a different resonance frequency by setting its Fermi level to be 0.5eV. Practically, the Fermi level of graphene can be tuned by chemical doping or electric gating [109]. The energy flux spectra between transmitter **A** and receivers **B** and **C** are plotted in Figure 4-3(b). Although receiver **B** is closer to transmitter **A** than receiver **C**, receiver **C** receives much more energy than receiver **B** due to the match of graphene ribbon resonance frequency. The weak coupling between nanoribbons ensures that the information communication between transmitter **A** and receiver **C** is not interfered by receiver **B**. The weak coupling also leads to the high efficiency of the waveguide. The local energy flux distribution at the peak frequency of energy flux received by receiver **C** ($\omega = 2.3 \times 10^{14}$ [rad/s]) is shown in Figure 4-3(c). The energy dissipated in the graphene waveguide underneath receiver **C** (green curve) is negligible compared to the energy absorbed by receiver **C** (red curve). The total thermal energy fluxes from transmitter **A** to receivers **B** and **C** are calculated to be $3.7 \times 10^2 \text{ W/m}^2$ and $1.8 \times 10^4 \text{ W/m}^2$, respectively, where the results are normalized to the area of the receiver. The high energy flux results from the near-field effect between the graphene ribbon and sheet, which has been demonstrated to be several orders of magnitude larger than the blackbody radiation. Quantitatively, the energy flux from transmitter **A** to receiver **C** is negligibly small (3.1 W/m^2) if the graphene sheet waveguide is absent. The dominant energy dissipation mechanism in this

system is the intrinsic loss of GSPs on the graphene waveguide, which can be reduced by using high-mobility graphene.

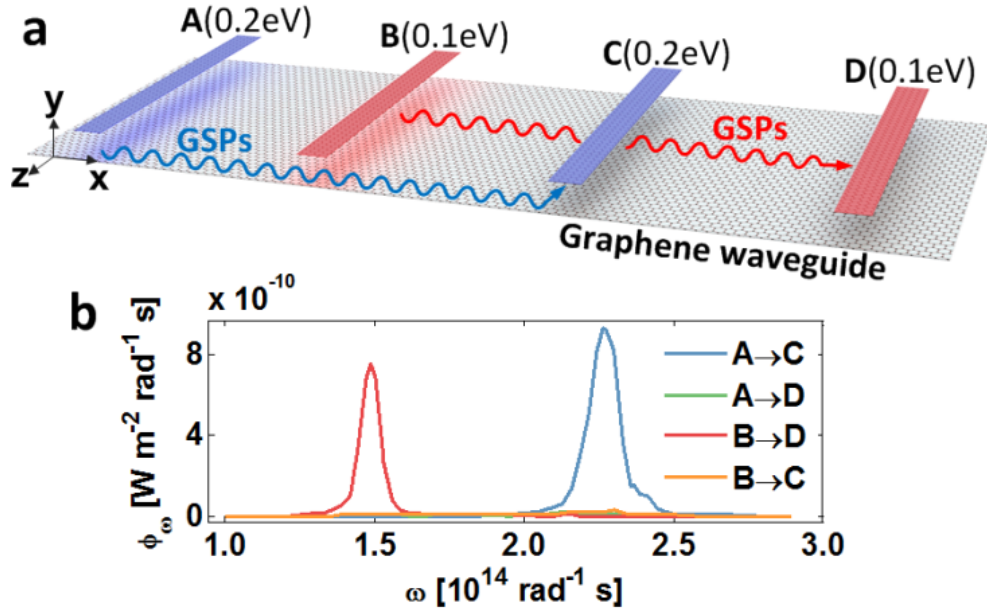


Figure 4-4: (a) Schematic of two graphene nanoribbon transmitters and two nanoribbon receivers. The graphene sheet waveguide has the finite width of $6.4\mu\text{m}$. (b) Spectral energy transfer for different transmitter and receiver pairs. The total energy fluxes for $A \rightarrow C$ and $B \rightarrow D$ are $1.3 \times 10^4 \text{W/m}^2$ and $6.6 \times 10^3 \text{W/m}^2$, respectively. The "cross-talk" energy fluxes for $A \rightarrow D$ and $B \rightarrow C$ are $4.4 \times 10^2 \text{W/m}^2$ and $7.6 \times 10^2 \text{W/m}^2$, respectively. The results are normalized to the area of the corresponding nanoribbon transmitter.

The monochromatism of thermally excited GSPs allows the multi-channel thermal information communication on a single waveguide, providing the possibility of integrating multiple graphene based thermo-plasmonic devices together to form a complex GSP interconnection system. Consider a system with two transmitters **A** and **B** and two receivers **C**

and **D**, as shown in Figure 4-4(a). The Fermi levels of receivers **A** and **C** are set to be 0.2eV, whereas the Fermi levels of receivers **B** and **D** are set to be 0.1eV. The width of the nanoribbons, the gap between the nanoribbons and the graphene waveguide, and the material properties of the graphene waveguide are chosen to be same with the previous system in Figure 4-3. The graphene nanoribbons are also separated from their adjacent nanoribbon by a large distance of $1.5\mu\text{m}$. The energy flux spectra of this system are plotted in Figure 4-4(b). Since thermally excited GSPs by transmitters **A** and **B** are monochromatic at different frequencies, the crosstalk energy transfer of **A**→**D** or **B**→**C** is about one order of magnitude smaller than the energy transfer through the desired channels (**A**→**C** or **B**→**D**), as shown in Figure 4-4(b).

4.4 Conclusion

In summary, thermal excitation of GSPs provides unprecedented opportunities for both thermal science and nanophotonics. Our numerical calculations demonstrate that thermal energy can be efficiently converted into the monochromatic and tunable propagating GSPs. Therefore, the plasmonics theory/methods can be applied to manipulate the thermal energy (e.g. GSP waveguide, GSP modulator, GSP detector, etc.). Graphene nanoemitters can be designed to have specific output spectra as guided by the optical cavity theory. More importantly, the power of thermally excited GSPs is not limited by the blackbody radiation due to near-field energy transfer. While the exfoliated graphene samples with high mobility demonstrates the potential to be infrared SP waveguides, other low-loss infrared SPs waveguides (e.g. dual-conductor transmission line metal waveguide) can also be adopted to transmit thermal signals in this scenario. This is because the near-field waves radiated by the graphene nanoemitter can also

excite the propagating SPs transmission-line modes. As a result, “thermal GSP interconnects” can be realized to effectively harness thermal energy and use it to transmit information.

5 Quasi-Normal Mode Theory for Thermal Radiation from Lossy and Dispersive Optical Resonators

5.1 Introduction

A thermal light source like a blackbody or the incandescent filament of a light bulb usually has a broad emission spectrum. However, in many energy applications such as infrared sensing [110], thermophotovoltaics [20,111], radiation cooling [112] and thermal circuits [37,79], thermal emission is in general required to be much narrower than that of a blackbody. A common paradigm for realizing narrow band thermal radiation is to utilize optical resonators including optical antennas [113], photonic crystal cavities [114], and graphene nanostructures [37,115]. According to the Purcell effect [24], thermal radiation from an optical resonator can be dramatically modulated by the resonance mode designed in the infrared range, leading to the narrow band thermal emission peaking at the resonant frequency. Since thermal radiation is intrinsically weaker than the infrared light from the light sources driven by electrical power, e.g. laser or LED, it is critical but challenging to maximize the emission power of a narrow band thermal emitter. To reveal the general principle of maximizing the thermal radiation from an optical resonator, a semi-analytical formalism based on coupled mode theory has recently been proposed to phenomenologically model an optical resonator thermal emitter as a general resonant system with different energy loss mechanisms [79,114,116,117]. It was discovered that the peak of radiation intensity in an emitter reaches a maximum when the energy loss rate to an absorber (or far-field background) is equal to the one to the emitter. Despite the success of couple mode theory in understanding the thermal radiation from optical resonators, this formalism is not directly consistent with electromagnetic wave theory, and therefore the energy loss rate lacks a

clear definition from fundamental electrodynamics, which particularly imposes a significant difficulty for calculating the energy loss rates in lossy and dispersive media.

In this work, rather than using the phenomenological approach, we develop a general and self-consistent formalism from fluctuational electrodynamics [25] and Quasi-Normal Mode (QNM) theory [118–120] to describe the thermal radiation from optical resonators made by lossy and dispersive materials like metals. For an optical resonator thermal emitter with a predominant resonant mode, our formalism provides a rigorous definition to the *mode loss* (with a closed-form expression) by considering the non-Hermitian nature of the lossy resonant mode and the material dispersion, and shows that to maximize the narrow band thermal radiation from an optical resonator, not only the mode losses to the emitter and the absorber (or far-field background) require to be matched, but the resonant mode needs to be electrically quasi-static, i.e. the electric field of the resonant mode oscillates in phase. This is intrinsically different from coupled-mode theory. By efficiently evaluating the lossy resonant modes of an optical resonator using finite element methods, the new formalism thus paves the way for designing arbitrary optical resonator thermal emitters with perfect or maximized emission.

5.2 Theory

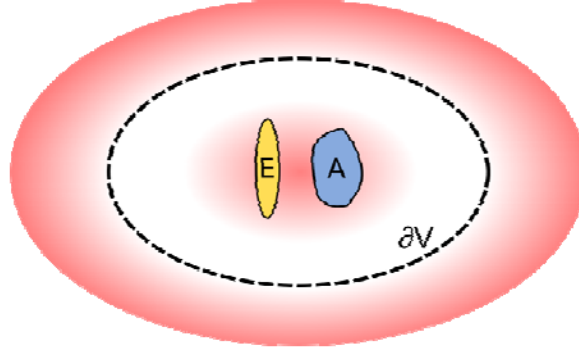


Figure 5-1: The schematic of an optical resonator thermal emitter and a near-field absorber placed in the vacuum background.

We first revisit fluctuational electrodynamics, and then derive the general formulations for both near-field and far-field thermal radiation of arbitrary structures using QNM theory. Consider a thermal emitter V_E at the temperature of T_E and a closely separated object V_A , where V_E and V_A are placed in vacuum, as shown in Figure 5-1. Since the thermal radiation from V_E is physically the emission of electromagnetic waves $[E(r, \omega), H(r, \omega)]$ generated by the thermally induced random currents $j(r, \omega, T_E)$ inside V_E , the spectral thermal energy transfer from V_E to V_A is therefore equal to the averaged electromagnetic absorption power of V_A ,

$$\phi_A(\omega) = \int_{V_A} dr^3 \left\langle \frac{1}{2} \sigma_A E(r, \omega)^* \cdot E(r, \omega) \right\rangle, \quad (5.1)$$

where $*$ denotes the conjugate-transpose, both the field and the current are expressed as 3-by-1 column vectors, and σ indicates the electric conductivity of a material, which relates to its permittivity as $\sigma(\omega) = \omega \text{Im}[\epsilon(\omega)]$. Similarly, the spectral energy transfer from V_E to the far-field, $\phi_\infty(\omega)$, equals the integration of the averaged Poynting vector over an enclosure surface

∂V , which can be further expressed by the total power from the current sources minus the near-field power absorption in both V_E and V_A according to energy conservation [40],

$$\begin{aligned}\phi_\infty(\omega) &= \int_{\partial V} dr^2 \hat{\mathbf{n}} \cdot \left\langle \frac{1}{2} \text{Re} [E \times H^*] \right\rangle \\ &= - \int_{V_E} dr^3 \left\langle \frac{1}{2} \text{Re} [j^* \cdot E] \right\rangle - \int_{V_E} dr^3 \left\langle \frac{1}{2} \sigma_E E^* \cdot E \right\rangle - \int_{V_A} dr^3 \left\langle \frac{1}{2} \sigma_A E^* \cdot E \right\rangle.\end{aligned}\quad (5.2)$$

Note that we ignore the backward thermal radiation from both V_A and the background to V_E . In addition, the spectral energy transfer $\phi(\omega)$ relates to the total power Φ as $\Phi = \int_0^\infty d\omega \phi(\omega)$.

The spectral energy transfer $\phi_A(\omega)$ and $\phi_\infty(\omega)$ in Eqs. (5.1) and (5.2) can be formulated as deterministic expressions, because (i) the electric field emitted by the random currents can be represented by the Dyadic Green's function $G_{\omega,r,r'}$ as $E(r, \omega) = i\omega\mu_0 \int_{V_E} dr'^3 G_{\omega,r,r'} \cdot j(r', \omega, T_E)$, where $G_{\omega,r,r'}$ is a 3-by-3 tensor defined as the impulse response of the wave equation $[\nabla \times \nabla \times + \omega^2 \mu_0 \epsilon(\omega, r)]G_{\omega,r,r'} = \mathbf{I}\delta(r - r')$ and \mathbf{I} is the 3-by-3 unit matrix [24], μ_0 is the vacuum permeability, assuming that there is no magnetic material used in our system; (ii) the autocorrelation of the random currents $j(r, \omega, T_E)$ is characterized by the fluctuation-dissipation theorem [25] as

$$\langle j(r, \omega, T_E) j^*(r', \omega, T_E) \rangle = \frac{4}{\pi} \sigma_E \Theta(\omega, T_E) \delta(r - r') \mathbf{I}.\quad (5.3)$$

Substituting the Dyadic Green's function and Eq. (5.3) into Eq. (5.1), $\phi_A(\omega)$ becomes

$$\phi_A(\omega) = \frac{\Theta}{2\pi} 4\omega^2 \mu_0^2 \text{Tr} \left[\int_{V_A} dr^3 \int_{V_E} dr'^3 \sigma_A \sigma_E G_{\omega,r,r'}^* \cdot G_{\omega,r,r'} \right].\quad (5.4)$$

where $\text{Tr}[\cdot]$ denotes the trace of the matrix, and our derivation uses the property $\text{Tr}[ABC] = \text{Tr}[CAB]$. Similarly, for the first term on the right-hand side of Eq. (5.2), we have $-\int_{V_E} dr^3 \frac{1}{2} \text{Re}[j^* \cdot E] = \frac{\Theta}{2\pi} 4\omega\mu_0 \text{Tr} \left[\int_{V_E} dr^3 \sigma_E \text{Im}[G_{\omega,r,r'}] \right]$. Together with Eq. (5.4), $\phi_\infty(\omega)$ becomes

$$\phi_\infty(\omega) = \frac{\Theta}{2\pi} \left\{ 4\omega\mu_0 \text{Tr} \left[\int_{V_E} dr^3 \sigma_E \text{Im}[G_{\omega,r,r'}] \right] - 4\omega^2 \mu_0^2 \text{Tr} \left[\int_{V_E} dr^3 \int_{V_E} dr'^3 \sigma_E^2 G_{\omega,r,r'}^* \cdot G_{\omega,r,r'} \right] \right. \\ \left. - 4\omega^2 \mu_0^2 \text{Tr} \left[\int_{V_A} dr^3 \int_{V_E} dr'^3 \sigma_A \sigma_E G_{\omega,r,r'}^* \cdot G_{\omega,r,r'} \right] \right\}. \quad (5.5)$$

Eqs. (5.4) and (5.5) are the general expressions for near-field and far-field thermal radiation, respectively. The only assumption is the quasi-thermal equilibrium in V_E , i.e. uniform temperature inside the emitter V_E .

If the thermal emitter in Fig. 1 is simultaneously an optical resonator, its far-field and near-field thermal radiation can be narrow-band and modulated by a predominant resonant mode. In this scenario, we can expand the Dyadic Green's function $G_{\omega,r,r'}$ in terms of the resonant modes based on QNM theory, especially for dispersive and lossy materials. For an optical resonator in vacuum (as shown in Figure 5-1), its resonant modes are naturally defined as the eigen-solutions of the source-free Maxwell equations

$$\begin{aligned} \nabla \times E_n(r) &= i\omega_n \mu_0 H_n(r) \\ \nabla \times H_n(r) &= -i\omega_n \epsilon(\omega_n, r) E_n(r) \end{aligned} \quad (5.6)$$

Here, the electromagnetic fields $[E_n(r), H_n(r)]$ satisfy the outgoing wave boundary condition at $|r| \rightarrow \infty$ [118,119]. In Eq. (5.6), ω_n is the eigen-frequency, which is a complex number in the cases that the resonant mode is lossy. Specifically, $\text{Re}[\omega_n]$ equals the resonant frequency, and

$\text{Im}[\omega_n]$ indicates the mode loss rate. For a good optical resonator thermal emitter, its resonant modes are generally lossy, i.e. $\text{Im}[\omega_n] < 0$, because a thermal emitter must contain dissipative materials in order to intensively radiate thermal energy.

Since the Dyadic Green's function $G_{\omega,r,r'}$ is essentially the impulse response of the Maxwell equations, it can mathematically be expanded in terms of the eigen-solutions of the Maxwell equations, when the resonant modes are orthonormal and complete [121] as

$$G_{\omega,r,r'} = \sum_n \frac{E_n(r) \cdot E_n^*(r')}{\omega \mu_0 (\omega_n - \omega) N_{nm}}, \quad (5.7)$$

where N_{nm} is the orthonormal factor for the mode n to itself. However, it turns out that the orthonormality and completeness of the lossy resonant modes are difficult to be defined and justified. Until recently this difficulty is resolved by QNM theory [118,119]. Since we are only interested in the frequencies in the vicinity of the resonant frequency of a predominated resonant mode, QNM theory proves that the orthonormality and completeness in this condition are approximately held by defining the orthonormal factor N_{nm} [119,122] as

$$N_{nm} = \int_{V_\infty} dr^3 \left[\frac{\partial \omega \epsilon(r, \omega)}{\partial \omega} E_n^T \cdot E_m - \frac{\partial \omega \mu}{\partial \omega} H_n^T \cdot H_m \right] \Bigg|_{\omega=\omega_n}, \quad (5.8)$$

where T denotes the matrix transpose and V_∞ indicates the entire space. The "quasi-" completeness requires that only the field inside or in proximity to the optical resonator can be expanded by the lossy resonant modes [118,119]. Meanwhile, it requires that the lossy resonant modes used in the expansion account for all the important energy decay channels [119]. Note that both of these two requirements are satisfied in our cases, because (i) Eqs. (5.4) and (5.5) only evaluate $G_{\omega,r,r'}$ with $r, r' \in V_E \cup V_A$, therefore the expansion in Eq. (5.7) only involves the

location inside the optical resonator itself and the near-field absorber; (ii) the optical resonator thermal emitters studied in our cases are designed to have a predominant resonant mode. Furthermore, the "quasi-" orthonormality of the lossy resonant modes introduces a nonresonant noise term to the right hand side (RHS) of Eq. (5.7), which is negligible for $\omega \approx \omega_n$. The QNM theory for expanding the field by using the lossy resonant modes has recently attracted massive attentions [46]. Several reports have demonstrated the good accuracy of QNM theory by comparing the directly simulated field profile $[E(r, \omega), H(r, \omega)]$ near the resonant structures emitted by a dipole source with the expansion of its lossy resonant modes, and good agreements are observed [119,123,124]. As a result, QNM theory justifies that Eq. (5.7) with the definition of N_{nn} in Eq. (5.8) is approximately held for the lossy resonant modes expansion near the resonant frequency $\omega \approx \text{Re}[\omega_n]$, which can then be substituted into Eqs. (5.4) and (5.5).

To clarify the effect of an individual resonant mode on thermal radiation, we simplify the physics by assuming the non-degeneracy of the resonant modes, and their resonant frequencies $\text{Re}[\omega_n]$ are highly distinct from each other. Consider the frequencies around the resonant frequency of the predominant resonant mode, i.e. $\omega \approx \text{Re}[\omega_n]$. The near-field radiative energy transfer from V_E to V_A in Eq. (5.4) becomes $\phi_A(\omega) = \frac{\Theta}{2\pi} L(\omega) \psi_A(\omega)$, where $L(\omega) = \text{Re}[\omega_n]^2 / [\text{Re}[\omega_n]^2 + 4Q_n^2(\text{Re}[\omega_n] - \omega)^2]$ is the Lorentz line shape function with the peak at the resonant frequency $\omega = \text{Re}[\omega_n]$, $Q_n = \frac{|\text{Re}[\omega_n]|}{2|\text{Im}[\omega_n]|}$ is the Q-factor of the resonant mode n , and $\psi_A(\omega)$ can be expressed by

$$\psi_A(\omega) = \frac{16}{\text{Im}[\omega_n]^2} \frac{1}{|N_{nn}|^2} \left[\int_{V_A} dr^3 \frac{1}{2} \sigma_A(\omega) |E_n(r)|^2 \right] \left[\int_{V_E} dr^3 \frac{1}{2} \sigma_E(\omega) |E_n(r)|^2 \right]. \quad (5.9)$$

$\phi_A(\omega)$ does not exactly follow the Lorentz line shape when the materials are dispersive. Nevertheless, for the cases that σ_A and σ_E do not abruptly vary at $\omega \approx \text{Re}[\omega_n]$, $\psi_A(\omega) \approx \psi_A(\text{Re}[\omega_n])$ indicates the peak of the near-field energy transfer power density. However, Eq. (5.9) alone fails to describe the dominant mechanism for maximizing the peak value ψ_A and thus guide the emitter design. To clarify the physical meaning of Eq. (5.9), we further express $\text{Im}[\omega_n]$ using the resonant modes $[E_n(r), H_n(r)]$. From Eq. (5.6), it has the mathematical identity $\int_{\partial V} dr^2 [E_n \times H_n^* + E_n^* \times H_n] = -2 \int_V dr^3 (|H_n|^2 \text{Im}[\omega_n] \mu_0 + |E_n|^2 \text{Im}[\omega_n \epsilon(\omega_n)])$, where V is the volume enclosed by ∂V (as shown in Figure 5-1), and $\text{Im}[\omega_n \epsilon(\omega_n)] = \sigma(\text{Re}[\omega_n]) + \text{Im}[\omega_n] \text{Re} \left[\frac{\partial \omega \epsilon}{\partial \omega} \Big|_{\omega=\text{Re}[\omega_n]} \right] + o(\text{Im}[\omega_n]^2)$ based on the Taylor expansion. As a result, $\text{Im}[\omega_n]$ can be expressed as

$$\frac{1}{-\text{Im}[\omega_n]} \approx \frac{\frac{1}{2} \int_V \text{Re} \left(\frac{\partial \omega \epsilon}{\partial \omega} \Big|_{\text{Re}[\omega_n]} |E_n|^2 + \mu_0 |H_n|^2}{\int_{\partial V} \frac{1}{2} \text{Re} [E_n \times H_n^*] + \int_{V_E + V_A} \frac{1}{2} \sigma(\text{Re}[\omega_n]) |E_n|^2}. \quad (5.10)$$

Eq. (5.10) agrees with the conventional definition of the mode loss rate $\tau = -1/\text{Im}[\omega_n]$, which equals the energy stored in the resonator divided by the energy loss per cycle [40]. In addition, the numerator on the RHS of Eq. (5.10) agrees with the universal description of the energy density, especially in the dispersive materials like metal [125]. Substitute Eq. (5.10) into Eq. (5.9), the peak value of the near-field spectral energy transfer from V_E to V_A equals

$$\Psi_A = 4 \left(\frac{D_E}{D_E + D_A + D_\infty} F \right) \left(\frac{D_A}{D_E + D_A + D_\infty} F \right), \quad (5.11)$$

where $D_E = \int_{V_E} dr^3 \frac{1}{2} \sigma_E (\text{Re}[\omega_n]) |E_n(r)|^2$ and $D_A = \int_{V_A} dr^3 \frac{1}{2} \sigma_A (\text{Re}[\omega_n]) |E_n(r)|^2$ represent the mode energy losses due to the resistive dissipation in the emitter and the absorber, respectively. $D_\infty = \int_{\partial V} dr^2 \frac{1}{2} \text{Re}[E_n(r) \times H_n^*(r)]$ has the form of the mode energy loss due to far-field radiation. F is a factor attributed to the non-Hermitian imperfection of the lossy resonant mode expansion, which equals $F = \left| \int_V dr^3 \text{Re} \left[\frac{\partial \omega \epsilon}{\partial \omega} (\text{Re}[\omega_n]) \right] |E_n|^2 + \mu_0 |H_n|^2 \right| / |N_{nn}|$.

Next, we investigate the far-field thermal radiation of V_E in Eq. (5.5) with the substitution of Eqs. (5.7) and (5.8). For the frequency ω close to the resonant frequency $\text{Re}[\omega]$ of the mode, the first term on the RHS of Eq. (5.5) becomes

$$4\omega\mu_0 \text{Tr} \left[\int_{V_E} dr^3 \sigma_E \text{Im} [G_{\omega, r, r}] \right] \approx 4 \text{Im} \left[\frac{1}{(\omega_n - \omega)} \right] \text{Re} \left[\frac{\int_{V_E} dr^3 \sigma_E(\omega) E_n^T(r) E_n(r)}{N_{nn}} \right], \quad (5.12)$$

$$= L(\omega) \psi_1(\omega)$$

where the peak value $\Psi_1 = \psi_1(\text{Re}[\omega_n]) = 4 \left(\frac{D_E}{D_E + D_A + D_\infty} F \right) P$, and the factor P is defined as

$$P = \text{Re} \left[\frac{\int_{V_E} dr^3 \sigma_E E_n^T(r) E_n(r)}{N_{nn}} \right] / \frac{\int_{V_E} dr^3 \sigma_E |E_n(r)|^2}{|N_{nn}|}, \quad (5.13)$$

which is the other imperfection factor due to the non-Hermitian fact as compared to the factor F . Mathematically, it has $P \leq 1$. Since the second and the third terms in Eq. (5.5) have the same form with Eq. (5.4), the spectral thermal radiation of V_E to far-field can be derived from Eqs.

(5.11) and (5.12) as $\phi_\infty(\omega) = \frac{\omega}{2\pi} L(\omega) \psi_\infty(\omega)$, where the peak value $\Psi_\infty = \psi_\infty(\text{Re}[\omega_n])$ equals

$$\Psi_\infty = 4 \left(\frac{D_E}{D_E + D_A + D_\infty} F \right) \left(P - \frac{D_E + D_A}{D_E + D_A + D_\infty} F \right). \quad (5.14)$$

Hence, Eqs. (5.11) and (5.14) represent a new physical framework to understand and control the thermal radiation from optical resonators in both near- and far-fields. To interpret the weights of the mode energy losses into all possible sources, we define the *fractional mode loss* of the emitter, the near-field absorber, and the far-field as $\eta_E = \frac{D_E}{D_E+D_A+D_\infty} F$, $\eta_A = \frac{D_A}{D_E+D_A+D_\infty} F$ and $\eta_\infty = P - \eta_E - \eta_A$, respectively. Although the values of D_∞ and F depend on the choices of the enclosure surface ∂V and the volume V , η_E , η_A and η_∞ all have fixed values because $\frac{F}{D_E+D_A+D_\infty} = \left| \frac{4}{\text{Im}[\omega_n] N_{nn}} \right|$ according to Eq. (5.10). As a result, Eqs. (5.11) and (5.14) become

$$\begin{aligned}\Psi_A &= 4\eta_E\eta_A \\ \Psi_\infty &= 4\eta_E\eta_\infty\end{aligned}\tag{5.15}$$

Given that both Ψ_A and Ψ_∞ are positive, and $\eta_E + \eta_A + \eta_\infty = P$, the maxima of both Ψ_A and Ψ_∞ are equal to P^2 , when $\eta_E = \eta_A = \frac{P}{2}$ and $\eta_\infty = 0$ for near-field thermal radiation, and $\eta_E = \eta_\infty = \frac{P}{2}$, $\eta_A = 0$ for far-field thermal radiation.

Because of the modulation of a resonant mode, both near-field and far-field spectral thermal energy fluxes follow the Lorentz line shape. To maximize thermal emission, Eqs. (5.11) and (5.14) demonstrate that the fractional mode losses must be matched in order to achieve maximized thermal radiation, i.e. $\eta_E = \eta_A = \frac{P}{2}$ for near-field emission, and $\eta_E = \eta_\infty = \frac{P}{2}$ for far-field emission. In our theory, the peak or maximum value of both near-field and far-field spectral thermal emission equals $\frac{\Theta}{2\pi} P^2$, which is the key distinction from the coupled-mode theory, i.e. peak equals $\frac{\Theta}{2\pi}$ [116,117]. To maximize P for reaching the limit of the peak value, Eq. (5.13) suggests that optical resonator thermal emitters need to be designed to have electrical quasi-static resonant modes, i.e. the electric field oscillates in phase, or $E_n(\mathbf{r})$ near the optical resonator has a

real value and it can be expressed by a voltage potential as $E_n = -\nabla\Phi$ [24]. In this case, $P \approx 1$ because (i) by choosing V to only enclose the near-field components of the resonant mode, the portion of the resonant mode outside V behaves as the propagating waves and therefore $\left(\frac{\partial\omega\epsilon}{\partial\omega}\right)E_n^2 = \epsilon E_n^2 \approx \mu H_n^2$, which results in $N_{nn} \approx \int_V dr^3 \left(\frac{\partial\omega\epsilon}{\partial\omega}\right)E_n^2 - \mu H_n^2$; (ii) the portion of the resonant mode inside V behaves to be quasi-static, where $H_n = \frac{1}{i\omega\mu_0}\nabla \times E_n \approx 0$, and thus $N_{nn} \approx \int_V dr^3 \left(\frac{\partial\omega\epsilon}{\partial\omega}\right)E_n^2$; (iii) Since the quasi-static electric field has a real value, $\int_{V_E} \sigma_E E^2 \approx \int_{V_E} \sigma_E |E|^2$ and $N_{nn} \approx \int_V dr^3 \left(\frac{\partial\omega\epsilon}{\partial\omega}\right)|E_n^2| \approx |N_{nn}|$ based on the fact $\frac{\partial\omega\epsilon}{\partial\omega} > 0$. Likewise, $F \approx \left| \frac{\int_V dr^3 \text{Re}\left[\frac{\partial\omega\epsilon}{\partial\omega}\right]|E_n|^2}{\int_V dr^3 \left(\frac{\partial\omega\epsilon}{\partial\omega}\right)E_n^2} \right| \approx 1$. As a result, in the quasi-static condition, our formalism agrees with the coupled mode theory: the requirement of matching fractional mode losses reduces to the matching of the mode energy losses $D_E = D_A$ for the near-field case and $D_E = D_\infty$ for the far-field case, and the peak value of the spectral thermal emission is equal to the limit of $\frac{\Theta}{2\pi}$.

5.3 Numerical Validation

Based on our formalism, we revisit the thermal emission of metal nanorods in both far-field and near-field, and demonstrate that metal nanorods can be designed as perfect optical resonator thermal emitters in both far- and near-fields by tuning the diameter of nanorods. We also validate our formalism by comparing $\phi_A(\omega)$ and $\phi_\infty(\omega)$ obtained from Eq. (5.11) and (5.14) with the direct simulation results from the Fluctuating-Surface Current (FSC) method [37,39]. In addition, to directly evaluate the fractional mode losses in Eq. (5.11) and (5.14), we numerically simulate

the lossy resonant modes and the normalization factor N_{nn} in Eq. (5.8) by using the finite element method and the postprocessing technique proposed in Ref. [123].

We investigate the far-field thermal radiation of a single gold nanorods and the near-field thermal energy transfer between two closely separated gold nanorods, where the nanorods have the same length of $L = 2.5\mu\text{m}$ but different diameter D . For the near-field case, two nanorods separate a distance of 50nm. The fundamental resonant mode of both cases are plotted in Fig. 2(a) and (b) for the single nanorod, and Fig. 3(a) and (b) for the two nanorods. The field profiles indicate that the resonant modes in both cases are essentially the Fabry-Perot resonance of the TM_0 waveguiding mode. Fig. 2(c) and Fig. 3(c) plots the fractional mode losses of the cases with different D . For the single nanorod case, η_E matches η_∞ at a single point of $D \sim 40\text{nm}$, where $\eta_E = \eta_\infty \sim 0.5$ indicating that the far-field thermal radiation is maximized. For the two nanorod case, $\eta_E = \eta_A \rightarrow 0.5$ for $D < 100\text{nm}$, where $\eta_E = \eta_A$ is because the emitter and the absorber are exactly the same, and $\eta_E = \eta_A \rightarrow 0.5$ for $D \rightarrow 0$ is attributed to the fact that the resistive losses of TM_0 waveguiding mode is monotonically increasing as the decrease of D , and therefore $\eta_E + \eta_A \rightarrow 1$. We also evaluate the factor P for all these cases, and $P \approx 1$ indicating the resonant modes satisfy the quasistatic criteria, which make the metal nanorods good candidates for making perfect optical resonator thermal emitters. Furthermore, both the spectral energy fluxes and their peak values obtained from our formalism are compared with the direct simulation results by the FSC method, as shown in Fig. 2(d) and the black curves in Fig. 2(c). The good agreement convincingly verifies our formalism in both far-field thermal emission and near-field energy transfer cases.

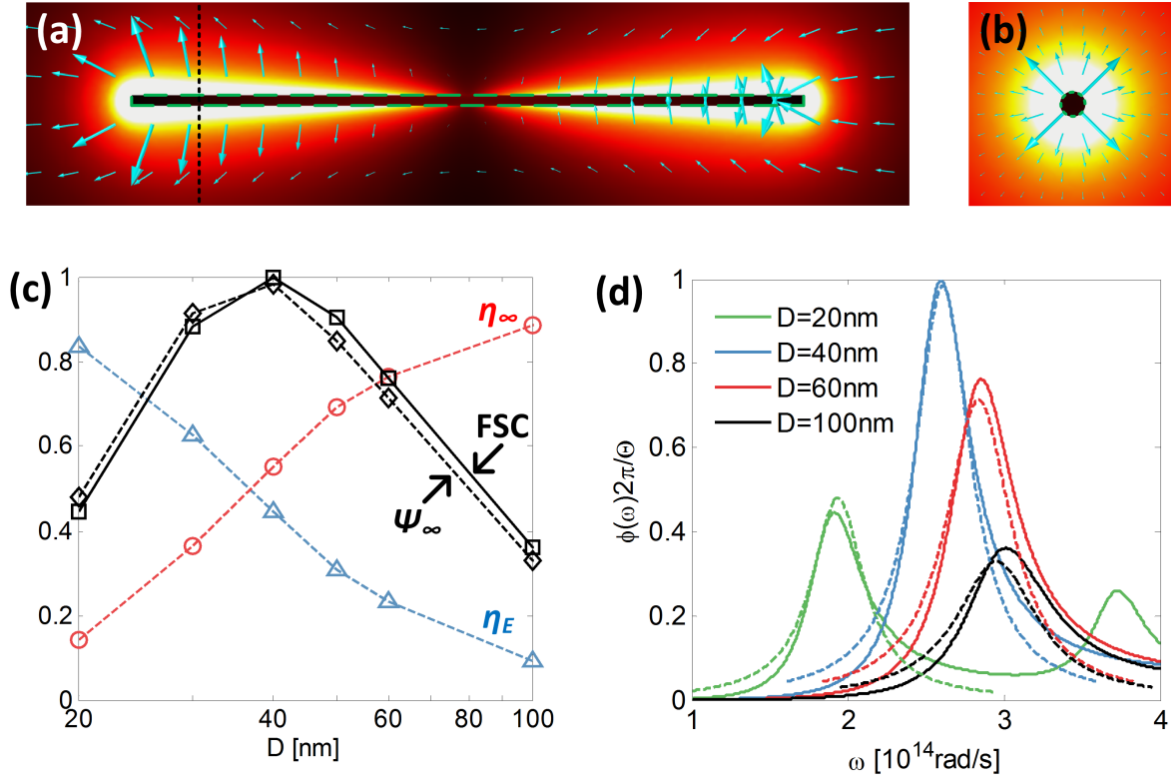


Figure 5-2: (a) and (b) Electric field profile of the fundamental resonant mode of the gold nanorod with $D = 40\text{nm}$ and $L = 2.5\mu\text{m}$. Color profile and the arrows indicate the field intensity and polarization, respectively. (c) Fractional mode losses and the thermal emission peak value for the cases with different D . (d) Spectral energy flux of thermal emission evaluated based on theory (dash curves) and direct calculation (solid curves).

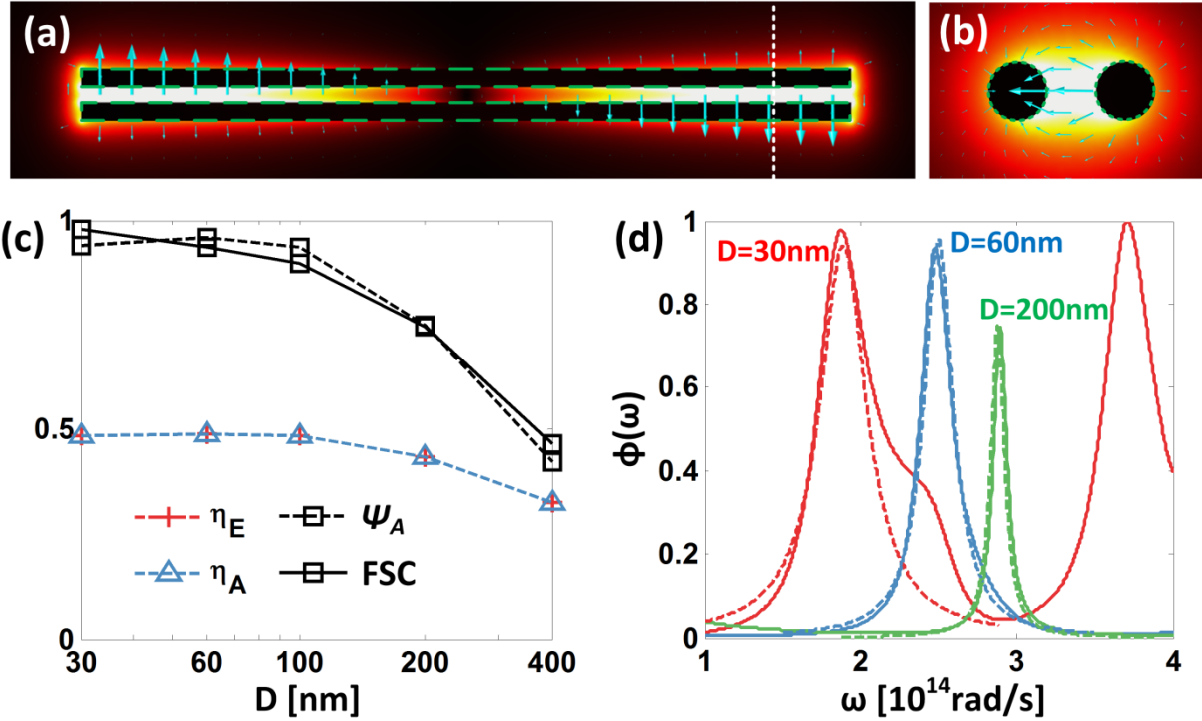


Figure 5-3: (a) and (b) Electric field profile of the fundamental resonant mode of two aligned gold nanorods with $D = 60\text{nm}$, $L = 2.5\mu\text{m}$ and a 50nm gap. Color profile and the arrows indicate the field intensity and polarization, respectively. (c) Fractional mode losses and the thermal emission peak value for the cases with different D . (d) Spectral energy flux of thermal emission evaluated based on theory (dash curves) and direct calculation (solid curves).

5.4 Conclusion

In conclusion, we develop a general formalism from the fluctuational electrodynamics and quasi-normal mode theory to elucidate the underlying physics of the far-field and near-field thermal radiation from the optical resonators made by lossy and dispersive material. Because of the modulation from the resonant mode, the thermal emission power density spectrum of the optical resonators is narrow-band and follows the Lorentz line shape with the peak at the

resonant frequency of the mode. To maximize the thermal emission, our formalism demonstrates that not only the mode losses to the emitter and the absorber (or far-field background) require to be matched, but the resonant mode also needs to be electrically quasi-static, i.e. the electric field of the resonant mode oscillates in phase. In addition, we also validate our formalism by investigating the far-field and near-field thermal emission from metal nanorods. Our formalism can therefore serve as a general rule to design the narrow-band thermal emission of arbitrary resonant structures.

6 Perfect Narrow-band Thermal Emission by Transmission Line Resonators

6.1 Introduction

Although thermal radiation usually have a fairly broad spectrum, the narrow-band control of thermal emission is of great importance in a variety of applications such as infrared sensing [110], thermophotovoltaics [20,111], radiation cooling [112] and thermal circuits [37,79]. One popular method to achieve narrow-band thermal emission is to tailor the spectral properties of resonant nanophotonic structures like metamaterials, nanocavities, and so on. The corresponding peak frequencies of thermal radiation can be readily tuned by modifying the geometries of the nanophotonic structures. However, a critical challenge for designing the nanophotonic resonators is the further maximization of the narrow-band thermal emission towards the "perfect" emission, where the emissive power reaches the blackbody radiation limit in the far-field. For instance, impedance matching has been widely used to maximize the thermal emission from metamaterials. But there lacks a general principle to design the impedance matching, where the electric and magnetic responses of the meta-atoms are generally correlated to each other in a complicated manner [126].

In this work, rather than using the well-known metamaterial framework, we introduce a new type of perfect resonant thermal emitters made from the densely packed transmission line resonators. Transmission lines are essentially the waveguides composed of one or multiple metallic wires, which have been invented more than a century ago [127] and extensively used in radio-frequency communications. It has been discovered that microscale transmission lines could efficiently guide the terahertz and infrared waves with highly confined waveguiding modes [93,128,129]. In terms of the recently developed Quasi-Normal Mode theory, we experimentally demonstrate that the thermal emission from a transmission line resonator can

always be maximized by tuning the waveguide loss or bending the structure. It therefore serves as a general principle to design perfect thermal emitters by densely packing the resonators on a surface. The perfect narrow-band thermal emitters based on transmission line resonators are particularly promising for narrow-band infrared sources, because the infrared transmission line structures can be fabricated by using large-scale techniques such as nano-imprinting [130], chemical synthesis [131], etc., and their emission can be easily tuned to cover the entire infrared spectrum by changing their geometries.

6.2 Maximizing Thermal Emission of Transmission Line Resonators

The thermal emission from an optical resonator has a narrow-band spectrum because of the modulation by its resonant mode. According to the recently developed Quasi-Normal Mode theory, its thermal emission spectrum follows a Lorentz line-shape, where the peak $\psi = \phi(\omega_0)$ equals

$$\psi = \frac{\Theta(\omega_0, T)}{2\pi} 4\eta_E\eta_\infty. \quad (6.1)$$

In Eq. (6.1), ω_0 is the resonant frequency, $\Theta(\omega, T) = \hbar\omega / \left[\exp\left(\frac{\hbar\omega}{k_B T}\right) - 1 \right]$ is the Planck distribution, η_E and η_∞ are the dissipative and radiative fractional mode losses, respectively. For the optical resonators whose resonant modes have quasi-static electric field profile, η_E and η_∞ satisfies $\eta_E + \eta_\infty \approx 1$, which can be understood as the percentages of the mode energy losses inside the resonator and to the far-field, respectively. As a result, the upper limit of ψ equals $\frac{\Theta}{2\pi}$ when $\eta_E = \eta_\infty = 0.5$. Although a single resonator only emits a limited amount of energy, the total energy flux from a surface with densely packed resonator arrays can potentially reaches the

blackbody radiation limit, i.e. $\frac{\psi}{A} \rightarrow \frac{\Theta(\omega, T)}{2\pi} \left(\frac{2\pi}{\lambda^2} \right)$, where A is the occupation area of a single resonator, and $\lambda = 2\pi\omega/c_0$ is the free-space wavelength.

To make a perfect thermal emitter, however, the resonators cannot be packed infinitely dense. This is because each resonator has a geometrical area A_g and thus $A > A_g$ must be satisfied. The distance between the adjacent resonators also requires to be large in order to prevent the strong interaction between the adjacent resonant modes. Otherwise, ψ can be severely deteriorated due to the significant increase of the dissipative mode loss η_E to the near-field neighbors. As a result, maximizing the emission from each optical resonator is crucial for achieving the perfect thermal emission.

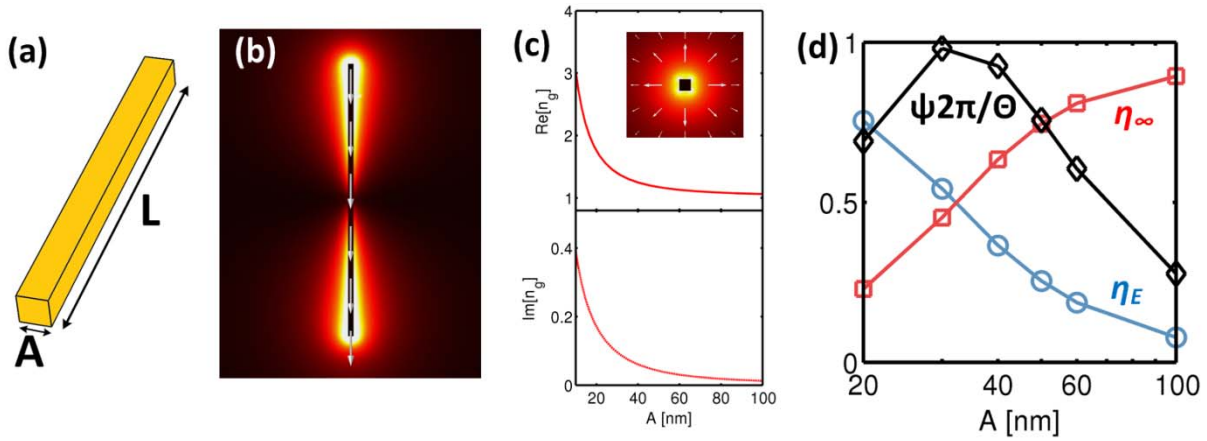


Figure 6-1: (a) The schematic of the transmission line resonator. (b) The electric field profile of the fundamental resonant mode. Arrows indicate the electric field polarization directions. (c) The effective propagating index of the transmission line waveguiding mode at the wavelength of $7\mu\text{m}$, inset: the electric field profile of the waveguiding mode. (d) The fractional mode losses η_E and η_∞ , and the thermal emission peak ψ of the cases with different A .

Transmission line resonators, i.e. cropped transmission lines with finite length, provide us a universal platform to realize perfect thermal emitters. Here, we introduce general principles to respectively tune the dissipative and radiative mode losses, i.e. η_E and η_∞ in Eq. (6.1), of a transmission line resonator by investigating its resonant modes using the quasi-normal mode formulation. Consider a gold wire transmission line resonator with the length $L = 2.5\mu\text{m}$ and the lateral size $A = 40\text{nm}$ as shown in Figure 6-1(a). The electric field profile of its fundamental resonant mode is plotted in Figure 6-1(b), where the fundamental resonant mode $[E_0(r), H_0(r)]$ is defined as the eigen-solution of the source-free Maxwell equations with the smallest eigen-frequency ω_0 [118,119]

$$\begin{aligned}\nabla \times E_0(r) &= i\omega_0\mu_0 H_0(r) \\ \nabla \times H_0(r) &= -i\omega_0\epsilon(\omega, r)E_0(r),\end{aligned}\tag{6.2}$$

where $[E_0(r), H_0(r)]$ can be directly calculated by using the finite-element method [123] based on quasi-normal mode formulation. Figure 6-1(b) clearly shows that the resonant modes of the transmission line resonator is essentially the Fabry-Perot resonance of the waves traveling in the form of the waveguiding mode, where the resonant wavelength equals $\lambda_0 = 7\mu\text{m} \approx 2L \times \text{Re}[n_g]$ and n_g is the propagating index of the waveguide. It clearly indicates that the dissipative mode loss η_E is directly proportional to the loss of the waveguide, which can be increased by shrinking the transverse size A of the metal wire [129]. We simulate the propagating index n_g of the gold nanowire transmission lines with different A . From Figure 6-1(c), the waveguide loss characterized by $\text{Im}[n_g]$ monotonically increases as the decrease of A . Next, we adopt the Quasi-Normal Mode theory to evaluate the fractional mode losses η_E and η_∞ and the thermal emission peak value ψ of the transmission line resonators at the same $L = 2.5\mu\text{m}$ with different A . As

shown in Figure 6-1(d), η_E is monotonically increasing as the decrease of A , which agrees with the trend of the waveguide loss in Figure 6-1(c). At $A \sim 40\text{nm}$, the dissipative mode loss and the radiative mode loss are matched, i.e. $\eta_E = \eta_\infty = 0.5$, and the peak of the thermal emission spectrum reaches the maximum $\psi \rightarrow 1$. As a result, it can be concluded that modifying the transverse size of transmission line serves as a general principle to tune the dissipative mode losses η_E of the transmission line resonators.

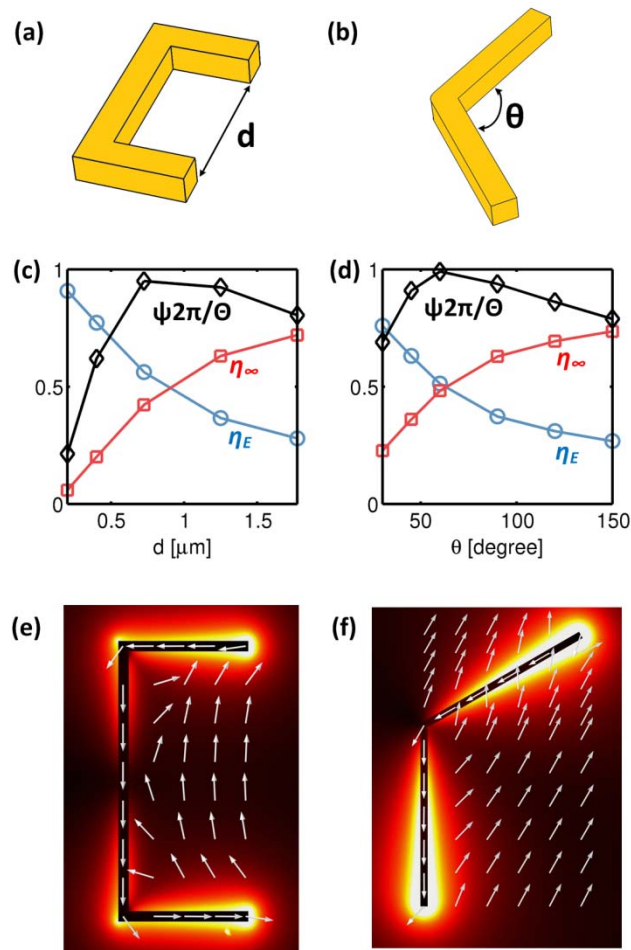


Figure 6-2: (a) and (b) The schematic of the bended transmission line resonators in C-shape (a) and (b) V-shape. (c) and (d) The fractional mode losses η_E and η_∞ , and the thermal emission

peak ψ of the cases with different d and θ . (e) and (f) the electric field profile of the fundamental resonant modes for both the cases. Arrows indicate the electric field polarization directions.

To tune the radiative mode loss η_∞ , we consider two types of bended transmission line resonators: C-shape and V-shape, as shown in Figure 6-2(a) and (b) respectively. In both cases, the length and the cross-section of the transmission line is kept to be the same, i.e. $L = 2.5\mu\text{m}$ and $A = 50\text{nm}$. Figure 6-2(c) and (d) plot the fractional mode losses η_E and η_∞ and the peak height ψ for the C-shape cases with different gap distance d and the V-shape cases with different bending angle θ . It can be found that η_∞ in both cases monotonically decreases as d for the C-shape resonator and θ for the V-shape resonator are shrunk. At the certain values of d and θ , η_∞ matches with η_E , and the thermal emission peak ψ reaches the maximum. To reveal the mechanism of tuning the radiative mode loss by bending the transmission line resonator, we rearrange Eq. (6.2) as

$$\begin{aligned}\nabla \times E_0(r) &= i\omega_0\mu_0 H_0(r) \\ \nabla \times H_0(r) &= -i\omega_0\epsilon_0 E_0(r) - i\omega_0 P(r).\end{aligned}\tag{6.3}$$

where $P(r) = (\epsilon(\omega_0, r) - \epsilon_0)E_0(r)$ indicates the induced electric dipole moments inside the emitter. Because the fundamental resonant mode confines the fields in subwavelength scale, it has $E_0 = \omega_0^2\mu_0 \int_{V_E} dr'^3 G_{\omega, r, r'} \cdot P(r') \approx \omega_0^2\mu_0 G_{\omega, r, r_0} \int_{V_E} dr'^3 P(r')$. Therefore, $[E_0, H_0]$ can be interpreted as the field emitted by an equivalent dipole located at the r_0 in free-space with the dipole moment $\int_{V_E} dr^3 P(r)$. Since η_∞ is proportional to $\int_{\partial V} \frac{1}{2} \text{Re}[E_0 \times H_0^*]$, i.e. the total outward energy flux from an enclosure surface ∂V . it therefore has $\eta_\infty \propto \left| \int_{V_E} dr^3 P(r) \right|^2$ according to the

property of dipole radiation [40]. As a result, by bending the transmission line resonator without changing the resonant mode, the radiative mode loss η_∞ can be tuned because it introduces a directional vector $\hat{\mathbf{e}}(r)$ in the integral $\eta_\infty \propto \left| \int_{V_E} dr^3 \hat{\mathbf{e}}(r) \cdot P(r) \right|^2$. For both the C-shape and V-shape transmission line resonators, the electric fields inside the metal wires are all polarized along the wire, as shown in Figure 6-2(e) and (f). Therefore, bending can efficiently reduce the overall equivalent dipole moment $\int_{V_E} dr^3 P(r)$ in both the cases, and the η_∞ can be decreased accordingly.

6.3 Experimental Validation

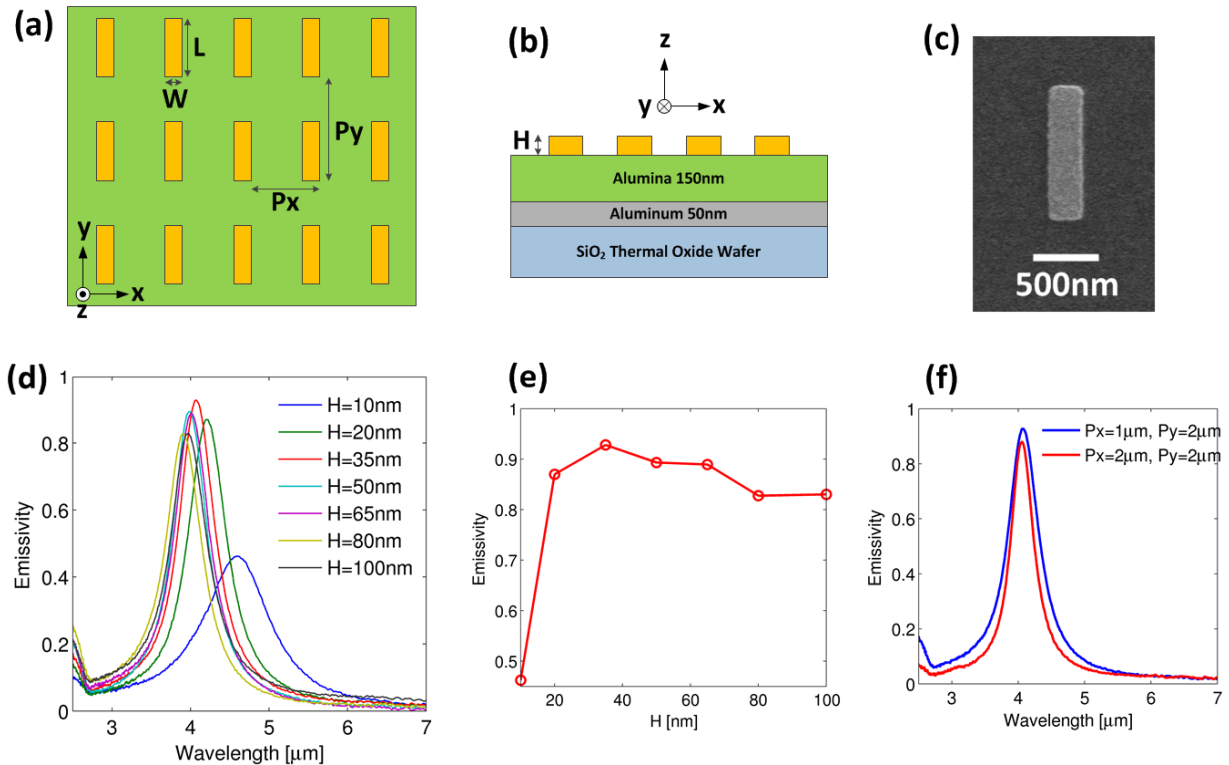


Figure 6-3: (a) and (b) The schematic of the transmission line resonator arrays. (c) The SEM image of an individual transmission line resonator in the arrays. (d) The y-polarized emissivity

spectrums of arrays with different H and (e) their corresponding peak values. (f) The y-polarized emissivity spectrums of the resonator arrays at $H = 35\text{nm}$ with different periodicity.

Based on the aforementioned principles, we experimentally investigate the thermal emissivity of the densely packed transmission line resonator arrays, as shown in Figure 6-3(a) and (b). Because the thermal emission from each resonator is usually omnidirectional, the substrate is chosen as a metal plate with a dielectric spacer, where the metal plate serves as a mirror to reflect all the radiation to the upper space. We demonstrate that the perfect thermal emission of the resonator arrays can always be approached by either tuning the thickness H of the metal wires or bending the individual structure, as shown in Figure 6-1 and Figure 6-2. To prove the concept, all of the transmission line resonators are aligned in y-direction, which is expected to achieve the perfect emissivity at the y-polarization. The sample fabrication begins with the sputtering of a 50nm thick aluminum thin film as the metal ground plate on a SiO_2 thermal oxide wafer. Then a 150nm thick aluminum oxide layer is sputtered on top of the aluminum, which serves as the dielectric spacer. Next, the transmission line resonator arrays are fabricated by electron beam lithography technique, which involves the following steps: (i) a 200nm-thick PMMA A4 photoresist layer is spin coated on top of the wafer, and then baked 2 minus at 180 degree Celsius; (ii) the metal wire arrays are patterned with the electron beam lithography (FEI Sirion 400 with JC Nability Nanometer Pattern Generation System), followed by the sample developing in the methyl isobutyl ketone (MIBK) solution (MIBK:IPA=1:3) with 90 seconds strong agitation; (iii) a gold thin film with the desired thickness H is then deposited with the electron beam evaporation deposition process (Ultek E-Beam Evaporator), followed by the lift-off of the photoresist. The Scanning Electron Microscope (SEM) image of a single

transmission line resonator is shown in Figure 6-3(c). The total lateral size of the arrays is $80\mu\text{m} \times 80\mu\text{m}$.

The thermal emissivity spectrums of the samples are characterized in the wavelength range of $2 - 12\mu\text{m}$. The emissivity is evaluated as the absorptivity according to the Kirchhoff's law, which is applicable since the size of the arrays is larger than the characteristic wavelength of thermal radiation. Since our samples are opaque, we directly measured their reflectivity. The emissivity can then be evaluated as one minus the reflectivity. To obtain the reflectivity, the y-polarized reflection spectrums of the samples are firstly measured by using a Fourier-Transform Infrared Spectrometer (Bruker IFS 66/s) combined with an infrared microscope (Bruker Hyperion 3000, with liquid nitrogen cooled MCT detector, KBr beam splitter, 15x cassegrain objective lens with numerical aperture of 0.4). Specifically, the reflected light in $7 - 23$ degrees to the normal direction is collected from a $40\mu\text{m} \times 40\mu\text{m}$ focusing spot on the samples. An infrared linear polarizer is used in the infrared microscope, which only allows the y-polarized reflected light passing through to the detector. Then, the reflection spectrums of the samples are normalized to that of a gold standard mirror, and the reflectivity and emissivity can thus be obtained.

We first demonstrate that the transmission line resonator arrays can achieve the perfect narrow-band thermal emission by tuning the metal wire thickness H . Figure 6-3(d) plots the measured emissivity spectrums of the resonator arrays with at $L \sim 1\mu\text{m}$ and $W \sim 0.25\mu\text{m}$ with different H . The period of the arrays is chosen as $P_x = 1\mu\text{m}$ and $P_y = 2\mu\text{m}$ to satisfy $A = P_x P_y < \lambda^2/\pi$ in order to be capable to reach the blackbody limit at the peak of $\lambda \sim 4\mu\text{m}$, and meanwhile preventing the strong interactions between the adjacent resonators. The narrow-band

thermal emission is observed for all the cases, where the peak wavelength corresponds to the resonance wavelength of the fundamental Fabry-Perot type mode, i.e. $\lambda_0 \sim 2Ln_g$. We also plot the corresponding peak values in Figure 6-3(e). By reducing H , the emissivity peak is first increasing and then decreases. At the optimized thickness $H = 35\text{nm}$, the emissivity peak reaches maximum. The discrepancy between the maximum peak value and the blackbody limit (100% emissivity) is attributed to (i) the limited resolution of our data points; (ii) the non-perfect angular dependent emission in oblique directions, where the upper bound of the averaged emissivity in $7 - 23$ degrees is estimated as 97% by assuming each transmission line resonator has the dipole radiation pattern. Note that the trend of the emissivity-peak variation in Figure 6-3(e) totally agrees with the theoretical investigation in Figure 6-1(c). We further prove that this narrow-band emissivity is not due to the strong interactions between the adjacent resonators (e.g. the optical grating effect), by comparing the emissivity spectrums of the resonator arrays at $H = 35\text{nm}$ with different period P_x and P_y in Figure 6-3(f). Their line-shapes agree well with each other, indicating no interaction between adjacent resonators.

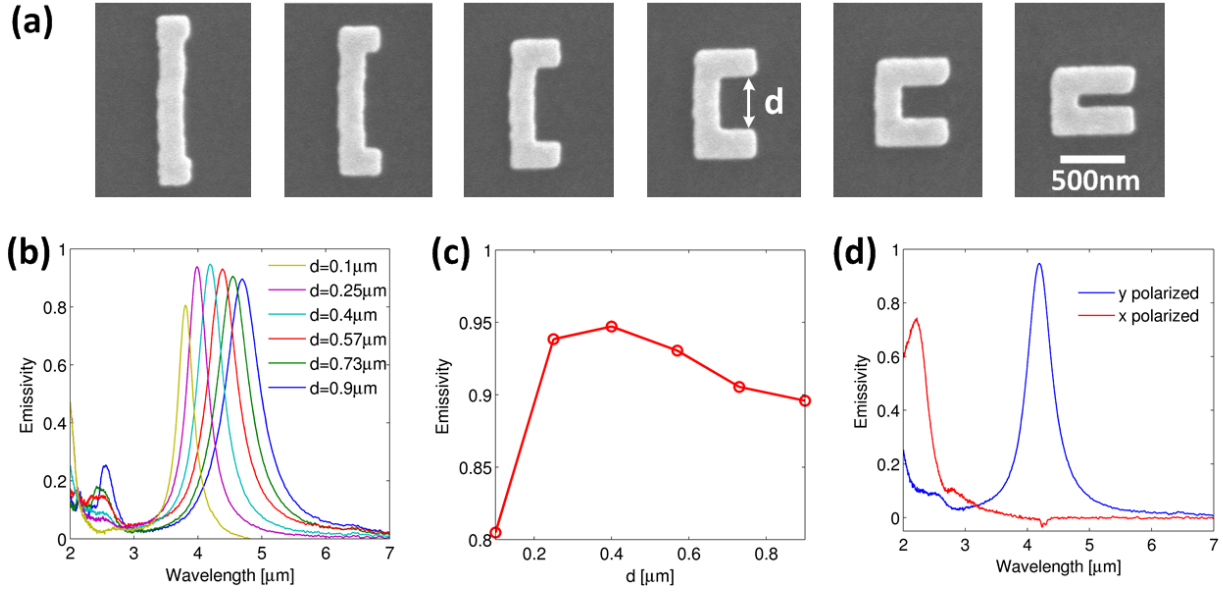


Figure 6-4: (a) The SEM images of the C-shape transmission line resonators with different gap distance d . (b) The y-polarized emissivity spectrums of the C-shape resonator arrays with different d , and (c) the corresponding peak values. (d) The y-polarized and x-polarized emissivity spectrums of the C-shape arrays with $d = 400\text{nm}$.

Next, we demonstrate that the thermal emission of the transmission line resonator arrays can also be maximized by bending the individual resonator. Here, we investigate both the C-shape and the V-shape structures. For the arrays of the C-shape with different gap distance d , the SEM images of the bended individual resonators are shown in Figure 6-4(a). As a fair comparison, the total length, width and thickness of the C-shape resonators are kept the same as $L \sim 1.4\mu\text{m}$, $W \sim 200\text{nm}$ and $H = 80\text{nm}$. The y-polarized emissivity spectrums of the arrays with different d is plotted in Figure 6-4(b), and the corresponding peak values are plotted in Figure 6-4(c). The peak wavelength also agrees with the resonant wavelength of the fundamental FP-type mode, and the similar trend of the peak height variation is observed in comparison with our

previous theoretical investigation. At $d = 400\text{nm}$, the emissivity peak approaches the blackbody limit. For this optimal structure, we also measure its emissivity spectrums with different polarization, as shown in Figure 6-4(d). The x-polarized emissivity is approximately zero at the resonant wavelength, which can be well explained by the aforementioned mechanism of radiative mode loss. Since the overall dipole moment of the C-shape transmission line resonator is polarized along y-direction, the emission only has the y-polarized electric field. We also investigate the arrays of the V-shape resonators with different bending angle θ , where the SEM images of the individual V-shape structures are shown in Figure 6-5(a). The length and the width of the V-shape transmission line are kept the same as $L \sim 1\mu\text{m}$, $W = 0.13\mu\text{m}$. The thermal emissivity spectrums and the corresponding peak height at different θ are plotted in Figure 6-5(b) and (c), respectively. The peak can also be maximized, and the similar trend of the peak height variation is also observed in comparison with the theoretical investigation. Hence, bending the transmission line structures (therefore changing the dipole moment) serves as a general method to maximize the thermal emissivity of the resonator arrays by tuning the radiative mode loss of the individual resonator.

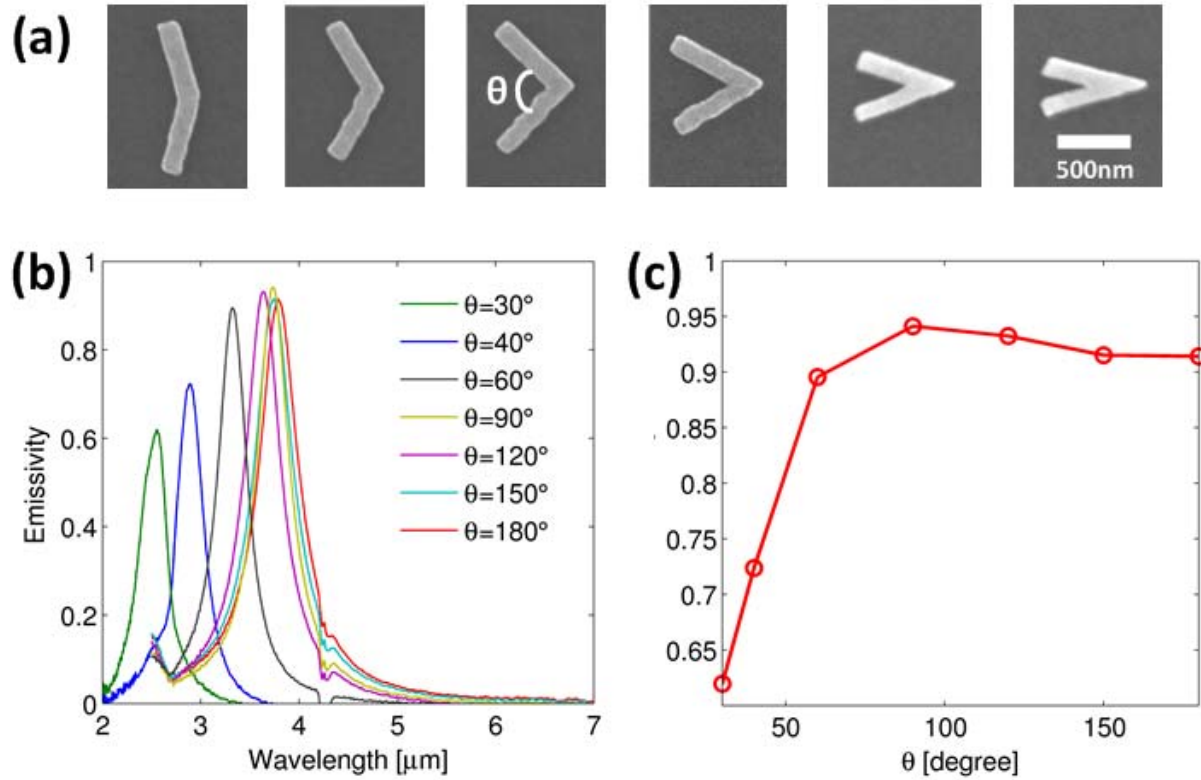


Figure 6-5: (a) The SEM images of the V-shape transmission line resonators with different bending angle θ . (b) The y-polarized emissivity spectrums of the V-shape resonator arrays with different θ , and (c) the corresponding peak values.

6.4 Conclusion

In conclusion, we propose a general formalism to make the perfect thermal emitter by densely packing the transmission line resonators on a surface. Rather than using the widely used metamaterial formalism, we adopt the recently developed Quasi-Normal Mode theory, and demonstrate a general principle to maximize the thermal emission by tuning the resistive mode loss and radiative mode loss of the individual transmission line resonator. Finally, we experimental validate our formalism by directly measuring the thermal emissivity of the

transmission line resonator arrays with different thickness or bending into different shapes. Our formalism therefore broadens the horizon of the fields of thermal light sources, thermal energy management and infrared sensing and imaging.

7 Conclusions and Outlook

7.1 Conclusions

In this dissertation, we designed and manipulated the super-Planckian thermal radiation by using the nanophotonic techniques. Our contributions are summarized as follows.

We described a hyperbolic metamaterial based heat emitter/absorber made of metal wire arrays (MWAs), which can greatly enhance near-field heat transfer with infrared surface plasmon resonant (IR-SPR) materials. Rather than match the resonant frequencies of IR-SPR materials, MWAs are non-resonant and have enormous enhancement of the local density of states (LDOS) in a broad frequency range. We directly simulated the near-field radiative heat transfer between MWAs and an IR-SPR emitter based on the Wiener-chaos expansion method. The direct numerical simulation is demonstrated to be critical for accurately predicting the near-field radiation of complex geometries like metamaterials. Manipulation of near-field radiation using metamaterials has been considered in theory for a long time but is difficult to be experimentally realized. The results presented in this paper provide a feasible way to achieve such metamaterials which work in the near-field and enhance radiative heat transfer beyond material limitation.

We demonstrated that the thermal excitation of graphene surface plasmons (GSPs) provides unprecedented opportunities for both thermal science and nanophotonics. Our numerical calculations demonstrate that thermal energy can be efficiently converted into the monochromatic and tunable propagating GSPs. Therefore, the plasmonics theory/methods can be applied to manipulate the thermal energy (e.g. GSP waveguide, GSP modulator, GSP detector, etc.). Graphene nanoemitters can be designed to have specific output spectra as guided by the

optical cavity theory. More importantly, the power of thermally excited GSPs is not limited by the blackbody radiation due to near-field energy transfer. While the exfoliated graphene samples with high mobility demonstrates the potential to be infrared SP waveguides, other low-loss infrared SPs waveguides (e.g. dual-conductor transmission line metal waveguide) can also be adopted to transmit thermal signals in this scenario. This is because the near-field waves radiated by the graphene nanoemitter can also excite the propagating SPs transmission-line modes. As a result, "thermal GSP interconnects" can be realized to effectively harness thermal energy and use it to transmit information.

We developed a general formalism from the fluctuational electrodynamics and quasi-normal mode theory to elucidate the underlying physics of the far-field and near-field thermal radiation from the optical resonators made by lossy and dispersive material. Because of the modulation from the resonant mode, the thermal emission power density spectrum of the optical resonators is narrow-band and follows the Lorentz line shape with the peak at the resonant frequency of the mode. To maximize the thermal emission, our formalism demonstrated that the fractional mode losses of the emitter and the absorber (or of the far-field) require to be matched, where the fractional mode losses are explicitly defined by closed-form expressions in terms of the electromagnetic theory. In addition, we also provided a rigorous upper bound to the peak value of the thermal emission, and further suggested that the ideal the optical resonator emitters should be designed to have subwavelength size where the field of the resonant modes is quasi-static. Finally, we validated our formalism by investigating the far-field and near-field thermal emission from metal nanorods. Our formalism can therefore serve as a general rule to design the resonance-modulated thermal emission of arbitrary resonant structures.

We proposed a general principle to make the perfect thermal emitter by densely packing the transmission line resonators on a surface. Rather than using the widely used metamaterial formalism, we adopted the recently developed Quasi-Normal Mode theory, and demonstrated a general principle to maximize the thermal emission based on tuning the resistive mode loss and radiative mode loss of each transmission line resonator. Finally, we proven the concept by experimentally investigate the thermal emission of the microstrip transmission line resonator arrays, without loss of generality. Our formalism therefore broadens the horizon of the fields of thermal light sources, thermal energy management and infrared sensing and imaging.

In addition, we also implemented two numerical simulation methods (the Wiener Chaos Expansion method and the Fluctuating Surface Current method) by our home-made code with the third-party software and open-source library to directly calculate the super-Planckian thermal radiation based on the fluctuational electrodynamic formulation. We also proposed the highly efficient algorithms to expedite the direct simulations of the thermal radiation from periodic and symmetric structures with the Wiener Chaos Expansion method, and the thermal emission from the two-dimensional materials with Fluctuating Surface Current method.

7.2 Outlook and future work

Engineering the thermal radiation in the framework of fluctuational electrodynamics has demonstrated the possibilities to totally alter the emission power and the spectrum described in the classic Planck's law. In the engineering aspects, it will be interesting to investigate the thermal infrared sources with the ultra-sharp and tunable emission spectrum, which can potentially replace the infrared lasers used in the spectroscopic applications. In addition, it will

also be interesting to further explore the role of thermal radiation in the energy conversion applications, such as the optimal thermal radiative emitters in the thermophotovoltaic technologies for maximizing the heat-electricity energy conversion efficiency. The tools and the theories proposed in this dissertation provide new guidance to design more sophisticated nanophotonic thermal emitters, which can better match the required emission spectrum and meanwhile bypass the material limitations or the fabrication challenges in the previous designs.

In the theoretical aspects, the quasi-normal mode formulation proposed in this dissertation opens a new window to view the underlying principles of resonant thermal emitters. It will be interesting to further develop this theory to describe the directionality of the resonant mode modulated thermal emission, which can be important in the sensing and detection applications such as the near-field thermal scanning optical microscope.

In the simulation aspects, the computational efficiency of the Fluctuating Surface Current method can be further improved by implementing the Fast Multipole Method in the boundary element method [59]. In addition, the Quasi-Normal Mode formulation proposed in this dissertation can be further generalized as a direct simulation method for thermal radiation by considering the cross-talk terms between different resonant modes.

REFERENCES

- [1] R. Siegel, *Thermal Radiation Heat Transfer, Fourth Edition* (Taylor & Francis, 2001).
- [2] M. Planck, *Verhandlungen Der Dtsch. Phys. Gesellschaft* **2**, 202 (1900).
- [3] M. Planck, *The Theory of Heat Radiation* (Dover, 1959).
- [4] C. . Hargreaves, *Phys. Lett. A* **30**, 491 (1969).
- [5] G. A. Domoto, R. F. Boehm, and C. L. Tien, *J. Heat Transfer* **92**, 412 (1970).
- [6] A. Kittel, W. Müller-Hirsch, J. Parisi, S. A. Biehs, D. Reddig, and M. Holthaus, *Phys. Rev. Lett.* **95**, 1 (2005).
- [7] S. Shen, A. Narayanaswamy, and G. Chen, *Nano Lett.* **9**, 2909 (2009).
- [8] A. Narayanaswamy, S. Shen, and G. Chen, *Phys. Rev. B* **78**, 115303 (2008).
- [9] E. Rousseau, A. Siria, G. Jourdan, S. Volz, F. Comin, J. Chevrier, and J.-J. Greffet, *Nat. Photonics* **3**, 514 (2009).
- [10] J. Shi, P. Li, B. Liu, and S. Shen, *Appl. Phys. Lett.* **102**, 183114 (2013).
- [11] P. J. van Zwol, S. Thiele, C. Berger, W. A. de Heer, and J. Chevrier, *Phys. Rev. Lett.* **109**, 264301 (2012).
- [12] J. Shi, B. Liu, P. Li, L. Y. Ng, and S. Shen, *Nano Lett.* **15**, 1217 (2015).
- [13] R. S. Ottens, V. Quetschke, S. Wise, a. a. Alemi, R. Lundock, G. Mueller, D. H. Reitze, D. B. Tanner, and B. F. Whiting, *Phys. Rev. Lett.* **107**, 014301 (2011).
- [14] B. Song, Y. Ganjeh, S. Sadat, D. Thompson, A. Fiorino, V. Fernández-Hurtado, J. Feist, F.

- J. Garcia-Vidal, J. C. Cuevas, P. Reddy, and E. Meyhofer, *Nat. Nanotechnol.* **10**, 253 (2015).
- [15] B. Song, D. Thompson, A. Fiorino, Y. Ganjeh, P. Reddy, and E. Meyhofer, *Nat. Nanotechnol.* (2016).
- [16] S. Ingvarsson, L. J. Klein, Y. Au, A. James, and H. F. Hamann, *Opt. Express* **15**, 11249 (2007).
- [17] C. Wuttke and A. Rauschenbeutel, *Phys. Rev. Lett.* **111**, 024301 (2013).
- [18] J. A. Schuller, T. Taubner, and M. L. Brongersma, *Nat. Photonics* **3**, 658 (2009).
- [19] J. J. Brehm and W. J. Mullin, *Introduction to the Structure of Matter: A Course in Modern Physics* (Wiley, 1989).
- [20] S. Basu, Z. M. Zhang, and C. J. Fu, *Int. J. Energy Res.* **33**, 1203 (2009).
- [21] X. Liu, L. Wang, and Z. M. Zhang, *Nanoscale Microscale Thermophys. Eng.* **19**, 98 (2015).
- [22] B. Song, A. Fiorino, E. Meyhofer, and P. Reddy, *AIP Adv.* **5**, (2015).
- [23] K. Joulain, J.-P. Mulet, F. Marquier, R. Carminati, and J.-J. Greffet, *Surf. Sci. Rep.* **57**, 59 (2005).
- [24] L. Novotny and B. Hecht, *Principle of Nano-Optics*, 2nd ed. (Cambridge University Press, Cambridge, UK, 2012).
- [25] S. M. Rytov, Y. A. Kravtsov, and V. I. Tatarskii, *Principles of Statistical Radiophysics*,

Vol. 3. (Springer-Verlag, 1989).

- [26] D. Polder and M. Van Hove, *Phys. Rev. B* **4**, 3303 (1971).
- [27] C. H. Henry and R. F. Kazarinov, *Rev. Mod. Phys.* **68**, 801 (1996).
- [28] H. B. Callen and T. A. Welton, *Phys. Rev.* **83**, 34 (1951).
- [29] R. Kubo, *Reports Prog. Phys.* **29**, 255 (1966).
- [30] L. D. Landau and E. M. Lifshitz, *Statistical Physics, 3rd Ed.* (Butterworth-Heinemann, 1980).
- [31] T. Søndergaard and B. Tromborg, *Phys. Rev. A* **64**, 033812 (2001).
- [32] S.-A. Biehs, E. Rousseau, and J.-J. Greffet, *Phys. Rev. Lett.* **105**, 234301 (2010).
- [33] B. Liu and S. Shen, *Phys. Rev. B* **87**, 115403 (2013).
- [34] S.-A. Biehs, M. Tschikin, and P. Ben-Abdallah, *Phys. Rev. Lett.* **109**, 104301 (2012).
- [35] X. L. Liu, R. Z. Zhang, and Z. M. Zhang, *Int. J. Heat Mass Transf.* **73**, 389 (2014).
- [36] O. Ilic, M. Jablan, J. D. Joannopoulos, I. Celanovic, H. Buljan, and M. Soljačić, *Phys. Rev. B* **85**, 155422 (2012).
- [37] B. Liu, Y. Liu, and S. Shen, *Phys. Rev. B* **90**, 195411 (2014).
- [38] V. A. Golyk, M. Krüger, and M. Kardar, *Phys. Rev. E* **85**, 046603 (2012).
- [39] A. W. Rodriguez, M. T. H. Reid, and S. G. Johnson, *Phys. Rev. B* **88**, 054305 (2013).
- [40] J. D. Jackson, *Classical Electrodynamics* (Wiley, 1998).

- [41] S. Basu, Z. M. Zhang, and C. J. Fu, *Int. J. Energy Res.* **33**, 1203 (2009).
- [42] M. Francoeur, M. P. Mengü, and R. Vaillon, *Appl. Phys. Lett.* **93**, 126 (2008).
- [43] A. Narayanaswamy and G. Chen, *Phys. Rev. B* **77**, 75125 (2008).
- [44] C. Otey and S. Fan, *Phys. Rev. B* **84**, 245431 (2011).
- [45] R. Guérout, J. Lussange, F. Rosa, J.-P. Hugonin, D. Dalvit, J.-J. Greffet, A. Lambrecht, and S. Reynaud, *Phys. Rev. B* **85**, 180301 (2012).
- [46] X. Liu and Z. Zhang, *ACS Photonics* **2**, 1320 (2015).
- [47] J. Lussange, R. Guérout, F. S. S. Rosa, J. J. Greffet, A. Lambrecht, and S. Reynaud, *Phys. Rev. B - Condens. Matter Mater. Phys.* **86**, 1 (2012).
- [48] S.-B. Wen, *J. Heat Transfer* **132**, 072704 (2010).
- [49] A. Rodriguez, M. Reid, and S. Johnson, *Phys. Rev. B* **86**, 220302 (2012).
- [50] A. Rodriguez, O. Ilic, P. Bermel, I. Celanovic, J. Joannopoulos, M. Soljačić, and S. Johnson, *Phys. Rev. Lett.* **107**, 114302 (2011).
- [51] S. Edalatpour and M. Francoeur, *J. Quant. Spectrosc. Radiat. Transf.* **133**, 364 (2014).
- [52] A. G. Polimeridis, M. T. H. Reid, W. Jin, S. G. Johnson, J. K. White, and A. W. Rodriguez, *Phys. Rev. B - Condens. Matter Mater. Phys.* **92**, 1 (2015).
- [53] D. Xiu, *Numerical Methods for Stochastic Computations: A Spectral Method Approach* (Princeton University Press, 2010).
- [54] M. K. Chung, A. Qiu, and M. Naciewicz, in *2nd MICCAI Work. MFCA* (2008).

- [55] J.-P. Mulet, K. Joulain, R. Carminati, and J.-J. Greffet, *Appl. Phys. Lett.* **78**, 2931 (2001).
- [56] P. C. Chaumet, A. Rahmani, F. de Fornel, and J.-P. Dufour, *Phys. Rev. B* **58**, 2310 (1998).
- [57] <http://www.lumerical.com/tcad-products/fdtd/>, Lumerical Solut. Inc. (n.d.).
- [58] P. Ben-abdallah, K. Joulain, J. Drevillon, G. Domingues, P. Ben-abdallah, K. Joulain, J. Drevillon, and G. Domingues, *J. Appl. Phys.* **106**, 044306 (2009).
- [59] M. T. H. Reid and J. White, PhD Thesis (2011).
- [60] W. C. Gibson, *The Method of Moments in Electromagnetics* (CPC Press, 2007).
- [61] L. N. Medgyesi-Mitschang, J. M. Putnam, and M. B. Gedera, *J. Opt. Soc. Am. A* **11**, 1383 (1994).
- [62] C.-T. Tai, *Dyadic Green's Functions in Electromagnetic Theory* (Scranton, Intext Educational Publishers, 1971).
- [63] P. Moin, *Fundamentals of Engineering Numerical Analysis, 2nd Ed.* (Cambridge University Press, 2010).
- [64] M. T. H. Reid and S. G. Johnson, arXiv:1307.2966 (2013).
- [65] S. Z. Butler, S. M. Hollen, L. Cao, Y. Cui, J. a. Gupta, H. R. Gutierrez, T. F. Heinz, S. S. Hong, J. Huang, A. F. Ismach, E. Johnston-Halperin, M. Kuno, V. V. Plashnitsa, R. D. Robinson, R. S. Ruoff, S. Salahuddin, J. Shan, L. Shi, M. G. Spencer, M. Terrones, W. Windl, J. E. Goldberger, H. R. Gutiérrez, T. F. Heinz, S. S. Hong, J. Huang, A. F. Ismach, E. Johnston-Halperin, M. Kuno, V. V. Plashnitsa, R. D. Robinson, R. S. Ruoff, S. Salahuddin, J. Shan, L. Shi, M. G. Spencer, M. Terrones, W. Windl, and J. E. Goldberger,

- ACS Nano **7**, 2898 (2013).
- [66] F. H. L. Koppens, D. E. Chang, and F. J. García de Abajo, Nano Lett. **11**, 3370 (2011).
- [67] A. N. Grigorenko, M. Polini, and K. S. Novoselov, Nat. Photonics **6**, 749 (2012).
- [68] O. Ilic, M. Jablan, J. D. Joannopoulos, I. Celanovic, and M. Soljačić, Opt. Express **20**, A366 (2012).
- [69] L. A. Falkovsky, J. Phys. Conf. Ser. **129**, 012004 (2008).
- [70] W. Gao, J. Shu, C. Qiu, and Q. Xu, ACS Nano **6**, 7806 (2012).
- [71] V. Nayyeri, M. Soleimani, and O. M. Ramahi, **61**, 4176 (2013).
- [72] Z. Li, K. Yao, F. Xia, S. Shen, J. Tian, and Y. Liu, Sci. Rep. **5**, 12423 (2015).
- [73] J. Christensen, A. Manjavacas, S. Thongrattanasiri, F. H. L. Koppens, and F. J. G. de Abajo, ACS Nano **6**, 431 (2012).
- [74] A. Volokitin and B. Persson, Rev. Mod. Phys. **79**, 1291 (2007).
- [75] V. P. Carey, G. Chen, C. Grigoropoulos, M. Kaviany, and A. Majumdar, Nanoscale Microscale Thermophys. Eng. **12**, 1 (2008).
- [76] J.-P. Mulet, K. Joulain, R. Carminati, and J.-J. Greffet, Microscale Therm. Eng. **6**, 209 (2002).
- [77] C. J. Fu and Z. M. Zhang, Int. J. Heat Mass Transf. **49**, 1703 (2006).
- [78] A. Narayanaswamy and G. Chen, Appl. Phys. Lett. **82**, 3544 (2003).

- [79] C. R. Otey, W. T. Lau, and S. Fan, *Phys. Rev. Lett.* **104**, 154301 (2010).
- [80] S. Basu and M. Francoeur, *Appl. Phys. Lett.* **98**, 113106 (2011).
- [81] K. Joulain and J. Drevillon, *Phys. Rev. B* **81**, 165119 (2010).
- [82] Y. Liu and X. Zhang, *Chem. Soc. Rev.* **40**, 2494 (2011).
- [83] W. Cai and V. Shalaev, *Optical Metamaterials: Fundamentals and Applications* (Springer, 2010).
- [84] S.-A. Biehs, P. Ben-Abdallah, F. S. S. Rosa, K. Joulain, and J.-J. Greffet, *Opt. Express* **19**, A1088 (2011).
- [85] J. Pendry, *Opt. Photon. News* **15**, 32 (2004).
- [86] P. A. Belov, R. Marqués, S. I. Maslovski, I. S. Nefedov, M. Silveirinha, C. R. Simovski, and S. A. Tretyakov, *Phys. Rev. B* **67**, 113103 (2003).
- [87] G. Shvets, S. Trendafilov, J. Pendry, and a. Sarychev, *Phys. Rev. Lett.* **99**, 053903 (2007).
- [88] S. Basu and M. Francoeur, *Appl. Phys. Lett.* **99**, 143107 (2011).
- [89] J. Pendry, A. Holden, W. Stewart, and I. Youngs, *Phys. Rev. Lett.* **76**, 4773 (1996).
- [90] J. B. Pendry, *J. Phys. Condens. Matter* **11**, 6621 (1999).
- [91] G. S. Agarwal, D. N. Pattanayak, and E. Wolf, *Phys. Rev. B* **10**, 1447 (1974).
- [92] P. Ben-Abdallah, K. Joulain, J. Drevillon, and G. Domingues, *J. Appl. Phys.* **106**, 044306 (2009).

- [93] M. Schnell, P. Alonso-González, L. Arzubiaga, F. Casanova, L. E. Hueso, A. Chuvilin, and R. Hillenbrand, *Nat. Photonics* **5**, 283 (2011).
- [94] J. Chen, M. Badioli, P. Alonso-González, S. Thongrattanasiri, F. Huth, J. Osmond, M. Spasenović, A. Centeno, A. Pesquera, P. Godignon, A. Z. Elorza, N. Camara, F. J. García de Abajo, R. Hillenbrand, and F. H. L. Koppens, *Nature* **487**, 77 (2012).
- [95] I. Gierz, J. C. Petersen, M. Mitrano, C. Cacho, I. C. E. Turcu, E. Springate, A. Stöhr, A. Köhler, U. Starke, and A. Cavalleri, *Nat. Mater.* **12**, 1119 (2013).
- [96] Y.-M. Lin, A. Valdes-Garcia, S.-J. Han, D. B. Farmer, I. Meric, Y. Sun, Y. Wu, C. Dimitrakopoulos, A. Grill, P. Avouris, and K. a Jenkins, *Science* **332**, 1294 (2011).
- [97] M. Freitag, T. Low, W. Zhu, H. Yan, F. Xia, and P. Avouris, *Nat. Commun.* **4**, 1951 (2013).
- [98] J. Yan, M.-H. Kim, J. A. Elle, A. B. Sushkov, G. S. Jenkins, H. M. Milchberg, M. S. Fuhrer, and H. D. Drew, *Nat. Nanotechnol.* **7**, 472 (2012).
- [99] N. Nader Esfahani, R. E. Peale, C. J. Fredricksen, J. W. Cleary, J. Hendrickson, W. R. Buchwald, B. D. Dawson, and M. Ishigami, in *SPIE OPTO*, edited by L. P. Sadwick and C. M. O'Sullivan (International Society for Optics and Photonics, 2012), p. 82610E.
- [100] M. Furchi, A. Urich, A. Pospischil, G. Lilley, K. Unterrainer, H. Detz, P. Klang, A. M. Andrews, W. Schrenk, G. Strasser, and T. Mueller, *Nano Lett.* **12**, 2773 (2012).
- [101] F. Xia, T. Mueller, Y.-M. Lin, A. Valdes-Garcia, and P. Avouris, *Nat. Nanotechnol.* **4**, 839 (2009).

- [102] T. Mueller, F. Xia, and P. Avouris, *Nat. Photonics* **4**, 297 (2010).
- [103] M. Liu, X. Yin, E. Ulin-Avila, B. Geng, T. Zentgraf, L. Ju, F. Wang, and X. Zhang, *Nature* **474**, 64 (2011).
- [104] W. Gao, G. Shi, Z. Jin, J. Shu, Q. Zhang, R. Vajtai, P. M. Ajayan, J. Kono, and Q. Xu, *Nano Lett.* **13**, 3698 (2013).
- [105] S. Yiğen and A. R. Champagne, *Nano Lett.* **14**, 289 (2014).
- [106] C. Chen, S. Rosenblatt, K. I. Bolotin, W. Kalb, P. Kim, I. Kymissis, H. L. Stormer, T. F. Heinz, and J. Hone, *Nat. Nanotechnol.* **4**, 861 (2009).
- [107] I. Neumann, J. Van de Vondel, G. Bridoux, M. V Costache, F. Alzina, C. M. Sotomayor Torres, and S. O. Valenzuela, *Small* **9**, 156 (2013).
- [108] J. B. Pendry, *J. Phys. A Math. Gen.* **16**, 2161 (1983).
- [109] M. F. Craciun, S. Russo, M. Yamamoto, and S. Tarucha, *Nano Today* **6**, 42 (2011).
- [110] T. Inoue, M. De Zoysa, T. Asano, and S. Noda, *Optica* **2**, 27 (2015).
- [111] A. Lenert, D. M. Bierman, Y. Nam, W. R. Chan, I. Celanović, M. Soljačić, and E. N. Wang, *Nat. Nanotechnol.* **9**, 126 (2014).
- [112] A. P. Raman, M. A. Anoma, L. Zhu, E. Rephaeli, and S. Fan, *Nature* **515**, 540 (2014).
- [113] X. Liu, T. Tyler, T. Starr, A. F. Starr, N. M. Jokerst, and W. J. Padilla, *Phys. Rev. Lett.* **107**, 4 (2011).
- [114] M. Ghebrebrhan, P. Bermel, Y. X. Yeng, I. Celanovic, M. Soljačić, and J. D.

- Joannopoulos, Phys. Rev. A **83**, 033810 (2011).
- [115] S. Thongrattanasiri, F. H. L. Koppens, and F. J. Garcia De Abajo, Phys. Rev. Lett. **108**, 1 (2012).
- [116] L. Zhu, S. Sandhu, C. Otey, S. Fan, M. B. Sinclair, and T. S. Luk, Appl. Phys. Lett. **102**, 103104 (2013).
- [117] A. Karalis and J. D. Joannopoulos, Appl. Phys. Lett. **107**, 1 (2015).
- [118] P. T. Kristensen and S. Hughes, ACS Photonics **1**, 2 (2014).
- [119] C. Sauvan, J. P. Hugonin, I. S. Maksymov, and P. Lalanne, Phys. Rev. Lett. **110**, 237401 (2013).
- [120] E. S. C. Ching, P. T. Leung, A. M. Van Den Brink, W. M. Suen, and S. S. Tong, Rev. Mod. Phys. **70**, 1545 (1998).
- [121] E. B. Davies and E. B. Davies, *Spectral Theory and Differential Operators* (Cambridge University Press, 1996).
- [122] C. Sauvan, J. P. Hugonin, R. Carminati, and P. Lalanne, Phys. Rev. A - At. Mol. Opt. Phys. **89**, 1 (2014).
- [123] Q. Bai, M. Perrin, C. Sauvan, J.-P. Hugonin, and P. Lalanne, Opt. Express **21**, 27371 (2013).
- [124] R.-C. Ge, P. T. Kristensen, J. F. Young, and S. Hughes, New J. Phys. **16**, 113048 (2014).
- [125] L. D. Landau, J. S. Bell, M. J. Kearsley, L. P. Pitaevskii, E. M. Lifshitz, and J. B. Sykes,

Electrodynamics of Continuous Media (elsevier, 1984).

- [126] D. Schurig, J. J. Mock, B. J. Justice, S. a Cummer, J. B. Pendry, a F. Starr, and D. R. Smith, *Science* **314**, 977 (2006).
- [127] A. Sommerfeld, *Ann. Phys.* **386**, 1135 (1926).
- [128] T. A. Mandviwala, B. A. Lail, and G. D. Boreman, *Microw. Opt. Technol. Lett.* **50**, 1232 (2008).
- [129] D. Gacemi, J. Mangeney, R. Colombelli, and A. Degiron, *Sci. Rep.* **3**, 1369 (2013).
- [130] I. Fernandez-Cuesta, R. B. Nielsen, A. Boltasseva, X. Borrisé, F. Pérez-Murano, and A. Kristensen, *J. Vac. Sci. Technol. B Microelectron. Nanom. Struct.* **25**, 2649 (2007).
- [131] Y. Sun, Y. Yin, B. T. Mayers, T. Herricks, and Y. Xia, *Chem. Mater.* **14**, 4736 (2002).